

Mask Roughness Induced LER in EUV Lithography

Brittany Marie McClinton



Electrical Engineering and Computer Sciences
University of California at Berkeley

Technical Report No. UCB/EECS-2011-127

<http://www.eecs.berkeley.edu/Pubs/TechRpts/2011/EECS-2011-127.html>

December 11, 2011

Copyright © 2011, by the author(s).
All rights reserved.

Permission to make digital or hard copies of all or part of this work for personal or classroom use is granted without fee provided that copies are not made or distributed for profit or commercial advantage and that copies bear this notice and the full citation on the first page. To copy otherwise, to republish, to post on servers or to redistribute to lists, requires prior specific permission.

Mask Roughness Induced Line-Edge Roughness in Extreme Ultraviolet Lithography

by

Brittany McClinton

A dissertation submitted in partial satisfaction of the

requirements for the degree of

Doctor of Philosophy

in

Electrical Engineering

in the Graduate Division of the

University of California, Berkeley

Committee in charge:

Doctor Patrick Naulleau, Co-Chair

Professor David Attwood, Co-Chair

Professor Andrew Neureuther

And Professor Oscar Dubon

Fall 2011

The dissertation of Brittany McClinton, titled Mask Roughness Induced Line-Edge Roughness in Extreme Ultraviolet Lithography, is approved:

Co-Chair	_____	Date	_____
Co-Chair	_____	Date	_____
	_____	Date	_____
	_____	Date	_____

University of California, Berkeley

Mask Roughness Induced Line-Edge Roughness in Extreme Ultraviolet Lithography

Copyright 2011

by

Brittany McClinton

Abstract

Mask Roughness Induced LER in Extreme Ultraviolet Lithography

by

Brittany McClinton

Doctor of Philosophy in Electrical Engineering

University of California, Berkeley

Doctor Patrick Naulleau, Co-Chair

Professor David Attwood, Co-Chair

This dissertation presents a thorough investigation of how mask roughness induces speckle in the aerial image that leads to line-edge roughness (LER) effects in extreme ultraviolet lithography. As next generation lithography techniques such as extreme-ultraviolet lithography (EUVL) push to ever smaller critical dimensions, achieving the stringent requirements for line-edge and -width roughness (LER/LWR) is increasingly challenging. For this reason, discovering the principle causes leading to LER demands immediate attention.

Until recently, LER has been considered a resist-limited effect. Now, however, it is better understood that system-level effects can greatly influence LER. Thus, in order to achieve adequately low LER levels for next generation projection lithography, we must understand not only the basic material properties of the resist, but also how resist effects and mask effects can each contribute to the LER that is ultimately printed. Much research has already been conducted to fully characterize photo-resists available to next generation lithography methods. Other studies have documented how the LER on the mask couples to the printed LER. The issue of mask roughness induced LER is one that has up to this point been neglected by the industry and requires attention from the International Roadmap of Semiconductors (ITRS) in its specifications tables for the successful manufacture of transistor devices in future nodes by EUVL. Specifically, the extent to which system-level effects such as mask surface roughness, defocus, and illumination conditions are currently factoring into LER limits and how to distinguish mask effect from resist effect in practice. Potential levels for mask roughness induced LER contribution are presented for realistic mask surface roughnesses, providing a strong motivation for this work. To be precise, for the 22nm half pitch nodes, the mask roughness induced LER can consume the entire LER budget for an ideal mask roughnesses at -100nm defocus.

This thesis focuses on characterizing requirements on mask surface roughness specifications from an LER budget perspective in future nodes where EUVL will likely be employed, and devising simplified models based on 2D thin mask modeling for mask roughness induced LER prediction. A 2D height map of mask surface roughness itself is characterized by mainly two statistical parameters: the first being replicated surface roughness (RSR), which describes the height deviations of roughness on the top surface of the mask, and the second being the

correlation length, which is a measure of the lateral surface roughness. The corresponding phase map is constructed by a simple transformation of OPD into phase space with an additional factor of 2 for EUVL reflective mode. The simplified model is then constructed using thin mask modeling of that clearfield rough mask to calculate the resulting speckle statistics, which are an intensity perturbation, and uses fast 1D modeling of the image-log-slope (ILS) to map that intensity perturbation to line-edge movement (LER). This is then verified against fully simulated LER, also in the thin mask approximation. The power of this simplified model lies in the simple physicality of the formulation, elucidating the principle causes of mask roughness induced LER: poor speckle, and bad imaging quality (ILS). The formulation also provides a significant speed enhancement by removing modeling redundancy of multiple feature types on top of the same surface roughness characterizations: only one clearfield speckle simulation is needed for the speckle statistics, which can then be mapped to any feature size through the ILS, and be used by the simplified equation to predict the mask roughness induced LER.

The second simplified model is based on a geometric argument of mask slope error, for special cases of mask surface roughness that are globally smooth. In this regime, the mask roughness induced LER collapses to a single value trend across all illumination partial coherence values—hence a geometric regime. Recognizing this fact, the further simplification employs the point spread function (PSF) of the optical system assuming full incoherence, convolved with the rough mask object, to give a simple image of the mask from the wafer plane. Taking the slope of that image and propagating through focus, the mask roughness induced LER contribution can be readily predicted for this geometric limit, and provides an even further speed enhancement to modeling by reducing the redundancy of illumination partial coherence type.

Beyond developing simplified models, characterizations of problematic aberrations are made extensively for the 22nm and 16nm half-pitch nodes. This is firstly done through random distributions across the principle Zernike aberrations (Fringe Zernikes 5-16) to determine the overall acceptable level of aberrations in the system of 0.25nm rms from a mask roughness induced LER perspective. A complete aberration sensitivity matrix is then constructed to identify individual Zernikes that are problematic, specific to the node, source shape, and optical system.

In addition, mask roughness induced LER mitigation strategies utilizing an alternative source shape called ‘strip’ illumination, or, extended dipole, is explored. By using the physicality of the simplified model’s equation, we recognize that by increasing incoherence by extending a traditional dipole laterally should help mitigate the speckle, while at the same time, confined coherence orthogonal to the lines and spaces should maintain good imaging quality through the ILS. Thus, overall, the simplified model would predict a reduction in mask roughness induced LER. We compare these results to other illumination candidates specifically for the 22nm node and find that overall, the mask roughness induced LER does benefit minimally for about 0.2nm LER for 100nm defocus conditions, but there lies a significant potential benefit in throughput in comparison to traditional dipole illuminations if one is employing limiting source shapes to manufacture the partial coherence.

Lastly, this work studies potential mask roughness induced LER effects introduced by mask cleaning strategies employed for EUVL. We look at effects on lithographic performance of lines and spaces, LER, and contacts based on a repetitive cleaning process and monitor that performance through number of cleans. Overall, we find that the cleaning process does not

introduce significant deterioration of the cleaned mask in comparison to a reference mask, up through a 33× cleaning cycle. Since EUVL expects to employ cleans through 22× over the typical lifetime of a mask, the 33× good performance confirms the viability of the cleaning process within a safe margin.

to my family and KAMiKZ

Contents

List of Figures	v
List of Tables	viii
1 Introduction	1
1.1 Motivation.....	1
1.2 Problem.....	2
1.3 Major Thesis Contributions.....	3
1.4 Thesis Structure.....	3
2 Background	4
2.1 LER requirements: RLS triangle and ITRS.....	14
2.2 Sources of LER.....	15
2.3 Mask roughness induced LER.....	17
2.4 Mask roughness couples to speckle.....	17
2.4.1 Coherence enables the presence of speckle.....	17
2.4.2 Speckle caused by mask surface roughness.....	18
2.4.3 A note on the difference between surface roughness on the mask versus surface roughness on projection optics.....	21
2.4.4 A note on the importance of mask roughness and absorber roughness from an LER perspective, and capping roughness.	21
2.4.5 A note on the experimental aerial image verification of mask roughness induced LER.....	22
2.5 Current simulation methods for mask roughness induced LER.....	22
2.5.1 3D simulations.....	22
2.5.2 Thin mask modeling at EUV wavelengths and NA for practical surface roughnesses.....	23
2.6 Conclusions.....	24

3	Simplified Model	25
3.1	Mapping intensity perturbation to line-edge movement.....	25
3.1.1	Mask roughness induced speckle as an intensity perturbation.....	25
3.1.2	ILS as a mapping from change in intensity to line-edge movement.....	26
3.1.3	Simplified Model Schematic.....	26
3.2	Mismatch: Line-edge speckle vs. Clearfield Speckle.....	27
3.2.1	Modeling method.....	27
3.2.2	Initial result.....	28
3.2.3	Line-edge speckle.....	30
3.2.4	Knife-edge rough object.....	31
3.2.5	New formulation.....	33
3.3	Conclusions.....	34
4	Simplified Model Verification Part I	35
4.1	Verification on dense lines and spaces.....	35
4.2	Verification at higher NA.....	37
4.3	Verification on isolated lines and spaces.....	38
4.4	Verification at long correlation lengths.....	41
4.5	Verification with self-affine surfaces.....	42
4.6	Conclusions.....	43
5	Simplified Model Verification Part II	45
5.1	Off-Axis illuminations.....	45
5.1.2	Thresholding.....	45
5.1.3	New results through focus.....	45
5.2	Alt-PSM.....	47
5.2.1	Simulated versus Simplified at 22-nm.....	47
5.2.2	Alt-PSM vs. Lines and Spaces at 22-nm.....	48
5.3	Conclusions.....	49
6	Geometric Model	50
6.1	Geometric Regime.....	50
6.1.1	Long correlation lengths trend.....	50
6.1.2	Mask Slope Error.....	51
6.2	Geometric Model.....	51
6.2.1	Construction.....	52
6.2.2	Verification.....	53
6.3	Conclusions.....	54
7	Control and Mitigation	57
7.1	Aberrations.....	57
7.1.1	Aberrations at the 22-nm half-pitch node.....	57
7.1.2	Aberrations at the 16-nm half-pitch node.....	62

7.2	Mitigation through Extended Dipole Illumination.....	65
7.2.1	LER performance – optimal stage.....	65
7.2.2	LER performance against conventional illuminations.....	66
7.3	Conclusions.....	67
8	Application in Industry	69
8.1	Mask cleaning effects on EUV lithography process and lifetime.....	69
8.1.1	Lines and spaces, LER, and contacts.....	71
8.1.2	Mask surface roughness.....	73
8.2	LER correlation method.....	74
8.2.1	The method.....	75
8.2.2	Applied to mask cleans.....	76
8.3	Conclusions.....	77
9	Conclusions	79
	Bibliography	81

List of Figures

1	Printed line with line-edge roughness.....	2
2	LER versus LWR.....	2
3	Projection lithography system.....	4
4	Lithography wavelength scaling.....	5
5	Source, drain, and CD.....	5
6	Cost of Ownership.....	6
7	Real index of refraction through wavelength.....	7
8	Total external reflection.....	7
9	Bragg-like mirror structure.....	8
10	Multilayer mirror reflectivity curves.....	9
11	DPP source generation.....	10
12	DPP vs. LPP sources.....	11
13	Defect cause distribution.....	12
14	Phase and amplitude defects.....	13
15	RLS triangle.....	15
16	LER and gate length.....	15
17	LER and photon shot noise, through resist sensitivity.....	16
18	LTF vs MTF.....	16
19	Absorber LER versus mask surface roughness.....	17
20	Physical regimes of coherent versus incoherent illumination.....	18
21	Dephased amplitude spread functions.....	18
22	Roughness on mask leads to speckle.....	19
23	Roughness PSD.....	20
24	Potential capping layer materials.....	21
25	Correlated and uncorrelated multilayer mirror growth.....	22
26	Speckle contrast for correlated versus uncorrelated mirror layers.....	23
27	2D thin mask versus 3D modeling for speckle contrast.....	24
28	Schematic of simplified model versus conventional modeling.....	27
29	Simulated LER through focus.....	29
30	Simulated LER versus Simplified model LER, initial trial.....	29

31	Clearfield versus line-edge speckle schematic.....	30
32	Clearfield versus line-edge speckle calculation.....	30
33	Simulated versus Simplified model LER with line-edge speckle LER, 50pm.	30
34	Simulated versus Simplified model LER with line-edge speckle LER, 230pm.	30
35	Knife-edge object.....	32
36	Knife-edge numerical results.....	32
37	Simulated LER versus Simplified LER.....	33
38	Simulated LER for 50nm L/S.....	36
39	Simulated LER versus Simplified LER, disk illuminations.....	37
40	Simulated LER versus Simplified LER, high-NA.....	38
41	Isolated line versus isolated space schematic.....	39
42	Maximum intensity comparison, isolated line versus space.....	39
43	Simulated LER versus Simplified LER, isolated line and space.....	40
44	Simulated LER, 50nm and 22nm isolated features.....	41
45	Simulated LER for long correlation lengths.....	42
46	Simulated LER versus Simplified LER, roughness exponent.....	43
47	Simulated LER versus Simplified LER, 22nm L/S, off-axis source shapes....	46
48	Simulated LER versus Simplified LER, 16nm L/S, off-axis source shapes....	47
49	Simulated LER versus Simplified LER, alt-psm.....	48
50	Simulated LER, 22nm alt-psm versus lines and spaces.....	49
51	Mask slope error schematic.....	51
52	Image placement error schematic.....	51
53	Geometric model schematic.....	52
54	Simulated LER versus Simplified LER, with geometric model.....	53
55	Simulated LER versus Simplified LER, with geometric model.....	54
56	Simulated LER versus Simplified LER, with geometric model.....	54
57	ILS comparison, 50nm versus 22nm at NA=0.5.....	55
58	22nm L/S Simulated LER: 10 random rough masks against 1 random Zernike.	58
59	10 random Zernike distributions.....	58
60	22nm L/S Simulated LER: 10 random rough masks against 1 random Zernike.	59
61	22nm L/S Simulated LER: 1 random rough mask against 10 random Zernikes.	59
62	22nm L/S Simulated LER: average of 10 random Zernikes.....	60
63	22nm L/S Simulated LER: individual zernikes against 1 random rough mask..	61
64	16nm L/S Simulated LER: 10 random rough masks against 1 random Zernike.	62
65	16nm L/S Simulated LER: 10 random rough masks against 1 random Zernike.	63
66	16nm L/S Simulated LER: 1 random rough mask against 10 random Zernikes.	63
67	16nm L/S Simulated LER: average of 10 random Zernikes.....	63
68	16nm L/S Simulated LER: individual zernikes against 1 random rough mask..	64
69	Five stages of extended dipole schematic.....	66
70	Simulated LER of five stages of extended dipole.....	66
71	Simulated LER of 3 rd stage extended dipole versus crosspole.....	67
72	ILS and Contrast of 3 rd stage extended dipole versus crosspole and dipole.....	67
73	Exposure latitude comparison of reference mask versus test mask.....	71
74	LER trends for both reference and test mask.....	72
75	RuML raw and MSFR surface roughness.....	73
76	AFM images of Ru surface of test mask.....	74

77	EUV reflectivity of witness plate through cleans cycles.....	74
78	SEM image of alignment feature and lines.....	76
79	Correlation between each adjacent exposure, test and reference mask.....	77

List of Tables

1	Process comparison for 36 and 40nm L/S.....	71
2	Iso-focal matched and average CD comparison for 36 and 40nm L/S.....	72
3	Critical dimensions and STD values for 45 and 50nm contacts.....	73

Acknowledgements

There are many people to thank who made this thesis possible, and who contributed to making my time in Berkeley great. My adviser, Patrick, especially made this work possible. His knowledge of coherence and EUV lithography continually astonishes me. It was an honor to learn from him, and be able to use that knowledge to make a contribution to science. My academic adviser, Dave, provided great guidance through my graduate years. He encouraged me to explore all aspects of CXRO, informed me of a great research opportunity abroad, and gave thoughtful advice about career. Andy Neureuther was not only a great teacher in my favorite subject- E&M- but also very ready to help with all the ins and outs of the EECS department, and how I could furnish my graduate courses around my interests. These were my advisers- and to each one of them I am very grateful.

At CXRO, I had a stellar team to work with and have support from. They included Ken Goldberg, Eric Gullikson, Erik Anderson, Weilun Chao, Iacopo Mochi- all of whom provided a great resource to ask questions and bounce ideas off, all of whom are very dedicated to their work. Simi George and Regina Soufli gave not only expertise, but company that has been invaluable.

Rok Yu of Panoramic gave excellent, consistent support on software, and always responded quickly and thoroughly. This was especially helpful in crunch times before conferences.

While I had an excellent academic environment at Berkeley, my friends outside that arena provided a different, but also very rich experience that complemented my entire time there. Lynn Wang not only provided a distant link to EECS, but also great conversation, whether simply at lunch, the opera, or a walk at the wharf. Nina Merolle, my german teacher, was first, a great teacher, and then later a great friend.

Personally, I would like to thank my former roommate Nancy, for her unconditional support. My friends Meral, Rachel, and Erin, though each one of you very physically far from Berkeley, were close here in my mind. My family, too, were always very encouraging and supportive. Especially my brother, for teaching me not to be bullied by bullies, even though they can give me carpet burns.

Lastly, of course, Nik. There is really too much to say here, but above all, proving to me that everything that can run on that operating system, can run on this operating system, better.

Chapter 1

Introduction

1.1 Motivation

The goal of this thesis is to explore a new significant contributor to line-edge roughness (LER) in extreme ultraviolet lithography (EUVL), called mask roughness induced LER.

As next generation lithography techniques such as extreme-ultraviolet lithography (EUVL) push to ever smaller critical dimensions, achieving the stringent requirements for line-edge and -width roughness (LER/LWR) is increasingly challenging. For this reason, discovering the principle causes leading to LER demands immediate attention.

Until recently, LER has been considered a resist-limited effect. Now, however, it is better understood that system-level effects can greatly influence LER. Thus, in order to achieve adequately low LER levels for next generation projection lithography, we must understand not only the basic material properties of the resist, but also how resist effects and mask effects can each propagate down to and contribute to the LER that is ultimately printed. Much research has already been conducted to fully characterize photo-resists available to next generation lithography methods. Other studies have documented how the LER on the mask (absorber LER) couples to the printed LER. What remains incompletely understood, however, is the extent to which system-level effects such as mask surface roughness, defocus, and illumination conditions are currently factoring into LER limits and how to distinguish mask effect from resist effect in practice.

This work focuses on characterizing requirements on mask surface roughness specifications from an LER budget perspective in future nodes where EUVL will likely be employed, and devising simplified models for mask roughness induced LER prediction. The issue of mask roughness induced LER is one that has up to this point been neglected by the industry and remains ignored by the International Roadmap of Semiconductors (ITRS) [1] in its specifications tables for the successful manufacture of transistor devices in future nodes by EUVL. We attempt to remedy that, and provide tools to greatly ease the calculation and prediction of mask roughness induced LER, and verify them against 2D thin mask modeling, assuming a simple binary threshold model for the resist.

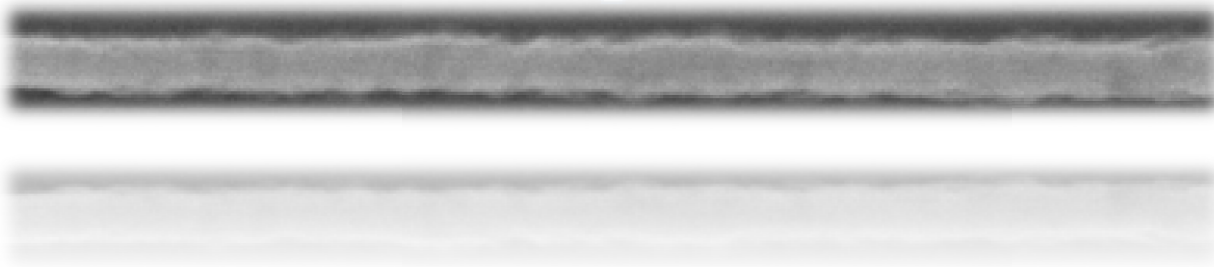


Fig. 1. An image of a printed line in photo-resist exhibiting line-edge roughness (LER).

1.2 Problem

Because EUVL is a band-limiting imaging process (i.e., an aperture limits the spatial frequencies it passes), the mask surface roughness (which is geometrically related to phase roughness, also known as replicated surface roughness- RSR, defined as the roughness on the top surface of the mask as replicated through the multilayer) is directly coupled to speckle-induced intensity variations at the image plane, and can significantly alter LER measurements of the printed image. Moreover, because EUVL is dependent on reflective optics and masks, the geometrical relation of mask roughness to phase roughness is amplified by a factor of 2 due to reflection. As defocus is introduced, mask phase errors even further couple into intensity variation, or speckle. As expected, when coherence is increased, speckle is enhanced, and the mask phase error-induced speckle increases proportionately.

As current semiconductor manufacturing roadmaps do not take into account mask roughness as a potential LER contributor, and it has been shown [2-5] that out of focus mask roughness induced LER can be on the order of several nanometers, the mask roughness issue cannot be ignored. There must be a fast, efficient means of predicting its contribution to provide industry with a realistic prediction of the total LER figures to balance terms in the LER budget.

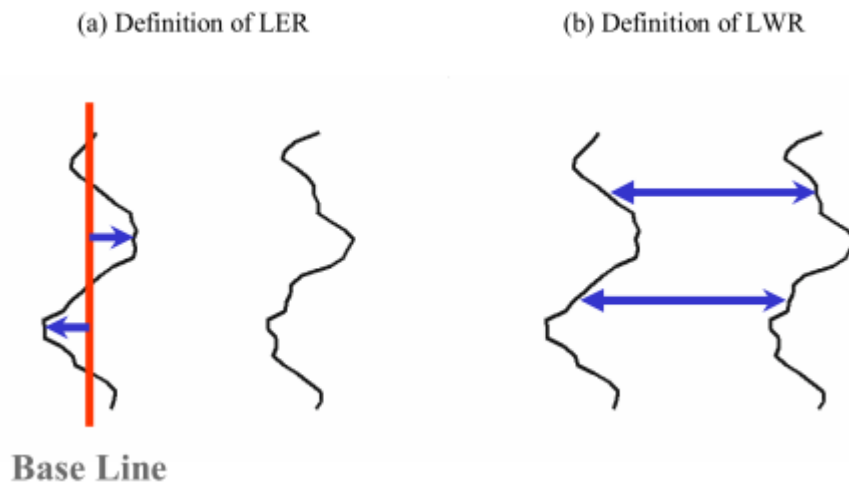


Fig. 2. Basic characterizations of line edge roughness (LER) as opposed to line width roughness (LWR) [61].

1.3 Major Thesis Contributions

The original work in this thesis lies in Chapters 3-8. The greatest contribution is made in Chapters 3 and 4, whereby a physical mechanism is developed for mapping mask roughness induced speckle to LER through the process of thresholding the aerial image. The greatest contribution of the work is found in verification of this model for a variety of features and conditions. Extensive peripheral work makes up the remainder of the thesis, such as further simplifications to the modeling process for geometric regimes, exploring mask roughness induced LER under optical aberrations, mitigation strategies, and applications of the mask roughness induced LER concept to mask cleans studies.

1.4 Thesis Structure

Chapter 2 provides a review of the status of the major challenges to EUVL, and sets the stage for the context of mask roughness induced LER in that bigger picture. The main contribution of this thesis is to construct a simple physical model by which speckle in the aerial image can be linked to the LER, which starts in Chapter 3. This is done by recognizing that speckle is fundamentally an intensity perturbation that can be mapped to line-edge movement by virtue of the thresholding process specific to the image-log-slope for the feature pitch, imaging system, and illumination conditions under investigation. As seen in Chapter 3, further contributions use this concept to facilitate existing, intense simulations for mask roughness induced LER by developing a simplified model to speed up the modeling process in the thin mask regime. The speed factor that the simplified model allows the mask roughness induced LER prediction to be enhanced by is dependent on the number of different feature pitches one wishes to investigate. The simplified model, therefore, can be a powerful tool when applied across an entire mask pattern comprising simultaneously many feature types. The model is verified in Chapters 4 and 5 against both on-axis and off-axis illumination conditions, dense and isolated features, through focus, down to the 16nm half-pitch.

An even further simplification to the modeling process is found in Chapter 6 for an “incoherent” or “geometric” illumination regime for long correlation lengths of spatial roughness on the mask, whereby simulation speed is increased by a factor proportional to however many illumination conditions one wishes to investigate.

The information gathered from both fully simulated and simplified model simulated LER is used to compose guidelines on the mask surface roughness specifications for future nodes that EUVL will in all likelihood be applied to. We also make investigations into the nature of mask roughness induced LER under the presence of optical aberrations in Chapter 7, and apply what is learned from the construction of the simplified model to conceive of potential LER mitigation strategies by manipulating illumination conditions.

Chapter 8 explores experimental effects of mask roughness in the context of a mask cleaning study. Results look at effects of the LER the mask cleaning process imposes, and a related concept- contact size variation. We also apply the recently developed LER correlation method [6] to the mask cleans study as an independent means of calculating the mask contributions to total printed LER in resist, thereby monitoring any effects the cleaning process has on changing the mask properties.

Chapter 2

Background

Projection lithography has allowed continuation of Moore's Law to extend several decades beyond the original contact lithography techniques, and their high throughput optical systems keep cost of ownership (CoO) down. As critical dimensions of circuits approach the 2 \times -nm feature size threshold, however, optical lithography [7-10] cannot operate in single-exposure conditions. As with any photon-based system (see Figure 3), the resolution of projection lithography is fundamentally diffraction limited. Meaning, the smallest resolvable feature that can be produced depends on the converging angle and the illumination wavelength ($\text{Res} \sim k_1 \lambda / \text{NA}$, where k_1 is a process dependent factor), as shown in Figures 4 and 5.

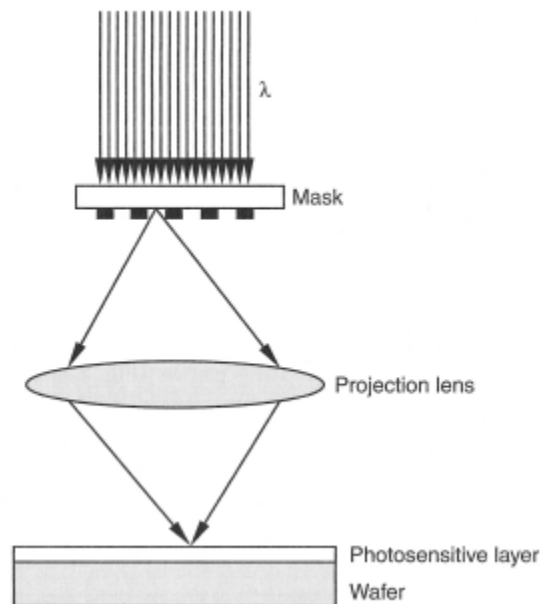


Fig. 3. A typical projection lithography system, transmissive mode with Kohler illumination [10].

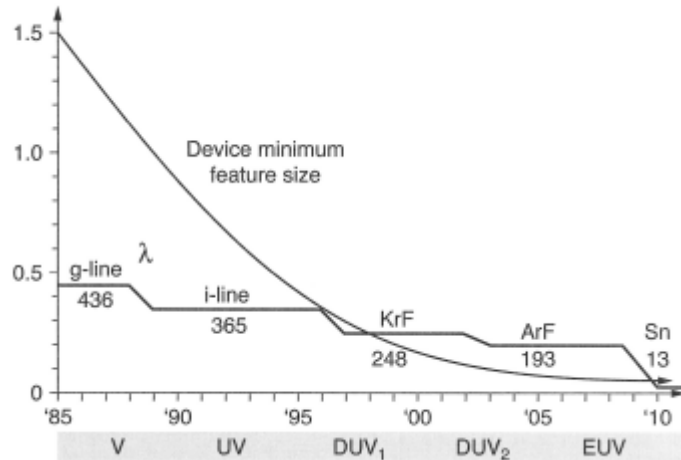


Fig. 4. Lithography wavelength scaling [10].

Immersion techniques with traditional ArF excimer lasers at 193nm have extended the life of optical lithography by allowing the illumination angles to be larger through so-called hyper-NA optics, or optics with NA effectively greater than 1. Beginning with the 45-nm half-pitch node, 193nm immersion techniques alone could not provide the resolution capabilities necessary. Techniques such as double patterning and spacer technology have been employed to meet the resolution requirements- but at extreme cost. Both techniques require the use of multiple masks per layer. If an alternative should appear that would allow the return to a single exposure per level printing, it would have obvious cost advantages. It was clear in the late 1990s that ultimately, optical lithography would reach a limit and that next generation lithography (NGL) techniques should be explored (see Figure 6).

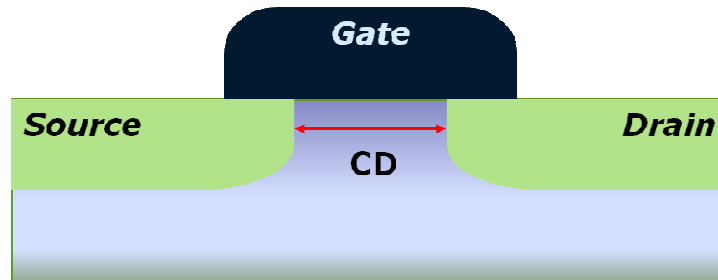


Fig. 5. Picture of source and drain connected by gate: the width of the pitch, called critical dimension (CD), determines the minimal gate length. The minimal CD achievable is set by the resolution of the system.

NGLs that would potentially provide such single exposure capabilities, such as direct electron beam writing, x-ray lithography, Scattering with Angular Limitation Projection Electron Lithography (SCALPEL), and ion beam lithography, all faced substantial implementation barriers that drove cost of ownership to become prohibitive to high volume manufacturing (HVM). One by one they were eliminated as viable alternatives. Direct electron beam writing had drawbacks relating to extremely low throughput (<10 wafers per hour), despite attractions such as design file size (no optical proximity corrections (OPC) are needed at 1 \times). X-ray lithography mask making required the use of a special substrate-thin membranes of silicon

carbide- rather than the traditional fused silica. This came with all the complications of stress-related issues of thin films such as feature position errors as a complicated function of feature density and locations of absorber material. The x-ray lithography system was also designed for 1× demagnification, so any defects would be printed directly without mitigation. While SCALPEL offered a 4× imaging advantage, it faced severe stitching problems, the need for silicon instead of glass for the mask, and lack of a pellicle, among other reasons. Lastly, ion beam lithography would provide high resolution with an ion beam on a 4× system, but had a huge disadvantage in that it applied a stenciling technique to its mask manufacturing: no isolated dark feature can ever be printed in a single exposure. In addition, it too required a silicon wafer as the mask substrate instead of fused silica, and had no pellicle.

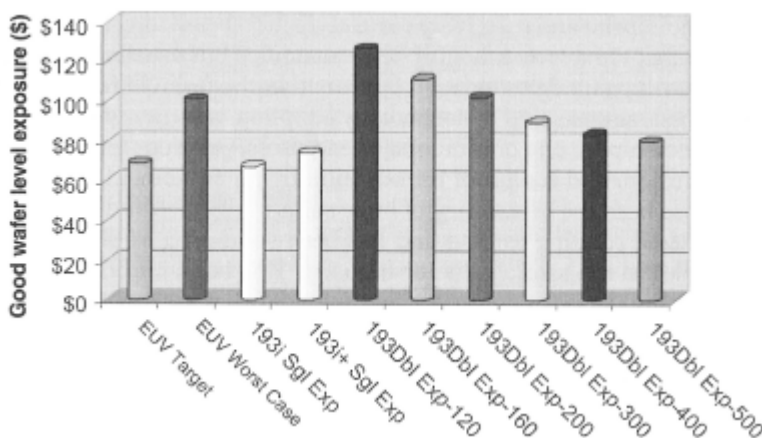


Fig. 6. Typical cost of ownership for likely litho-solution candidates [10].

The currently favored- and likely- NGL candidate, extreme ultraviolet lithography (EUVL), offers the best combination of advantages thus far. It drastically enhances resolution by roughly a factor of 5 (assuming a comparable k_1 -factor) through a near 14-fold reduction from 193nm to a nominal wavelength of 13.5nm, despite a lower overall NA of 0.33 on the current NXE:3300B platform offered by ASML [11]. EUVL is also an attractive option for its relative similarity to optical lithography; it can rely, at least partially, on the vast expertise of photon-based optical lithography techniques developed over the past four decades, and uses the traditional glass substrate and form factor for the mask.

Ultimately, however, EUVL has been held back by the fundamental differences in materials properties and behaviors that exist between optical wavelengths and 13.5nm. Originally planned for introduction at the 32nm half-pitch node, delays have caused it to miss the deadline, as well as for the 28nm node. It is planned that EUVL will be employed for critical layers in combination with double patterning when it is introduced.

EUV Materials Properties

At the extreme ultraviolet wavelength regime, most materials have an index of refraction just under one, due to high material absorption for 13.5nm, where the index of refraction, n , for a material is given by

$$n = 1 - \delta + i\beta,$$

and δ is the material phase speed and β is the material absorption coefficient. This high amount of absorption for EUV means firstly, that refractive optics are not an option, and secondly, as a consequence, that innovative ways of constructing mirrors are necessary to maintain high reflectivity and throughput for the fast printing of wafers, and the elimination of any protective pellicle.

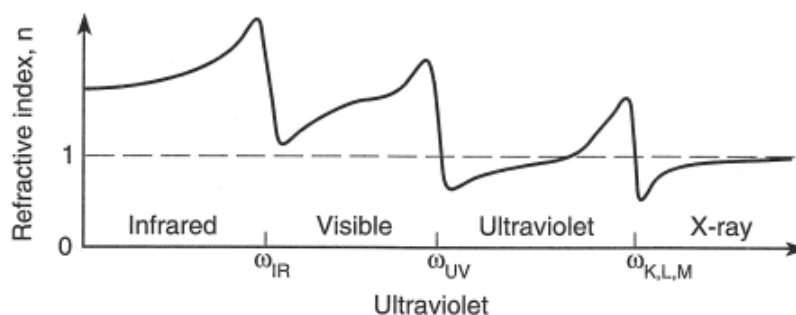


Fig. 7. Real index of refraction component varying through wavelength [14].

Because $n \sim 1$, the reflection coefficient between two surfaces is small for most angles of incidence due to little change of field amplitudes across the interface. An exception occurs for incident radiation at glancing incidence angles to the material surface, far from the surface normal. Similar to total *internal* reflection for optical light, for extreme ultraviolet the phenomenon is known as total *external* reflection [12-14]. This can largely be understood through the concept of Snell's law, which for a vacuum/material interface at EUV would reduce to

$$\sin \phi' = \sin \phi / 1 - \delta,$$

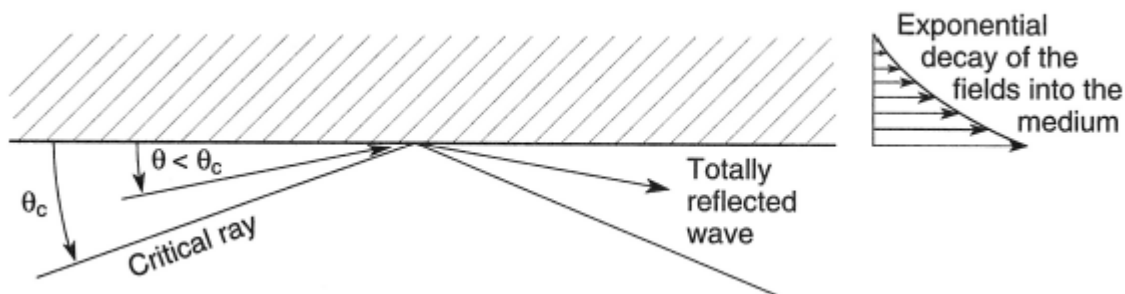


Fig. 8. Total external reflection for extreme ultraviolet and soft x-rays [14].

assuming $\beta \sim 0$. Because the $1 - \delta$ factor is somewhat less than one, the refracted wave is at an angle φ' that is a little further from the surface normal than φ . Under the limit that $\varphi' = \pi / 2$ so that $\sin \varphi' = 1$, we have the *critical angle* φ_c condition where

$$\sin \varphi_c = 1 - \delta,$$

and converting to glancing angles where $\theta_c = 90 - \varphi_c$, for a small angles approximation we have

$$\theta_c = \sqrt{2 \delta}.$$

Therefore, at incident angles less than or equal to θ_c , we can achieve near total external reflection whereby the wave is totally reflected outside of the material. So called *glancing incidence mirrors* are common in EUV use as they can maintain near-perfect reflectivity. They are employed whenever possible in EUVL tools to provide maximal source power.

The problem occurs as soon as the optical train in a potential lithography system needs to manipulate the illumination wavefront, and image the mask to the wafer. Structural properties of the beam such as spatial coherence and illumination uniformity, and imaging 3D absorber structures on a mask, all require the use of a reflective optic that can operate much closer to the surface normal. (Refractive optics are, again, precluded due to the extremely absorptive nature of materials for EUV, that would severely diminish power and throughput in litho tools). Therefore, in order to achieve high reflectivity at these near-normal incidence angles, multilayer interference coatings are used for mask architectures [15-20].

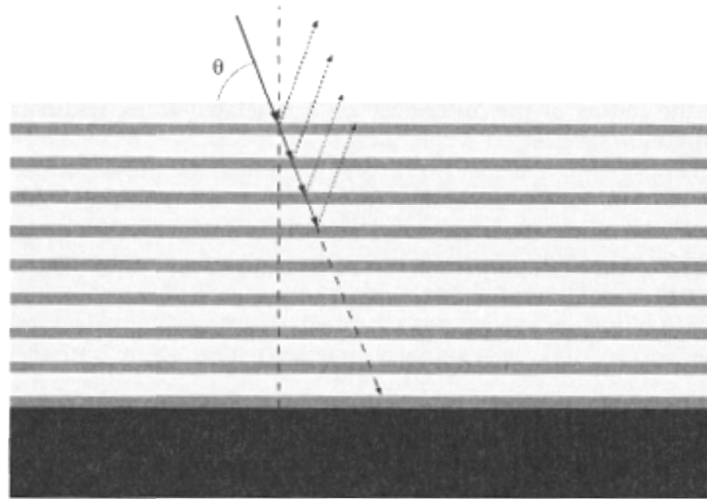


Fig. 9. An example of constructive scattering through multiple layers of a Bragg-like mirror structure [14].

In a medium of uniform refractive index, no scattering occurs. Only when there are variations in the refractive index does scattering arise, such as between two materials with large differences in atomic number, Z . By alternating coatings of high and low Z materials with a periodicity (for one layer pair) of $d \sim \lambda / 2$ for near-normal incidence illumination at wavelength λ , high reflectivity of $\sim 70\%$ can be achieved [21-23]. (The illumination cannot be perfectly at normal

incidence due to the need for actually imaging an absorber structure on top of the mirror down to the wafer.)

These multilayer Bragg-like mirror structures can alternatively be viewed as sinusoidal density gratings creating a resonant structure through angle and wavelength. For a true sinusoidal grating, the Fourier transform would yield only a single Bragg peak ($m=1$) [24]. For sharp interfaces where the grating represents a step function, Bragg peaks will appear for odd orders ($m=1,3,5,\dots$). Asymmetry due to diffusion between the interfaces can cause even orders to appear, as well as diminish overall reflectivity. This is usually not desired, so diffusion is prevented by depositing B_4C between layers [25-26].

For EUV at 13.5nm, or equivalently 92eV, most materials have the aforementioned extremely high absorption (typically high Z), so it is much more important to choose the so-called *spacer* material (typically low Z), whose role is to provide good scattering contrast while minimizing absorption. Good candidates for the spacer material include C, B, Be, Si, and Al, all of which have K- and L- absorption edges in the EUV region, allowing for minimal absorption just above the absorption edge [10]. Early prototypes of multilayer mirrors were with Mo/Be that were capable of achieving 69.3% peak reflectivity with 0.35nm bandwidth, but were eventually replaced with Mo/Si designs that provided a lower peak reflectivity of 67.2% [27]. While this represents a loss of 17% gain in resist activation, the Mo/Si architecture avoided a toxic material (Be), and also provided greater bandwidth of 0.55nm [10]. Multilayer mirror concepts can even be employed at near-glancing incidence to provide a Bragg peak at an angle several times larger than the critical angle, which has advantages in larger angular bandwidth, increased NA, and reduced aberrations (as it is closer to the surface normal) [14].

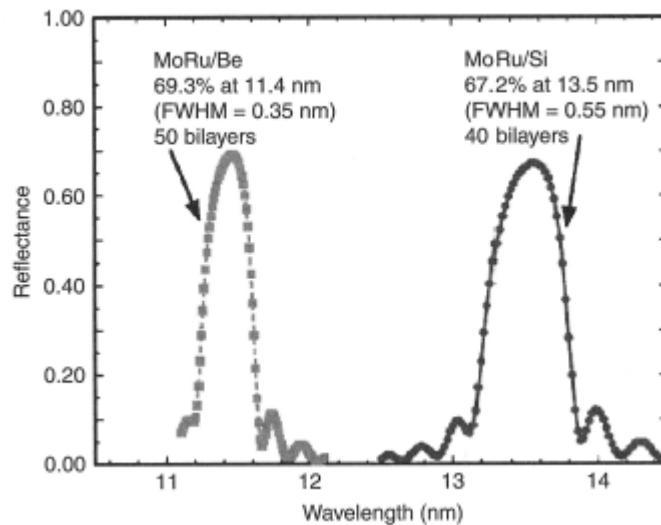


Fig. 10. Sample reflectivity curves for two multilayer mirror architectures [10].

Despite the innovations in the forms of glancing incidence and multilayer mirrors, the materials differences at 13.5nm nonetheless remain a challenge for EUVL in three main areas: source, mask defects, and photo-resist.

EUVL Sources

Ever since EUVL was first explored in the late 1980s, problems with providing a high-powered portable source have plagued the industry. The only plentiful source of photons in this wavelength regime was through exposure systems mounted at end-stations of synchrotron facilities, such as the micro-field exposure tool (MET) [28-39]. A synchrotron facility, however, is certainly not a feasible option for the semiconductor industry. Recently, progress has been made in this arena, and two potential source designs currently dominate the source market [40]. These designs are based on either electrical-discharge- or laser-produced plasmas (DPP and LPP, respectively) that emit at EUV wavelengths. Neither of these sources have either the same level of spectral purity or power of the currently employed line-narrowed excimer lasers.

The discharge-produced plasma source method supplied by Philips Extreme UV GmbH [41] employs two rotating electrode wheels covered with a thin layer of fuel [42-43]. The original fuel choice was Xe, but the industry has over the years moved to the use of Sn for improved conversion efficiency [10]. By laser ablation a tiny tin plume extends from one of the electrodes eventually reaching the other electrode, both of which are connected by a capacitor bank. When the plume completes the circuit between the electrodes, a discharge of several joules of energy produces a current of ~ 20 kA, and creates a highly ionized tin plasma that emits at EUV wavelengths at a few kilohertz repetition rate. The method, however, has problems dealing with large power dissipation. The issue is reaching powers above 100W, and a large amount of debris is also generated. This is the source used in the Alpha Demo Tool (ADT) [44-50].

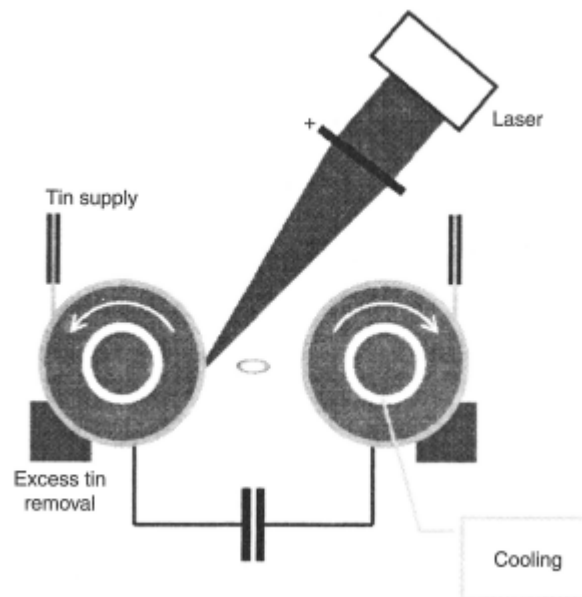


Fig. 11. Detail of DPP source generation [42].

The other source candidate that is the choice for the NXE:3300B is the laser-produced plasma that also works by employing Sn as a fuel, this time in the form of droplets through a nozzle. Because of the high material absorption properties, the optical train must operate in vacuum, which precludes convectional heating that would normally be present [10]. As a consequence, radiative cooling freezes the fast moving liquid by the time it reaches a focused laser beam that

would ideally generate a plasma that emits at EUV. Each droplet is hit by a separate, sequential laser pulse. Once again, contamination of the vacuum chamber and optics is an issue, and the nozzle dispenser has difficulties of flow and accumulation effects.

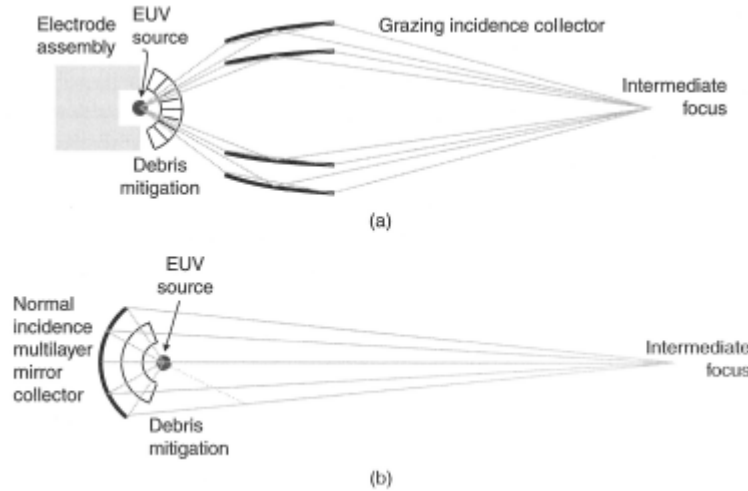


Fig. 12. (a) DPP source and (b) LPP source schematics [10].

Debris is perhaps the largest disadvantage of both DPP and LPP source types, through the limitations this places on the collector optics which must maintain lifetimes of 30,000 hrs (about 3 yrs.) with less than 1% drop in reflectivity per mirror. Coupled with the fact that EUV has high material absorption and power is already very low, debris needs to be kept to the minimum possible. This has led to the SoCoMo designs, or *Source Collector Modules*, that are distinct in nature for both DPP and LPP source types. The rule that guides the design above all is source-to-collector coupling efficiency (typically around 33%). For DPP, the SoCoMo unit consists of nested grazing incidence, ellipsoidal or Wolter type I hyperboloidal-ellipsoidal reflectors [49] that are fabricated in thin shells mounted on a spider wheel. Since the particles do not flow ballistically, but are influenced by fields, many end up sticking to walls of an employed foil trap (similar to venetian blinds) in the design, to keep them from the mirror surfaces.

LPP SoCoMo is fundamentally different by nature due to being able to reach the other 2π solid angle of EUV source emission that was before being blocked by the electrode assembly for the DPP setup. The full spherical source space can now be accessed, and normal incidence multilayer mirrors can be situated in the back hemisphere. Use of a repeller-field concept that drives particles away from mirror surfaces can reduce the debris by a factor of 40 [51-52]. For LPP, optimization of droplet size can also have a major role in reducing debris. Smaller droplets produce less debris, but longer wavelength lasers usually have bigger focus spots which would cause a mismatch between droplet size and focal spot size, causing wasted power. For a lens of diameter D_l (cm) and focal length f_l (cm), the focal spot size d_0 (cm) is by diffraction a minimum for a laser with wavelength λ

$$d_{0(min)} = 1.22 f_l \lambda / D_l.$$

It is therefore highly desirable to use a lens with a large focal length to keep debris from mirrors, and a small diameter to reduce solid angle and thermal distortion, so spot sizes and therefore

debris of the tin tend to be larger for long wavelength lasers [10]. One way to mitigate this is by hitting the droplets with a laser pre-pulse to get the droplet to expand and better match the spot size.

In the end, after the SoCoMo unit with the collector optics, all the light is brought to an intermediate focus that is then transferred to the rest of the lithography tool in a separate vacuum environment to prevent debris from reaching downstream mirrors. No matter the employment of either glancing incidence or normal incidence optics, the fact remains that a large portion of the EUV light will be absorbed at every mirror interface, and will limit source power. For HVM, it is required that source power at intermediate focus deliver several hundred watts of spectrally pure light (100W is equivalent to about 60 wafers per hour). As of this writing, both LPP and DPP sources are at the 10W level (about 5-6 wafers per hour), and have shown little progress over the past three years [53]. This remains a grave concern for EUVL.

EUVL Mask Defects

Due to the reflective architecture and extensive use of multilayer mirror optics, as well as the use of no pellicle, many opportunities to introduce defects occur. Most defects are introduced on the substrate as pits, but a significant number as well through the multilayer deposition process. Small, but significant ones can occur through handling and substrate particles. In whatever way defects are introduced, their total number must be zero [54].

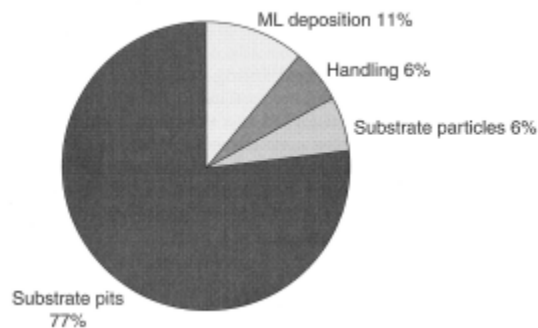


Fig. 13. Defect cause distribution [10].

Defects are of two types: amplitude and phase. Amplitude defects are those that lie on the top surface of the multilayer mirror and cause changes in field amplitude through absorption. Phase defects are those embedded through the vertical height of the multilayer stack by locally changing the phase of the field. Ultimately, this causes a small shift in peak reflectivity wavelength of the multilayer [10]. The preferred solution exists for both types of defects in the form of optimal placement and OPC for the absorber pattern that can potentially cover the defect [55]. Above all, to avoid missing defects, the mask should be imaged at actinic wavelengths during inspection [56]. Defect counts are currently non-zero, and therefore do not meet HVM requirements and are the second critical area pertaining to EUVL.

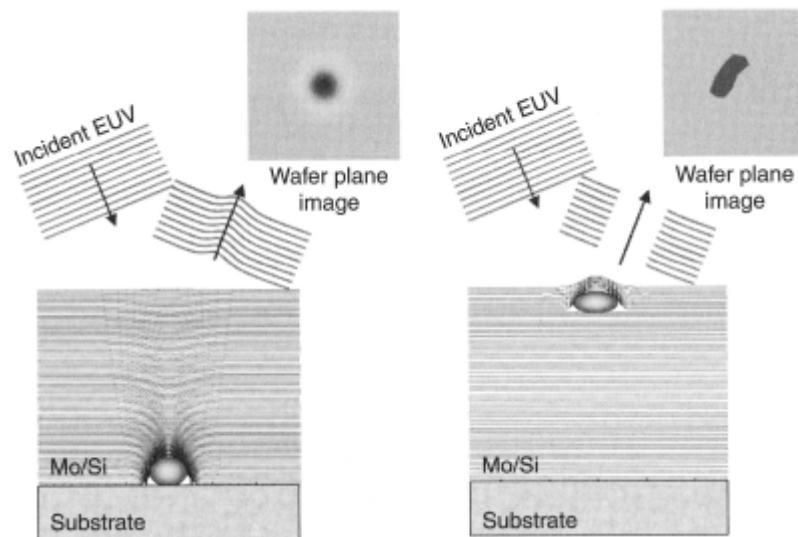


Fig. 14. (Left) Phase defects found at the bottom of the multilayer, and (right) amplitude defects found at the top surface of the multilayer [10].

EUVL Resist

The third greatest concern for EUVL commercialization lies in the readiness of a suitable resist platform. Once again, the goal is keeping down CoO, and the resist can aid in this by helping achieve high transistor density with high throughput by fast recording of that photonic image (called sensitivity) to produce as many wafers as possible. With the wavelength change to EUV, resist chemistry must satisfy performance categories through its material properties at 13.5nm.

Resist as a photo-detector works by creating solubility differentials across regions where photons are absorbed, and those where they are not. The resist itself is made of a resin polymer that carries sensitizers, called photo-acid generators (PAG), which are the light-sensitive components.

For such so-called chemically amplified (CA) resists, the exposure energy does not directly cause the solubility differential, but rather generates a chemically stable catalytic species, aka “photoacid”, designated as a proton, H^+ . The resin of CA resists contain a base polymer with that contain acidic hydroxyl (-OH) groups to give it high solubility under normal circumstances. The polymer, however, is prepped for exposure by partially blocking these sites with other chain molecules to reduce solubility. During a post-exposure bake (PEB), the increased temperature (activation energy) initiates a chemical reaction to use the generated photoacids and remove the blocking group and therefore make the polymer soluble (this process is known as “deprotection”), as well as regenerate catalytic acids to prolong the solubility-switching chemical reaction. This cascade of solubility switching reactions in the exposed regions can typically have a chain length in the many 100’s. For the reason of very efficient solubility differential generation, when the sensitivity of the resist can be enhanced, exposure times can be shorter, more wafers per hour can be exposed, CoO decreases, and CA-resists are the preferred platform [8].

As half-pitches become extremely small, however, CA-resists become diffusion limited. High activation energy (high PEB temperature) CA-resists with t-butyl ester and butoxycarbonyl blocking groups mean that the photoacids have large diffusion lengths during the PEB. This creates high image blur that reduces image quality (but can aid in smoothing out line-edge roughness (LER)). The diffusion length for high activation energy CA resists is larger, while low activation energy (low PEB temperature) CA resists have less image blur. Not only is the LER less mitigated by blur, but the blocking groups of a low activation energy CA resist are the acetal and ketal groups and solvent which result in much outgassing that harm the imaging optics and severely reduce lifetime [57]. This can be mitigated, but not eliminated, by introducing a post-apply bake (PAB) after first applying the wafer with resist before exposure. The PAB serves to reduce the amount of remaining solvent in the resist that was initially needed for applying a uniform, smooth coating across the wafer. But the highly energetic EUV photons enhance the volatility of the molecules, and the vacuum environment required for EUVL also facilitate freely moving vapors [10]. Current resist research is therefore focusing on resists that can firstly achieve the high resolution necessary without outgassing, but obviously at the cost of sensitivity and throughput. Inpria has recently shown quality imaging results in an inorganic Hafnium based resist, but at high sensitivity [58].

2.1 LER requirements for EUVL: the RLS triangle

As mentioned above, in order to achieve HVM requirements, the resist for EUV must meet certain performance categories. There are three main capabilities that are the cornerstone of resist performance, that are in fact to some degree mutually exclusive. They are: resolution, LER, and sensitivity, which form what is referred to as the RLS triangle for a particular resist formulation. EUVL introduction at the 22nm half-pitch requires a resolution of 22nm. According to the International Roadmap for Semiconductors (ITRS)[1], LER should be limited to about 1.7nm. And sensitivity, as mentioned should be 10 mJ/cm². Simultaneously meeting all three requirements is a great challenge. Small features (high resolution) can be printed very quickly (high sensitivity), but with poor LER. If LER is instead addressed and high sensitivity is maintained, the resolution suffers. (This exchange between resolution and LER occurs through the image blur, as required for high sensitivity resists that are CA based, with a necessary PEB bake.) Therefore, novel resist formulations are necessary. Resolution is the absolute requirement for the resist, so it is paramount to limit any excess LER contributions.

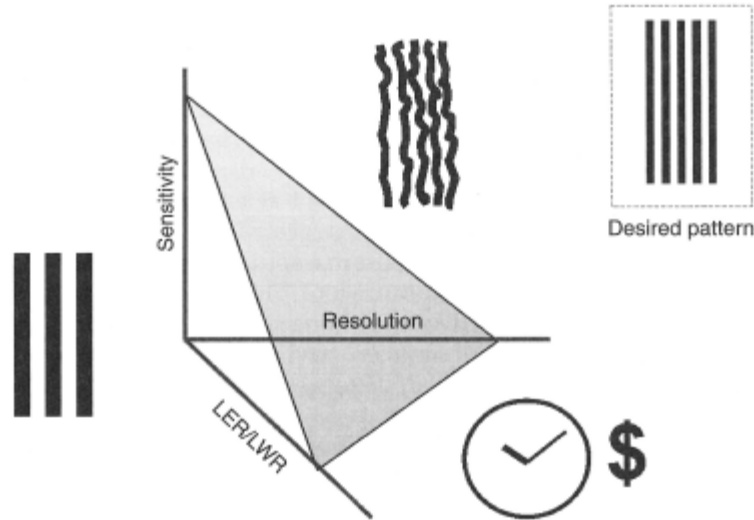


Fig. 15. The so-called RLS Triangle, a surface specific to a particular resist chemistry platform [10]. A better performing resist would overall have the surface closer to the origin: it can perform better in all three categories simultaneously.

2.2 Sources of LER

Line-edge roughness (LER), causes many degradations to device performance. I-V characteristics are strongly affected by gate length- which is mostly determined by the half-pitch critical dimension (CD), but is also effected by LER [59-63]. Traditional causes of LER comes from primarily 3 sources: resist chemistry LER (also comprising shot noise effects), mask LER, and mask roughness induced LER.

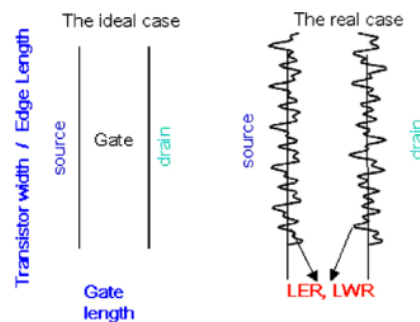


Fig. 16. Top down view of a gate showing how LER can lead to degradation in transistor performance [64].

As discussed in some detail in the previous section, resist chemistry is a large factor of LER. Current state-of-the-art resist platforms reach a minimum at 3nm LER performance (comprising all 3 LER sources) [65]. There are also photon shot noise contributions that need to be considered. The shot noise is wrapped up in the innate LER deprotection blur, which serves as the fundamental counting bin [66]. For EUV, we can expect that a 1x1nm area will see only 2-3 photons [57]. As soon as we introduce diffusion length (image blur), this sets the effective counting bin size for photon statistics, which follow a Poisson distribution with a $1/\sqrt{N}$ variation.

With bigger counting bins, there are more absorbed photons per bin, and better counting statistics; so apart from the natural smoothing benefits of image blur, we also achieve reduced LER through photon shot noise. If however, the blur becomes so large relative to the pitch such that the chemical contrast is degraded, we gain no further benefit in LER. Studies show this occurs for diffusion lengths of about 0.2 times the pitch, beyond which the LER shows no further improvement, but there is decreasing exposure latitude [57].

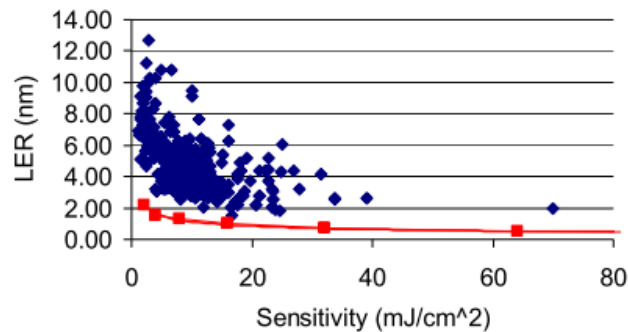


Fig. 17. Scatter plot of LER as a function of resist sensitivity and prediction of photon noise induced LER based on stochastic modeling [65].

The resist LER component can also be reduced through introduction of a base quencher to the resist formulation. The base quencher serves to increase the chemical contrast by increasing the counting statistics of both photons and acids. Diffusional effects can degrade the chemical contrast, but if counting statistics are increased by adding base, the small amounts of photoacids that have diffused to regions where they shouldn't be will not be able to effectively deprotect the polymer. This works because virtually all the polymer must be deblocked in order to cause the solubility differential, so it neutralizes low levels of the photoacids [8].

Mask LER, or the LER intrinsically on the mask pattern, is the second significant contributor to LER and will transfer almost directly down to the wafer, according to the line-edge transfer function (LTF). The LTF differs from the traditional MTF due to LER's complex 2D nature, and exhibits a faster fall off at higher spatial frequencies [67-68] (see Figure 18). For the 22nm node, mask LER is expected to contribute 2nm LER to the total budget.

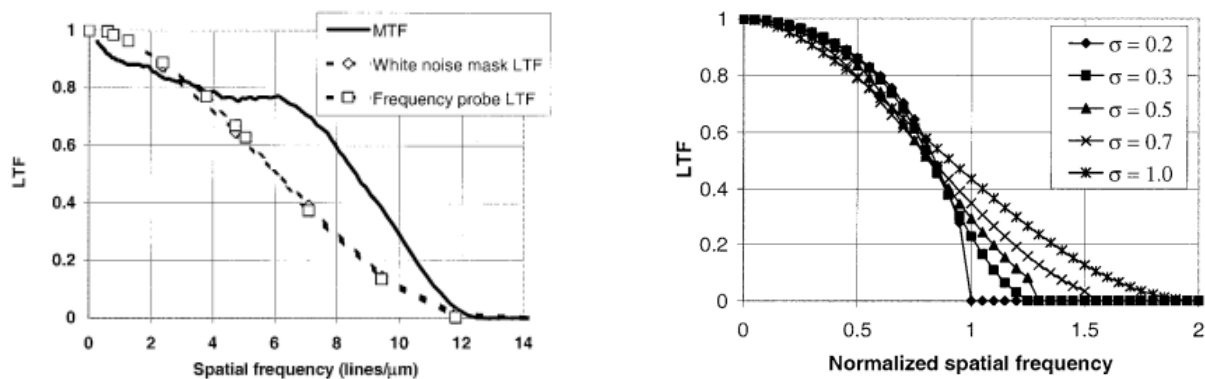


Fig. 18. LTF vs MTF (left), and LTF (right) for various σ values as a function of the normalized spatial frequency (normalized to the coherent cutoff frequency) [67].

As described below, the third significant contributor to LER is something not seen at optical wavelengths and is purely an effect due to the extremely small wavelength of EUV: mask roughness induced LER.

2.3 Mask roughness induced LER

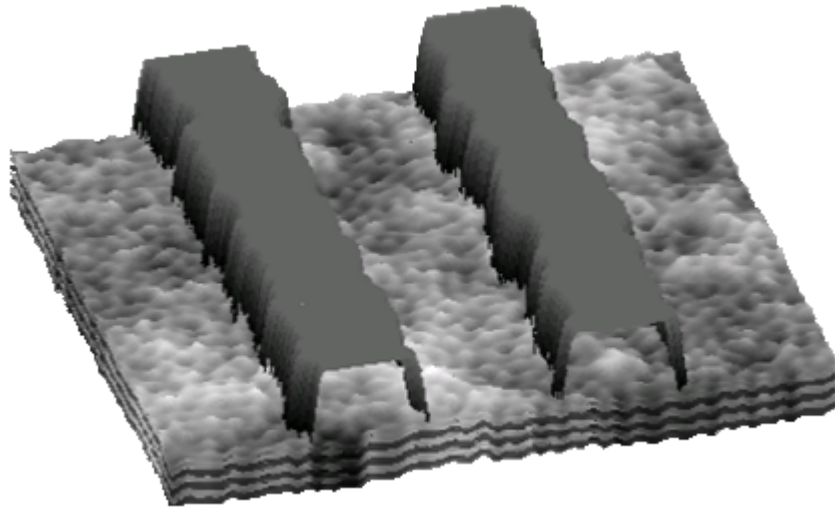


Fig. 19. A simple schematic (not to scale) illustrating the difference between absorber LER and mask surface roughness [69].

2.4 Mask roughness couples to speckle

At 13.5nm illumination wavelength, suddenly phase variations induced by optical path differences are significantly different than at 193nm: to be precise, by a factor of 14. As we will see, small surface deviations not large enough to be defects, but statistically spread across the surface of the mask, cause significant phase deviations on the outgoing wavefront that in turn, couple to speckle at the aerial image plane and cause LER.

2.4.1 Coherence enables speckle

Considering the fundamental definition of coherence, σ , set by a source of lateral coherence width l_{coh} and an objective of resolution δ_{obj} , we have

$$\sigma = \delta_{\text{obj}} / l_{\text{coh}}$$

in the object plane, where the resolution of the objective is the point spread function of a delta function object, and the lateral coherence width is the minimal size over which we can observe some modulation in coherence [69].

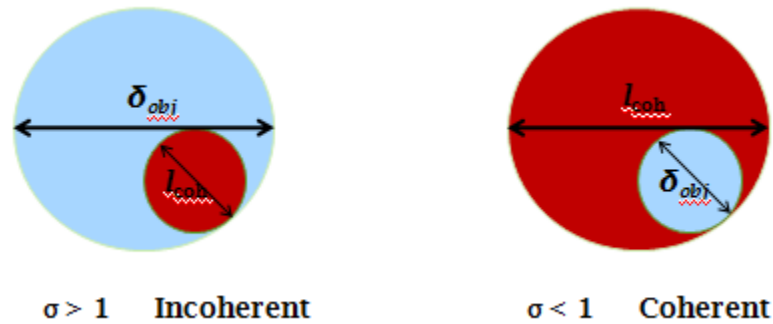


Fig. 20. Simple regimes of coherent and incoherent illumination illustrated physically in the object plane.

We can understand better the meaning of this simple equation by looking at two basic regimes in a geometrical sense. When $\sigma > 1$, we have the “incoherent” regime. Physically, this means that the resolution of the objective is larger than the lateral coherence width of the source, and we cannot peer inside that area to see coherent interactions taking place. On the other hand, as soon as we go to $\sigma < 1$ we enter the partially coherent regime where suddenly the resolution of the objective is smaller than the lateral coherence width of the source and we can see coherent interactions taking place. It is under partially coherent illumination (as is the case in all litho tools) that we are *able* to see speckle effects.

2.4.2 Speckle caused by mask surface roughness

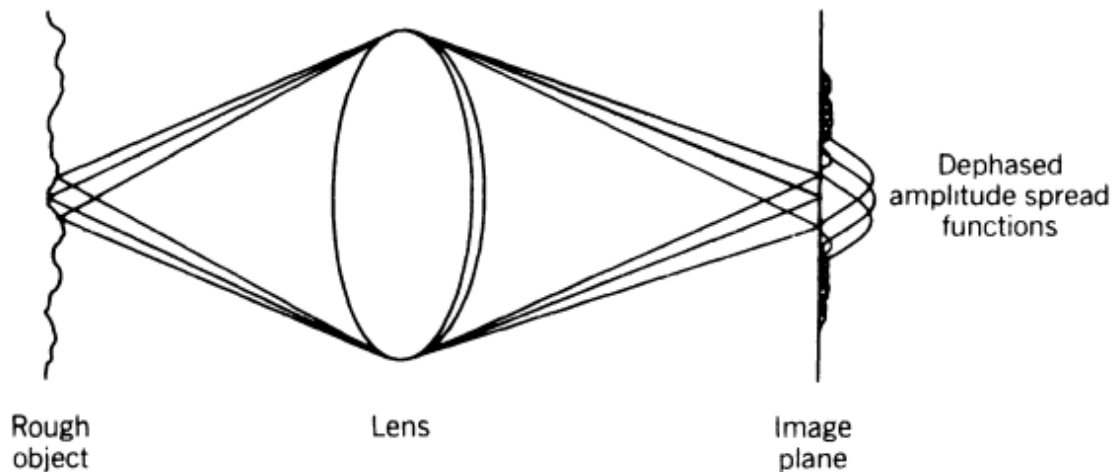


Fig. 21. Scattering points on a rough object couple to many dephased amplitude spread functions in the aerial image, or speckle [70].

The speckle itself, however, is caused by mask surface roughness that is rough on the scale of an optical wavelength. The wave reflected from such a surface consists of a superposition of a multitude of amplitude spread functions, each arising from a different scattering point on the object.

Although it is not impossible to describe a mask completely by every detail of its surface roughness, it is more useful to describe it in terms of its macroscopic properties. By doing so, its speckle statistics are shared by a much wider set of masks, all differing in microscopic detail, but sharing these macroscopic properties. To elucidate the macroscopic properties of importance, let us picture roughness as random “bumps” covering the surface of the mask. The optical path length difference on the phase wavefront (termed ‘phase roughness’ PR) induced by each scattering point or bump can be related to the 2D map of surface height deviations characterized by a statistical height deviation, called replicated surface roughness (RSR). Since the multilayer mirror is built up through many layer depositions which are conformal to one another, and hence, “replicated”, the whole roughness of the multilayer stack is well represented just by the top surface map, and the RSR, thus truly affecting the phase of the reflected beam.

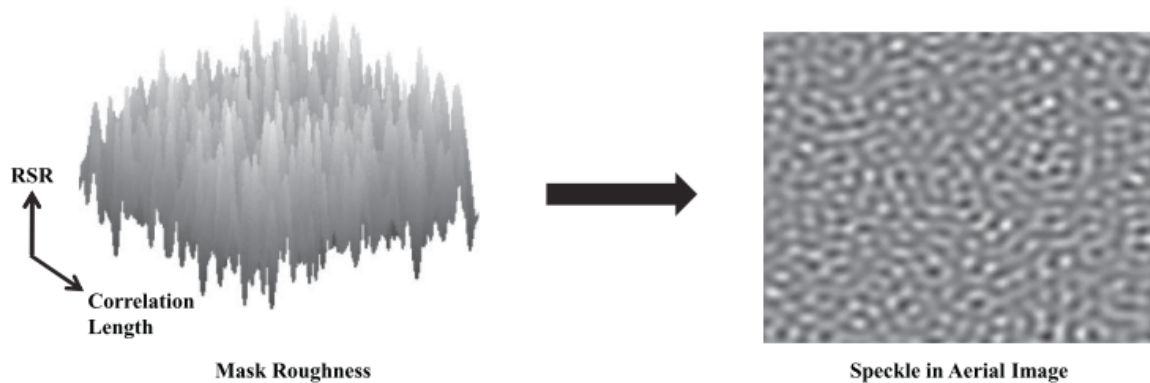


Fig. 22. Roughness on the mask (exaggerated in image) leads to speckle in the aerial image [71].

The phase roughness of the mask can be related to this geometrical height deviation by a simple equation:

$$PR = 2 * 2\pi * RSR / \lambda$$

with an additional factor of 2 for the reflective nature of EUV masks. From a simple calculation, we can see that a height deviation of 100pm results in 5° of phase shift. Typical mask surface specifications are about this: worse case scenarios are around 230pm, and as we will see in coming chapters, the ideal is 50pm [4].

The other property of concern is the extent to which the bumps are laterally self-similar on the mask. This property is characterized by the correlation length. It is a measure of the extent to which the roughness is dephased laterally across the wavefront with respect to itself, and it governs the spatial frequency content of the roughness on the mask. Thus, for example, greater height variations (RSR) and lesser self-similarity across the mask (correlation length) mean that the mask is “rougher” in a statistical sense. The Fourier transform of such a rough mask yields the power spectral density (PSD) graph that characterizes the statistical nature of the mask. As can be seen in Figure 23, the height of the PSD curve is normalized to the overall level of roughness present on the mask (the RSR). The “knee” in the log-log plot is located at the correlation length. Additionally, there is one other statistical factor of importance besides the RSR and the correlation length in characterizing the mask surface roughness properties. Called the roughness exponent, or sometimes the fractal dimension, it is a measure of the slope of the

PSD graph following the “knee”. Formally, it is defined by $(m-1)/2$ [59], where m is the slope. The larger the slope, the more the integrated spectrum is concentrated in high spatial frequencies, or finer roughness. For most of the analysis presented in this thesis, we will consider a top-hat form of the PSD, implying a roughness exponent of infinity, where all the roughness is concentrated only in spatial frequencies strictly below the correlation length of the roughness.

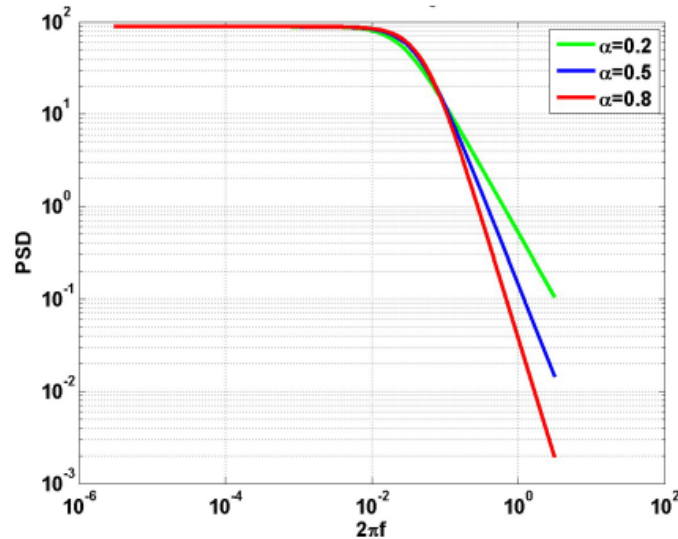


Fig. 23. A typical approximated PSD curve of roughness illustrating the correlation length “knee” feature, and varying roughness exponents, σ [62]. The overall level of the curve is normalized to the amount of RSR found by the integrated PSD.

By expressing mask roughness in terms of correlation length and RSR, and finally the roughness exponent, its macroscopic roughness properties are well determined. When combined with the parameters of the objective NA, coherence factor σ , and defocus, the speckle statistics can then theoretically be determined. For a given mask roughness, more coherent illumination will enhance the speckle problem, since adjacent points have greater ability to interfere. Although analytic solutions for the clear-field speckle are certainly feasible, dealing with system parameters such as aberrations (including defocus) considerably complicate the issue. Thus, the more practical approach is to use modeling to predict the speckle.

The resultant fields add with markedly different phases that result in a random walk in the field, and hence in intensity, at the image plane [69]. This is speckle: random intensity variations.

The random intensity variations in turn induce LER when the image is thresholded in the resist. The thresholding process starts with the map of the photon distribution given by the intensity right above the wafer plane (called the aerial image). Since the optical imaging process is imperfect, instead of a sharp transition from line to space, the image is much more smoothly modulating. To measure the quality of that image, lithographers take the slope of that image in log-space, to normalize out simple intensity scaling. This is called *image-log-slope* (ILS), and it is defined as $ILS = \partial \ln I / \partial x = \partial I / \partial x * (1 / I)$, across the horizontal position of the image. Physically, the ILS allows calculation of a given change in line-edge position (∂x), due to a change in intensity ($\partial \ln I$). This concept will be employed in the development of a simplified model of the mask roughness induced LER, where the image quality as given by the ILS will

determine how the small intensity perturbations due to speckle will cause the line-edge position to change.

2.4.3 A note on the difference between surface roughness on the mask and surface roughness on projection optics

Before investigating the effects of mask roughness induced LER, it is important to note that surface roughness on the mask and surface roughness on the optics are entirely different issues. Firstly, the mask is conjugate with the image plane, so these surface deviations on the object can be mapped directly to the image [24]. Secondly, surface roughness on the optics has been well studied, and shown that low spatial frequency roughness leads to figure errors (aberrations), mid spatial frequency roughness to flare, and high spatial frequency roughness to a loss in reflectivity [10]. The only way surface roughness on the optic can contribute to speckle at the image is if there is a large illumination area compared to the correlation length of the roughness in the pupil: then the coherence can build up. Since this is normally quite large, we end up with a large random walk where the projection optic-induced speckle goes as $1/\sqrt{N}$.

2.4.4 A note on the importance of mask surface roughness and absorber surface roughness from an LER perspective, and capping roughness

While variations in absorber surface roughness can also affect LER on the other side of the thresholded image, these variations are insignificant, even at EUV and for thin absorber thicknesses. Thin absorbers such as 50nm TaN will cause only an overall reflectance of about 3%, where the surface variations would account for a factor of about 1-3% of that (for RSR values of about 50pm, when the PR now takes into account the index of refraction for TaN). This is compared directly to the surface roughness of the bright area in between absorber regions, which nominally has a reflectance of 100%. Therefore, the induced LER due to absorber surface roughness is negligible (from a CD uniformity perspective, however, it should be taken into account [11]). Of greater concern is the choice material used for the capping layer that will induce additional phase roughness from refraction on top of the geometrical roughness. Simple calculations show [69] that Ru is in fact the worse choice inducing 6° phase deviation in a double pass through 1nm of material (requiring 0.44nm thickness to achieve an equivalent of 50pm RSR).

Capping Material	Double Pass Phase Shift per nm of material	Roughness Equivalent to 50 pm RSR*
Si	0.002°	730 nm
Ru	6°	0.44 nm
C	2°	1.25 nm

Fig. 24. Potential capping layer materials, and their equivalent phase roughnesses [69].

2.4.3 A note on the experimental aerial image verification of mask roughness induced LER

Studies have shown that 2D thin mask modeling results compare well to systematic trends in the experimental LER results [2]. Modeling was based on aberrations present in the actual optic and AFM measurements of a portion of the mask being imaged to the wafer, and assuming that mask roughness induced LER adds in quadrature to all other contributors, the fractional contribution to total observed LER is limited to less than 15%, with a systematic increase in that contribution as a function of focus and coherence. At the edge of focus, these effects can be large enough to account for the entire specified resist LER budget for the 22nm, unless very low roughnesses and coherence are used.

2.5 Current simulation methods for mask roughness induced LER

Current simulation methods for mask roughness induced LER are a tedious process. One must take the full 2D aerial image simulation of the complex, compound object of a rough mask superimposed with lines and spaces as a function of illumination coherence, optical aberrations, defocus, and mask roughnesses. Subsequently, one must analyze the data in an offline program to calculate the expected LER values. These simulations can take large amounts of time, and any shortcuts in decreasing time would be highly valuable to the industry to further increase turnover rate and understanding of mask roughness effects. Key aspects to reducing simulation time include the validity of thin mask modeling versus 3D (see below), and decoupling mask surface roughness from pitch values (the basis of the simplified model to be explored beginning in Chapter 3). A 3D model can take up about 12 hours to run versus 30 seconds for the thin mask modeling [72]. By decoupling mask surface roughness from pitch values, simulations can be sped up by a factor of however many feature sizes one wishes to simultaneously investigate.

2.5.1 3D simulations

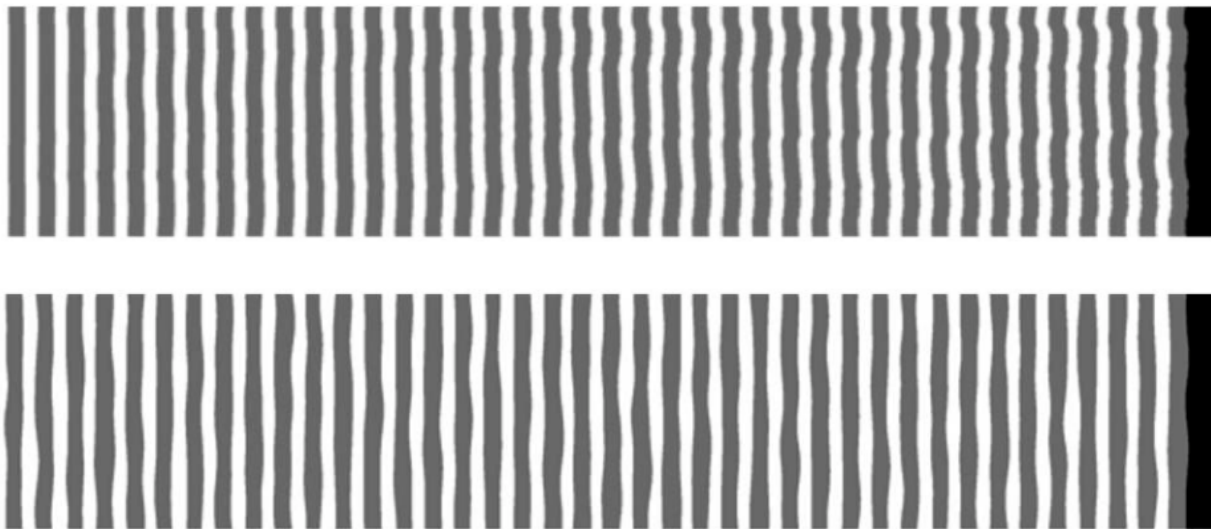


Fig. 25. (Top) Correlated interface roughness multilayer with uncorrelated thickness layer to layer, and (bottom) uncorrelated interface roughness and layer thickness [72].

3D finite-difference time-domain (FDTD) simulations of mask roughness require that the roughness be characterized for each layer of the multilayer mirror. Recent investigations looked at both conformal growth and non-conformal growth of the multilayer mirrors [72]. In the first case assuming conformal growth (a very realistic assumption as the multilayer deposition process has a point-spread function of its own [73], uncorrelated random thickness layers and perfectly smooth substrate and top surface roughness of 230pm, speckle contrast at -150nm defocus is 14%. If, however, the layers were completely non-conformal with each other, a dramatically lower speckle contrast of about 4% is observed. This case, however, is very unrealistic for the multilayer deposition process, and shows the importance of the replicated nature of the interface roughness in the multilayer in the formation of speckle [72]. Therefore, it is convenient in the 2D (thin mask) modeling to characterize just the top surface roughness to represent the whole multilayer, and this is called “replicated surface roughness”, or RSR.

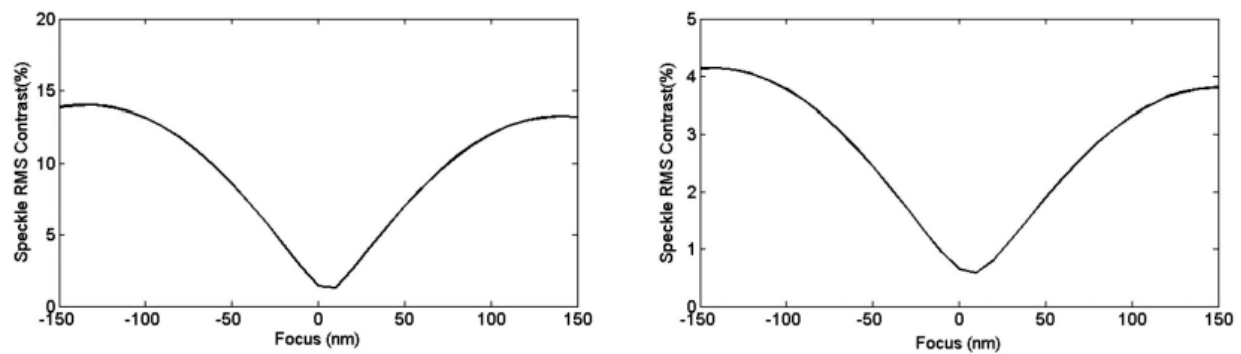


Fig. 26. 3D simulated speckle contrast curves expected for (left) correlated interfacial roughness, uncorrelated thickness layer to layer in the multilayer, and (right) uncorrelated interfacial roughness and thickness [72].

2.5.2 Thin mask modeling at EUV wavelengths and NA for practical surface roughnesses

In the same study, investigations show that differences between 2D thin mask modeling and 3D mask modeling by FDTD are minimal over a range of NA from 0.32, 0.4, to 0.5. With perfect conformal growth of the multilayer, at a roughness with rms height variation of 230pm (a severe but practical RSR figure) and correlation length of 125nm on the mask, comparisons between the 2D and 3D simulations confirm overall the validity of the thin mask modeling [71]. The 3D modeling, as expected, yields slightly lower speckle contrast than 2D by a couple percent, mainly due to uncorrelated thickness layer to layer which helps reduce the coherent addition of speckle from each layer. Position of the contrast rollover, however, remains in the same position between 2D and 3D, most likely due to perfectly correlated roughness between the layers. Despite the already very large increase in speed from 3D to 2D modeling, further speed increases promised by the redundant nature of speckle statistics around image features have a good potential. Such a model that decouples the speckle from the feature would not only provide a benefit in reducing this modeling redundancy, but also provide physical insight into the means by which speckle couples to LER, and into how it can be mitigated.

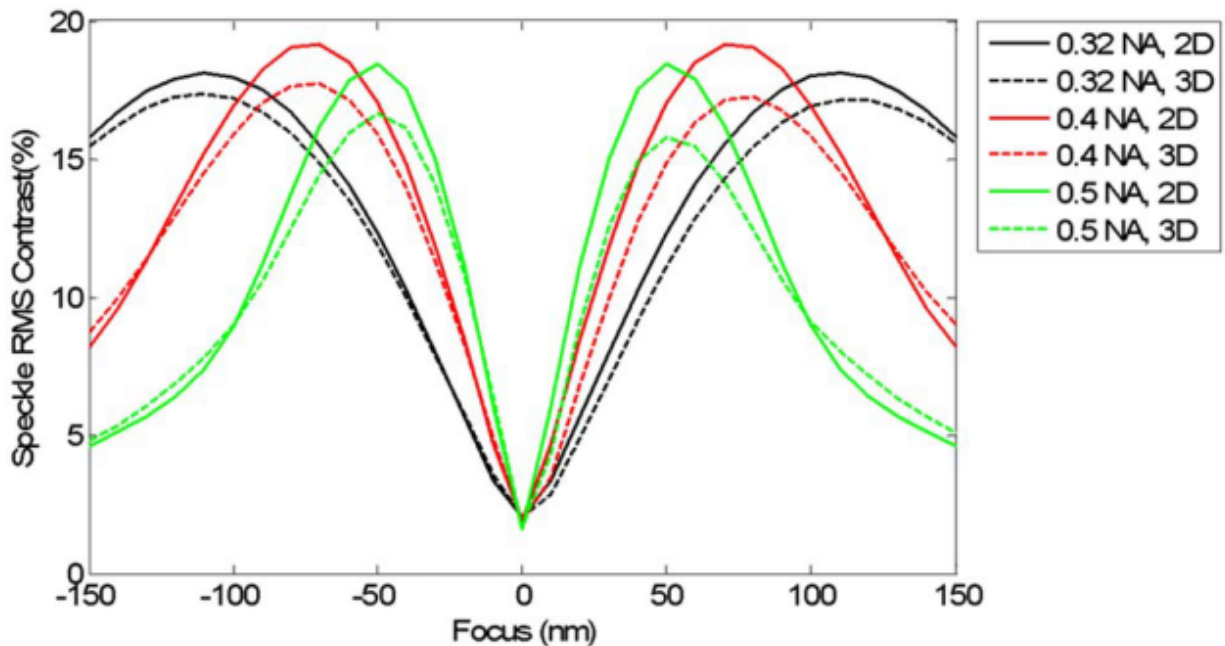


Fig. 27. Direct comparison of thin mask (2D) modeling to full (3D) simulations of mask roughness with correlated multilayer deposition [72].

2.6 Conclusions

EUVL faces many problems before its implementation. Most importantly; problems of source power, mask defects, and a suitable photo-resist platform. Mask roughness induced LER- an issue specific to EUV- pertains mainly to the final printing performance of the photo-resist, which is a small, but crucial piece of the puzzle to the solution of pushing the RLS triangle to better performance levels.

Because EUVL is a band-limiting imaging process (i.e., an aperture limits the spatial frequencies it passes), the mask surface roughness (which is geometrically related to phase roughness), is significant for EUV wavelength, and is directly coupled to speckle-induced intensity variations at the image plane, which can significantly alter LER measurements of the printed image. Moreover, because EUVL is dependent on reflective optics and masks, the geometrical relation of mask roughness to phase roughness is amplified by a factor of 2 due to reflection. As defocus is introduced, mask phase errors even further couple into intensity variation, or speckle. As expected, when coherence is increased, speckle is enhanced, and the mask phase error-induced speckle increases proportionately, and the mask roughness induced LER as well.

While thin mask modeling provides a tremendous boost in speed to simulating speckle contrast over 3D modeling without sacrificing much accuracy, there is still a strong motivation to provide an even faster means of predicting mask roughness induced LER by decoupling speckle contrast from the features. This is the basis of the simplified model, to be explored in the following chapter.

Chapter 3

Simplified Model

In this chapter, we explore the physicality between connecting speckle to line-edge movement through the use of image-log-slope (ILS). Using this concept, we formulate a simple equation for the prediction of mask roughness induced LER based on clearfield speckle for the mask surface roughness properties. To aid ourselves in this formulation, we first construct the model on a simple knife edge, then formalize the model at the end of the chapter. We will see the model provides a speed enhancement through the elimination of redundancy in modeling multiple feature types on top of the same speckle pattern.

3.1 Mapping Intensity Perturbation to Line-Edge Movement

As mentioned above, the mask surface roughness characteristics determine the clearfield speckle statistics, specific to the optical system and focus. By recognizing that speckle is fundamentally an intensity perturbation, we explore the use of the image-log-slope in mapping those incremental intensity changes to a corresponding movement of the line-edge.

3.1.1 Mask Roughness Induced Speckle as an intensity perturbation

Before investigating possible simplified methods to predict mask roughness induced LER, it is important to understand how it arises. As discussed in the literature [2,4,74-76] and therefore only briefly presented here, surface roughness on a reflective mask geometrically induces phase roughness on the wavefront that due to the reflection is a factor of two larger than the actual surface deviations. This effect has detrimental consequences for EUVL. Since the operating wavelength is nominally 13.5 nm, very small roughness on the multi-layer mask can significantly modulate the phase. While the lithographic process operates by reimaging the mask to the wafer, the process itself is band-limited, resulting in an imperfect replication of the mask object that is sensitive to the phase errors on it. Phase roughness on the mask results in many overlapping amplitude spread functions in the image plane that differ in phase from one to another, causing a complex interference pattern, the strength of which is modulated by the coherence factor. These interference events manifest themselves as intensity variations, or speckle, at scales down to the resolution limit of the objective [70].

It is apparent that speckle is a complex phenomenon. However, it is a statistical effect whose macroscopic properties can be largely described by specifying the objective NA, coherence factor σ , defocus, and, of course, mask roughness. Ultimately, it is essential to recognize that speckle is an intensity perturbation: a random walk in the electric field, and hence, also in intensity.

3.1.2 ILS as a mapping from change in intensity to line-edge movement

Of greatest interest, however, is the LER and not the speckle. The strength of how the speckle couples to LER is determined by the image-log-slope (ILS). Typically used as a metric of image quality, it measures the slope of the aerial image intensity transition across the edge of features present on a mask; e.g. from line to space. Essentially, it is the change in intensity over change in position across the edge. By definition, it is

$$ILS = \frac{d \ln I}{dx} = \frac{1}{I} \frac{dI}{dx} \quad (1)$$

where the intensity, I , is the threshold at which the ILS is evaluated. It is dependent on the objective NA, coherence factor σ , CD, and defocus. A higher ILS means that for any intensity variation (e.g., through speckle), the resulting change in line-edge position will be small in comparison to a lower ILS value. Therefore, a higher ILS is desirable, from the perspective of minimizing sensitivity to mask roughness.

Noting that movements in line-edge, dx , are directly related to the 3-sigma definition of line-edge roughness, we can formalize the relation between speckle statistics and LER as

$$LER = 3 \times dx = 3 \times S \times \frac{1}{Intensity \times ILS} \quad (2)$$

3.1.3 Simplified Model Schematic

Current methods to predict mask roughness induced LER involve conducting full 2D aerial image simulations in commercially available software (such as PROLITH [77] or Panoramic [78]), followed by extracting the LER from the computed aerial image through offline analysis using a software package such as SuMMIT [79]. As stated earlier, this method is time consuming and cumbersome.

Our goal instead, is to simplify the LER modeling process by using simplified form of Eq. 2. The power in this simple equation is not in any new formulation, but in the method of implementing it. By looking at Eq. 2, we can break-up the problem into smaller parts. Consider an imaging system of given objective NA. Instead of doing 2D aerial image simulations for each process parameter individually, we can minimize this time-consuming process by only conducting a one-time 2D aerial image simulation through focus on a clear-field rough mask to get the illumination- and mask roughness-specific clear-field speckle. We can then couple this speckle to LER by using fast 1D aerial image simulations (e.g., using PROLITH) to get the feature- and illumination-specific ILS as it varies through focus. From here, the full parameter space can be reached by analytic extension. A comparison schematic of the two methods is shown in Fig. 28.

There are two distinct advantages to such a formulation. Firstly, it provides a straightforward, tractable simplified solution to computing mask-roughness-induced LER that is fast. Secondly, there is no need for an exhaustive list of 2D aerial image simulations for every mask pattern to be considered.

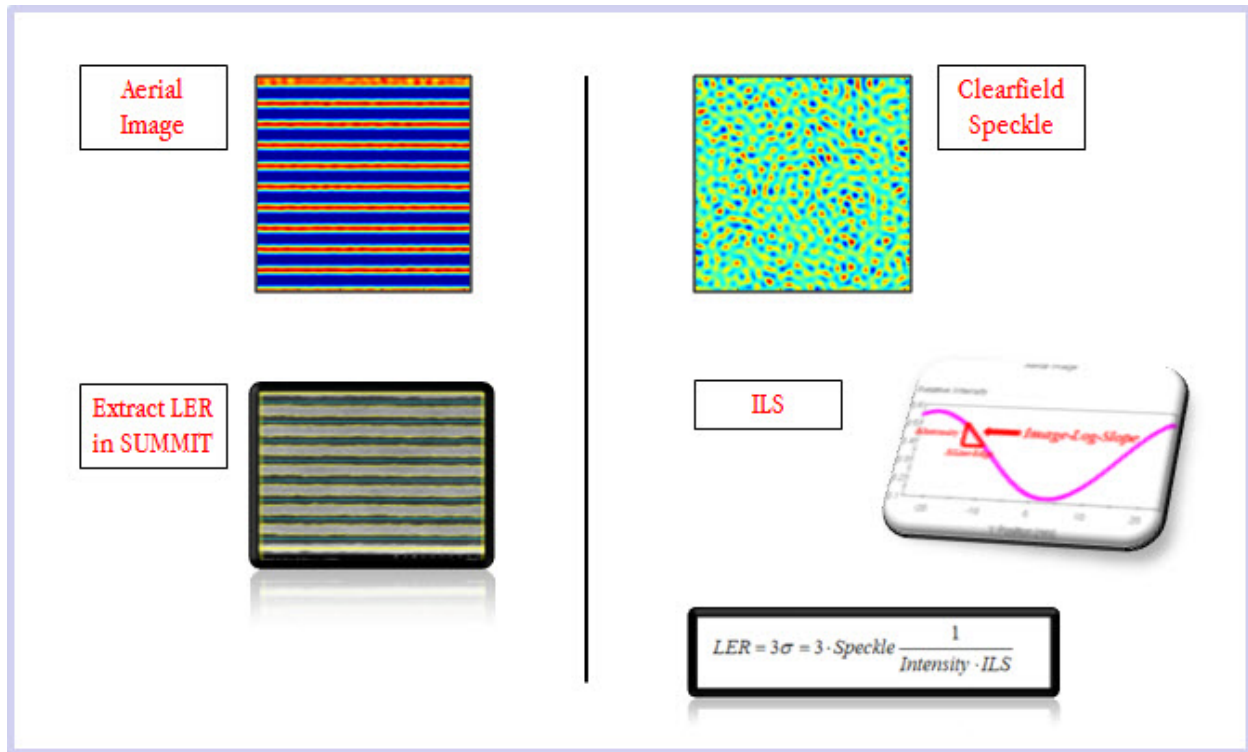


Fig. 28. A comparison schematic of the traditional method and the simplified method to get the mask roughness induced LER.

3.2 Mismatch: Line-edge speckle vs. Clearfield Speckle

Our first attempt at implementing the model, as we shall see, was unsuccessful. The key reason lies in the difference between the clearfield speckle and the speckle actually at the thresholded line-edge, which actually causes LER. Analysis shown below indicates that the clearfield speckle can be scaled by the intensity at the threshold, to give the line-edge speckle and correct the model.

3.2.1 Modeling method

To verify the validity of our approach, we need to compute the LER from both methods illustrated in Fig. 2 and compare them. Both used scalar aerial image modeling software based on the equations of partially coherent image formation [70]. Commercial software with similar capabilities include PROLITH [77] and Panoramic [78]. We modeled an aberration-free optical system with $NA = 0.32$. Again, the low NA allows for scalar and thin mask modeling. Following a similar numerical analysis approach used elsewhere [2], we constructed a statistical representation of a clear rough mask as a random phase object, whose pure phase distribution is determined from the geometric path length differences imparted by the rough surface of the mask. We started with a randomly generated mask object that was 1024×1024 pixels at $1 \text{ nm} /$

pixel with 1:1 imaging to the wafer plane. Using this process we generated an entire set of masks all with an RSR of 50 pm, and with a variety of correlation lengths (5, 13, 20, 26, 32, 42, 47, 61, 68, 83, 96, 106, 127 nm). In order to build up a significant statistical ensemble, we created 10 random realizations of the mask for each RSR / correlation length pair. Assuming a wavelength of 13.5 nm, we converted each topographic surface to a phase perturbation. This set of masks was the starting point for the two approaches we wish to compare: the traditional method and the proposed simplified one.

To reproduce the traditional method which calls for calculating the LER directly from aerial-image simulations, we overlaid (multiplied) each clear-field rough mask realization with an ideal binary amplitude 50 nm line-space pattern.

We carried out the simulations through focus for 4 different disk illuminations: coherence factors $\sigma = 0.15, 0.25, 0.50,$ and 0.75 . We then extracted the LER in SuMMIT [79], using only nested features for LER analysis, avoiding the outer 200 nm border. We took care to set the binary threshold properly for each sigma value to provide proper sizing of the 50 nm lines at best focus. This was done for each random realization of each mask to build up the statistics. Assuming the process is ergodic, we could have just as easily used a larger mask with larger lengths of lines instead of numerous independent realizations. However, due to memory constraints, our chosen method is the preferred one. The LER data from this traditional approach is now ready for comparison to the new simplified method.

For the simplified method, we modeled each random realization of the clear-field mask under the same illumination conditions to get the clear-field speckle statistics. We then calculated the ILS using fast 1D aerial-image simulations in PROLITH [77] for our pattern of lines and spaces for each illumination condition. Finally, using the proposed solution to mask roughness induced LER described above, we analytically calculated the LER.

It is important to note that the power of the simplified approach lies in the one-time intensive aerial-image simulations of the clear-field speckle statistics. Once calculated, they are done. By using feature-specific ILS to couple clear-field speckle to LER in the aerial image, we can analytically extend the LER analysis to an arbitrary set of features with great ease, and reduce redundancy.

3.2.2 Initial result

Fig. 26 shows simulated LER results for one illumination setting, $\sigma = 0.15$. The trends for each correlation length show fairly constant slopes through focus with no crossover between them. This pattern is consistent for all other illuminations as well. It is therefore possible, for clarity, to look at just one defocus setting for comparison of the simulated LER to the simplified approach.

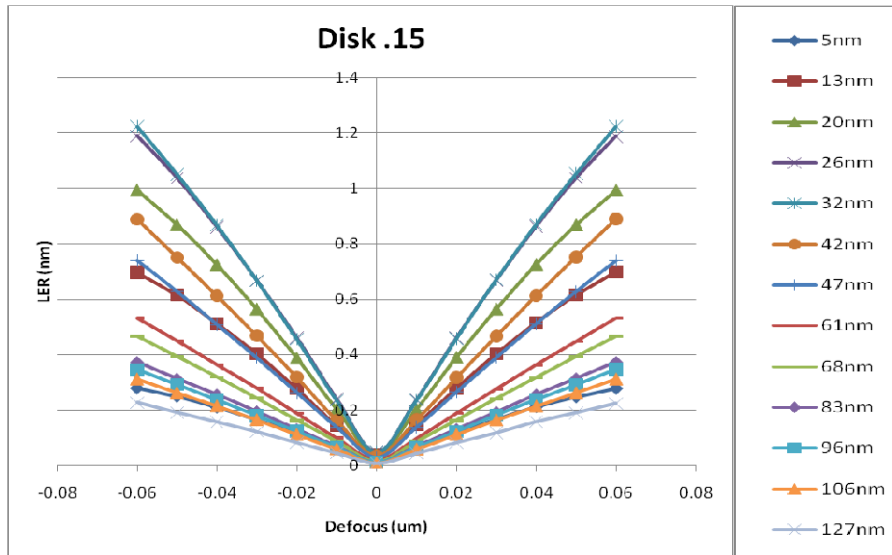


Fig. 29. Simulated LER data through focus for 50 nm lines and spaces, RSR 50 pm, disk of $\sigma = .15$ illumination, for a variety of correlation lengths.

Our first attempt to verify the simplified method against the full calculation did not provide a good match (see Fig. 30). This suggests that the clear-field speckle differs significantly from the speckle in the presence of lines and spaces. To assert this, we directly compared the intensity standard deviation of the clear-field aerial image and that of the feature-specific one (taken both at the line-edge and in the middle of the space). In this calculation, we used the aerial image results from the simulated LER method to investigate the feature-specific speckle. We took the standard deviation of the intensity in the direction parallel to the lines at two horizontal positions: in the middle of the space and at the line-edge (see Fig. 31 for a comparison of the two methods). We also took care to evaluate the line-edge intensity standard deviation at the same threshold value used for calculating the simulated LER. The results show great disparity (see Fig. 32). It is apparent that the presence of features affects speckle in a complex way.

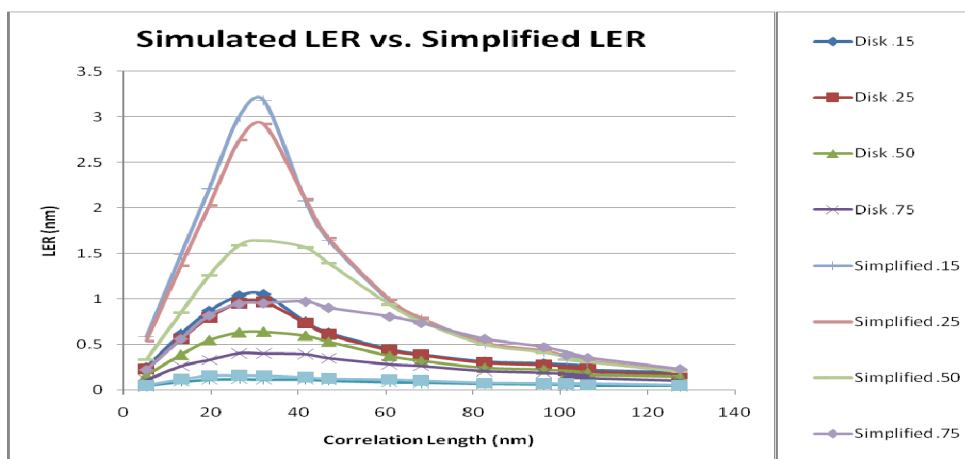


Fig. 30. Our first attempt provided a poor match. Simulated LER vs. Simplified LER (using clear-field speckle) at -50 nm defocus setting for a variety of correlation lengths and a variety of illumination settings.

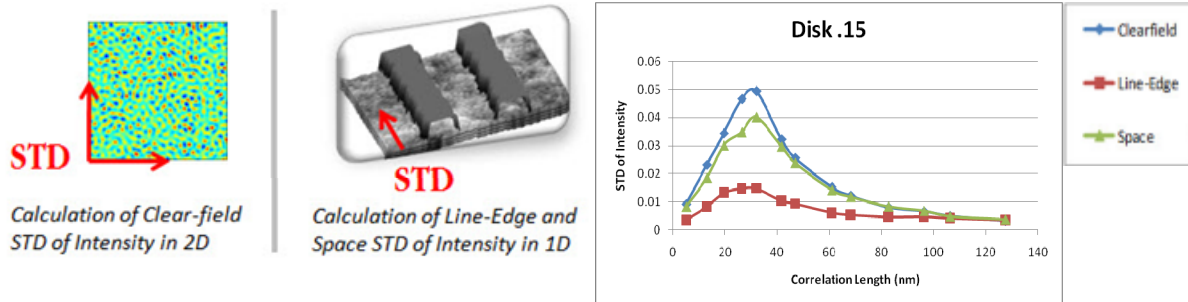
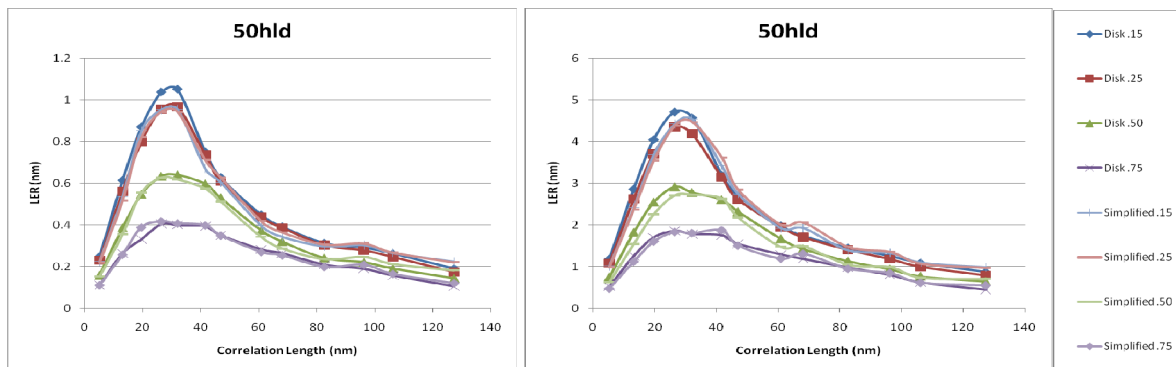


Fig. 31. (Left) Clear-field speckle vs. Line-edge speckle calculation method.

Fig. 32. (Right) STD of Intensity of Clear-field vs. at the Line-edge and middle of the Space for 50 nm lines and spaces with disk illuminations $\sigma = .15$, RSR 50 pm, for a variety of correlation lengths at -50 nm defocus

3.2.3 Line-edge speckle

We concluded then, in its most general form, the simplified method must use the speckle at the line-edge. To prove its validity, we attempted the comparison between the full calculation and simplified method once again, but this time using the standard-deviation of intensity at the line-edge [80]. The results are shown in Fig. 33 (top-left) are at a defocus setting of -50 nm and give an excellent match. We repeated the entire data set for 40 nm lines and spaces and 22 nm lines and spaces, the results of which are shown in Fig. 33. We also repeated the entire data set on 50 nm and 22 nm lines and spaces for a different RSR value of 230 pm, shown in Fig. 34. For Fig. 34 at 22 nm lines and spaces, the defocus setting was changed slightly to -30 nm, due to corrupted image files further out of focus. In all cases, there was good agreement between the full and simplified LER methods. In Fig. 34 for 22 nm lines and spaces at 230 pm RSR, the match between the two methods agrees less well for higher correlation lengths, but we believe this is a simple artifact of the statistical nature of the speckle. Since the line-edge speckle calculation used only one line-edge on one aerial image, this could likely be improved by considering a larger dataset.



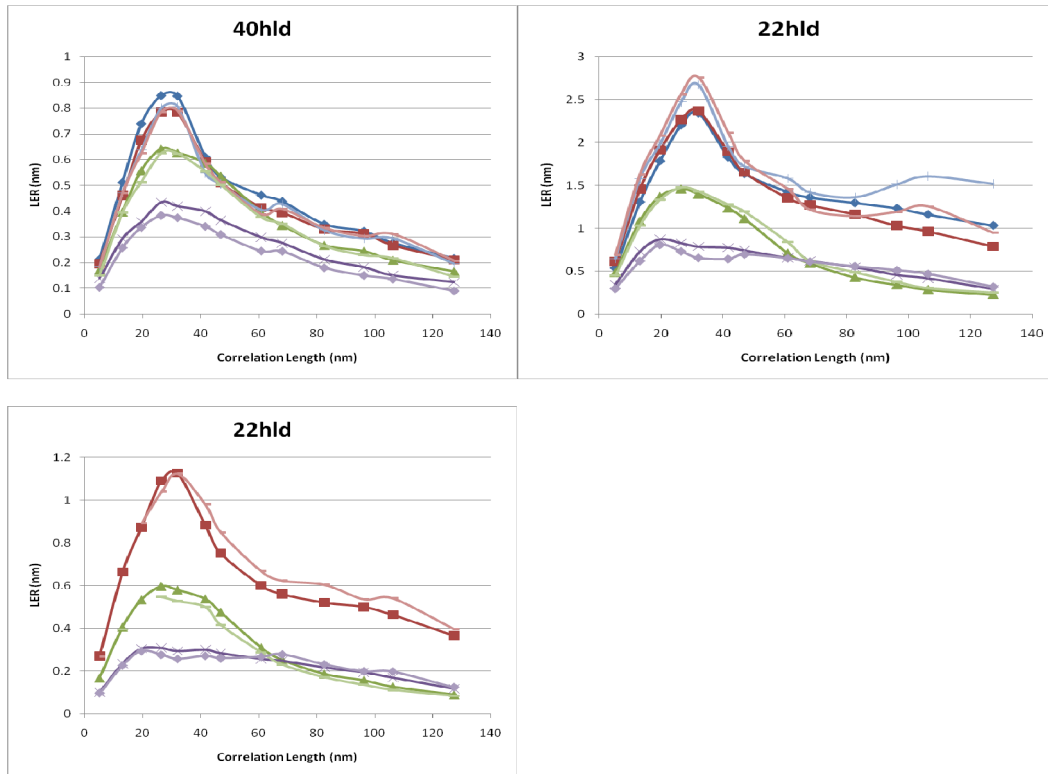


Fig. 33. Simulated LER vs. Simplified LER (using speckle at Line-edge) for RSR 50 pm, a variety of illuminations, a variety of correlation lengths, at a defocus of -50 nm, for (top-left) 50 nm, (center-left) 40 nm, and (bottom-left) 22 nm lines and spaces (where hld is horizontal line dense, or lines and spaces).

Fig. 34. Simulated LER vs. Simplified LER (using speckle at Line-edge) for RSR 230 pm, a variety of illuminations, a variety of correlation lengths, (top-right) at a defocus of -50 nm for 50 nm lines and spaces, and (bottom-right) at a defocus of -30 nm for 22 nm lines and spaces.

3.2.4 Knife-edge rough object

Since the power of the simplified method lies in applying the clear-field speckle formulation and *not* the feature-specific line-edge one, we investigated how to functionally relate the one to the other. If we found some way to do so, then we could maintain the clear-field speckle formulation with perhaps some adjustment parameter. Assuming the relative intensity variation in the case with lines to be constant and equal to the relative variation in the clear-field speckle, we can approximate the absolute intensity variation (speckle) at the edge to be the absolute clear-field speckle scaled by the relative intensity at the edge. Thus, if the edge is defined at a threshold value of 30%, for example, we would assume the absolute speckle at the edge to be 30% of the absolute speckle in the clear-field. To test this assumption, we constructed a knife-edge structure on top of a clear-field rough mask of RSR 50 pm, using one of the previously generated realizations of the clear rough mask for the 32 nm correlation length case (see Fig. 35). We carried out aerial image simulations for the same 4 disk illuminations examined above, and extracted the resulting LER. We then calculated the clear-field speckle and the ILS, in a similar manner to that described above, and repeated the calculation of LER using the clear-field speckle as in Eq. 2, but where the clear-field speckle was scaled by the line-edge intensity (found in PROLITH[77]). The numerical results are seen in Fig. 10, and show that the scaled clear-field

speckle formulation actually provides a better agreement with the simulated LER values than does the simulated line-edge speckle formulation, for the case of the knife-edge. We believe this is because the standard deviation of the line-edge captures not only the line-edge speckle, but deviations caused by the LER itself as well, resulting in an overestimation of the LER.

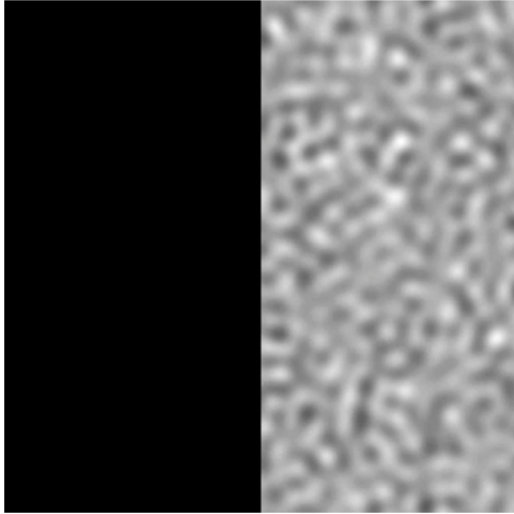


Fig. 35. Knife-Edge on rough clear mask with RSR 50 pm and correlation length of 32nm.

Disk Illumination	$\sigma = 0.15$	$\sigma = 0.25$	$\sigma = 0.50$	$\sigma = 0.75$
Clear-field Speckle	0.0493	0.0444	0.0256	0.0129
ILS	92.3	90.7	83.6	72.5
Intensity at line-edge	0.272	0.266	0.284	0.305
LER from Eq. 2	1.45	1.3	0.87	0.54
Simulated LER	1.2	1.1	0.7	0.4

Fig. 36. Numerical results for the calculation of LER based on the simplified model in comparison with the LER calculated from the full 2D aerial image simulation.

We then repeated the comparison between simulated LER and the LER calculated from the simplified model, shown in Fig. 33 (top-left). This time, however, we used the new scaled clear-field speckle for the simplified model. The results shown in Fig. 37 show a good match. The simplified model seems to consistently underestimate the simulated LER by only a small amount for all illuminations, approximately 0.1 nm at most.

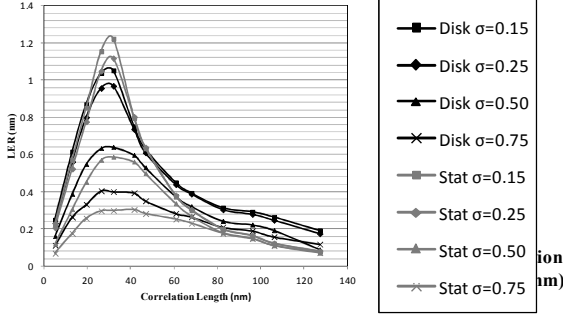


Fig. 37. When the clear-field speckle is scaled by intensity at the line edge, the LER based on the simplified model matches the simulated LER well. For all illuminations, the LER is consistently underestimated by only a small amount, approximately 0.1 nm at most. This is for 50 nm lines and spaces with an RSR 50pm at a defocus of -50nm, for a variety of correlation lengths and illumination settings.

3.2.5 New formulation

Let us formalize the simplified model: Given NA, illumination conditions, and mask roughness characteristics (well defined by replicated surface roughness (RSR) and correlation length), a one-time 2D aerial image can be conducted to calculate the clear-field speckle statistics through focus. This can be done by taking the rms-deviation of the resulting clear-field intensity distribution, which in the notation below, is called S . The total incident clear-field intensity, is here called I_{CF} . The details of the aerial image modeling of a rough mask are described elsewhere [8], and can be done in the previously mentioned commercial software packages PROLITH [77] and Panoramic [78]. This speckle can be coupled to any feature size using a fast 1D aerial image simulation of the image-log-slope (ILS), again, within the same software utilities. The ILS should be evaluated at a relative percent threshold to produce properly sized-to-target features at zero defocus. This is called p in the notation below. In terms of absolute intensity, the intensity at the threshold, here called I_{th} , is then

$$I_{th} = I_{CF} \times p. \quad (1)$$

From the 1D aerial image, the maximum intensity in the middle of the space can be found, which is here called I_{max} . Using this information and the fact that speckle scales with intensity [2], the speckle at the line-edge can be calculated directly. In absolute intensity terms, the speckle at the line-edge, here called S' , can be found by

$$S' = \frac{S}{I_{CF}} \times \frac{I_{max}}{I_{CF}} \times I_{th}. \quad (2)$$

Finally, by dimensional analysis, it can be shown that the 3-sigma LER in terms of absolute intensity can be calculated by

$$LER = 3 \times S' \times \frac{1}{I_{th} \times ILS}. \quad (3)$$

The numerical analysis to be followed is similar in approach to that used elsewhere [2,71]. The rough clear mask is statistically represented as a random phase object with a pure phase distribution determined by the geometric path length differences imparted by the rough surface of the mask. Starting with a randomly generated mask object that was 1024×1024 pixels at 1 nm / pixel and 1:1 imaging to the wafer plane that represents a geometric height map, the replicated surface roughness (RSR) value is to be set by appropriately scaling the standard deviation of this original mask object. The other surface roughness parameter of interest is the correlation length, which is to be calculated by taking the FWHM of the autocorrelation of the resulting mask object. This process should be repeated to generate an ensemble of 10 random realizations of the clear rough mask, all with an RSR and correlation length of interest. Given an illumination wavelength of 13.5 nm for EUVL, each topographic surface should then be converted to a phase perturbation.

A one-time 2D aerial image simulation (using either PROLITH [77] or Panoramic [78]) through focus should be conducted based on the NA of the optical system and the type of illumination conditions of interest. The clear-field speckle statistics (S in the above formulae) can then be calculated by taking the standard deviation of the resulting clear-field intensity distribution of the rough mask, and averaging across the ensemble. The input intensity in this aerial image simulation of the clear-field is the intensity normalization factor, I_{CF} .

For the particular critical dimension of interest, a fast 1D aerial image simulation should be done (for example, using PROLITH [77]), using the appropriate parameters of NA of the imaging optic and illumination conditions through focus. The feature should be thresholded to yield target CD at best focus. This threshold value is the p seen above. Although this value drops out of the final LER equation explicitly, it is implicitly present in the ILS value, which, as the next step, should be calculated at this threshold value. Finally, the maximum intensity modulation value can be calculated by looking at the aerial image intensity as a function of horizontal position at the appropriate defocus value. The maximum intensity value will occur approximately in the middle of the space for a horizontal line dense structure.

3.3 Conclusions

A simplified solution exists for predicting mask roughness induced LER.

The power of the simplified solution lies in being able to use the clear-field speckle formulation, where there is no need to repeat intensive 2D aerial image simulations for each specific feature. A one-time clear-field rough mask simulation for the illumination of interest will suffice, scaled by the intensity at the line-edge, with fast 1D aerial image simulations of the ILS to couple LER to any specific feature desired. This clear-field speckle formulation of the simplified solution provides a fast and tractable means of quickly calculating the mask roughness induced LER.

Chapter 4

Simplified Model Verification Part I

In this chapter, we verify that the newly constructed simplified model works for on-axis illumination conditions, for dense lines and spaces, down to the 22-nm half-pitch, as well as isolated ones, for higher NA, long correlation lengths, and different roughness exponents.

4.1 Verification on dense lines and spaces

We modeled an aberration-free optical system with $NA = 0.32$, but extended our set of rough masks all with an RSR of 50 pm to have a variety of correlation lengths (5, 13, 20, 26, 32, 42, 47, 61, 68, 83, 96, 106, 127 nm). In order to build up a statistically significant ensemble, we created 10 random realizations of the mask for each RSR / correlation length pair. This set of masks was the starting point for the two approaches we wish to compare: the traditional method and the proposed simplified one.

To reproduce the traditional method which calls for calculating the LER directly from aerial-image simulations, we overlaid (multiplied) each clear-field rough mask realization with an ideal binary amplitude 50 nm line-space pattern.

We carried out the simulations through focus for the same four disk illuminations used above: coherence factors $\sigma = 0.15, 0.25, 0.50, \text{ and } 0.75$. We then extracted the LER in SuMMIT [79], using only nested features for LER analysis, avoiding the outer 200 nm border. We took care to set the binary threshold properly for each sigma value to provide proper sizing of the 50 nm lines at best focus.

Fig. 38 shows simulated LER results for one illumination setting, $\sigma = 0.15$. The trends for each correlation length show fairly constant slopes through focus with no crossover between them. This pattern is consistent for all other illuminations as well. It is therefore possible, for clarity, to look at just one defocus setting for comparison of the simulated LER to the simplified approach.

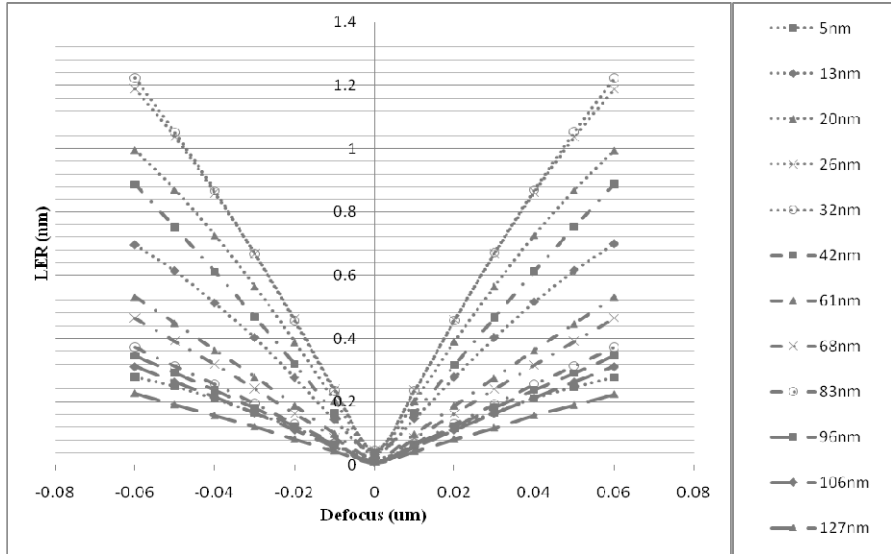
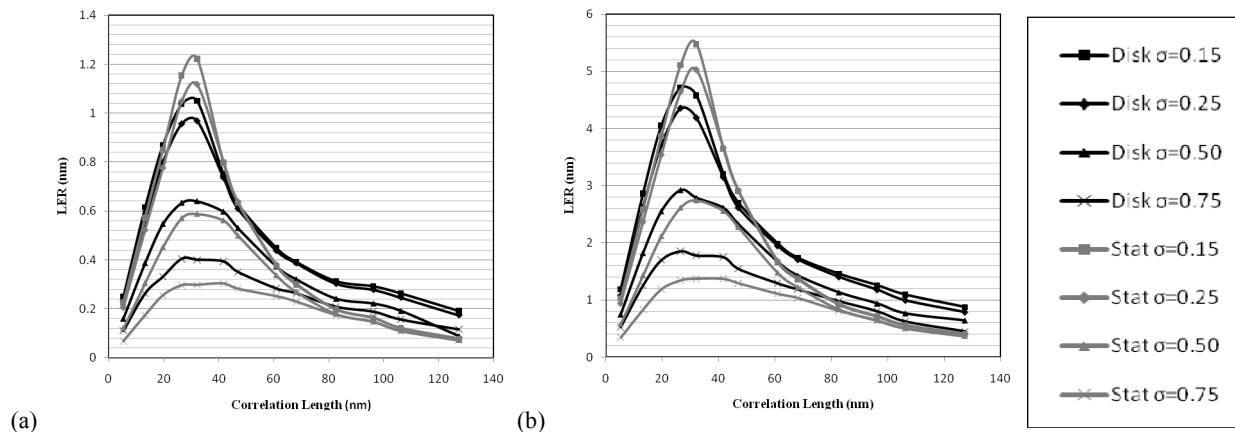


Fig. 38. Simulated LER data through focus for 50 nm lines and spaces, RSR 50 pm, disk of $\sigma = 0.15$ illumination, for a variety of correlation lengths.

The results are shown in Fig. 39 are at a defocus setting of -50 nm and give an excellent match. We repeated the entire data set for 40 nm lines and spaces and 22 nm lines and spaces, the results of which are also shown in Fig. 39. We also repeated the entire data set on 50 nm and 22 nm lines and spaces for a different RSR value of 230 pm, shown as well in Fig. 39. For 22 nm lines and spaces with an RSR of 230 pm [Fig. 39 (d)], the defocus setting was changed slightly to -30 nm, due to the reduced depth of focus. In all cases, there was good agreement between the full and simplified LER methods. At large correlation lengths, however, the case of 22 nm lines and spaces for highly coherent disk illuminations of $\sigma = 0.15$ and 0.25, the simplified model significantly underestimates the simulated LER. We believe that in this regime, the assumption that the speckle at the line-edge can be obtained by scaling the clear-field speckle by the intensity at the line-edge is no longer strictly true. For correlation lengths less than 60 nm, it is apparent that the scaled clear-field speckle formulation is a good rule-of-thumb, nonetheless. The simplified model seems to consistently underestimate the simulated LER by only a small amount for all illuminations, approximately 0.1 nm at most.



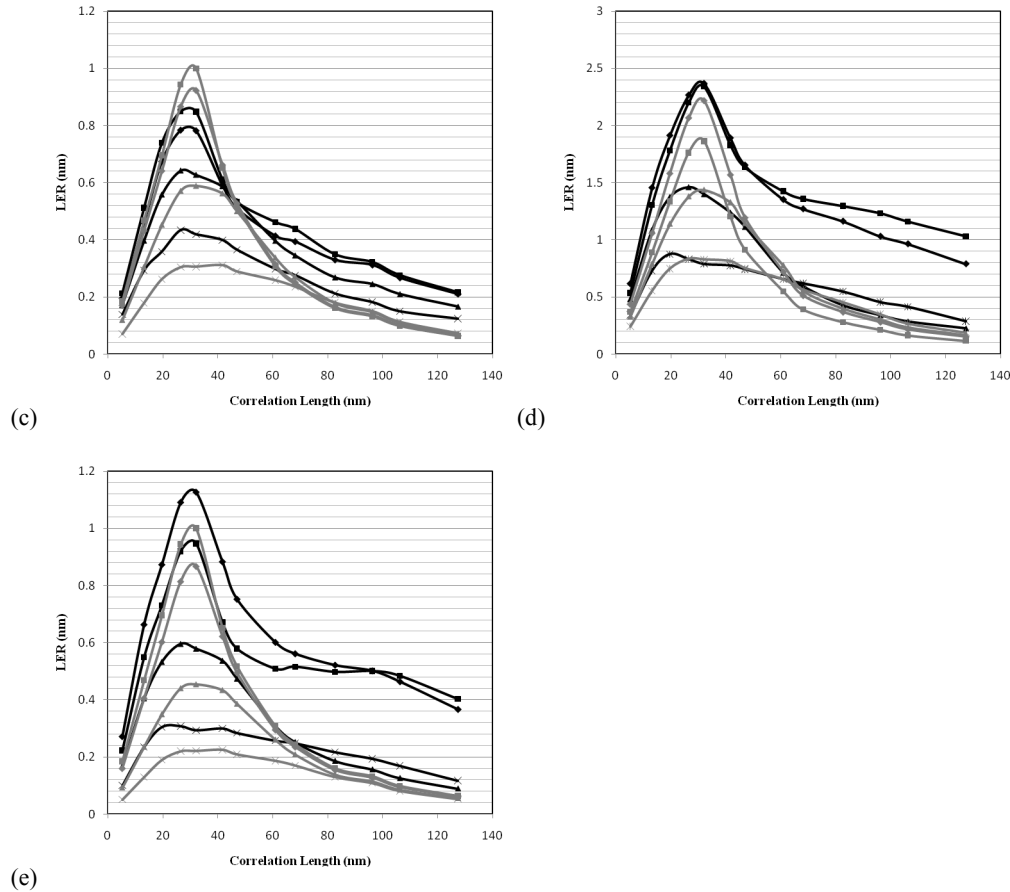


Fig. 39. Simplified LER (“Stat” indicated in gray) for the calculation of LER based on Eq. 2 in comparison with Simulated LER (“Disk” indicated in black) for RSR 50 pm, a variety of illuminations, a variety of correlation lengths, for (a) 50 nm hld (horizontal line dense, or lines and spaces) for RSR 50 pm, (b) 50 nm hld for RSR 230 pm, (c) 40 nm hld for RSR 50 pm, (d) 22 nm hld for RSR 230 pm, and (e) 22 nm hld for RSR 50 pm. All were at a defocus setting of -50 nm, except for (d) which was at -30 nm defocus.

4.2 Verification at higher NA

In order to verify that the peak location in correlation length is tied to the NA of the optic, we also tested the simplified model against higher NA, keeping all other parameters the same. So, now shifting from $NA = 0.32$ to $NA = 0.5$, we see a corresponding shift of the peak location to a lower correlation length, again on par with the enhanced resolution of the optical system. We note that the actual peak location is slightly higher than the arbitrary $0.61\lambda/NA$ resolution according to Rayleigh, and this is due to maximal capture of the scattering halo by the optic when at a value of $0.71\lambda/NA$ (based on a sinc function instead of a Gaussian). Again, this was for an RSR of 50pm, through correlation length, this time for a defocus value of -30nm. Reasons for the apparent worse performance of the larger features at 50nm CD versus 22nm CD are explained in chapter 6 when the data is revisited (see Figure 40).

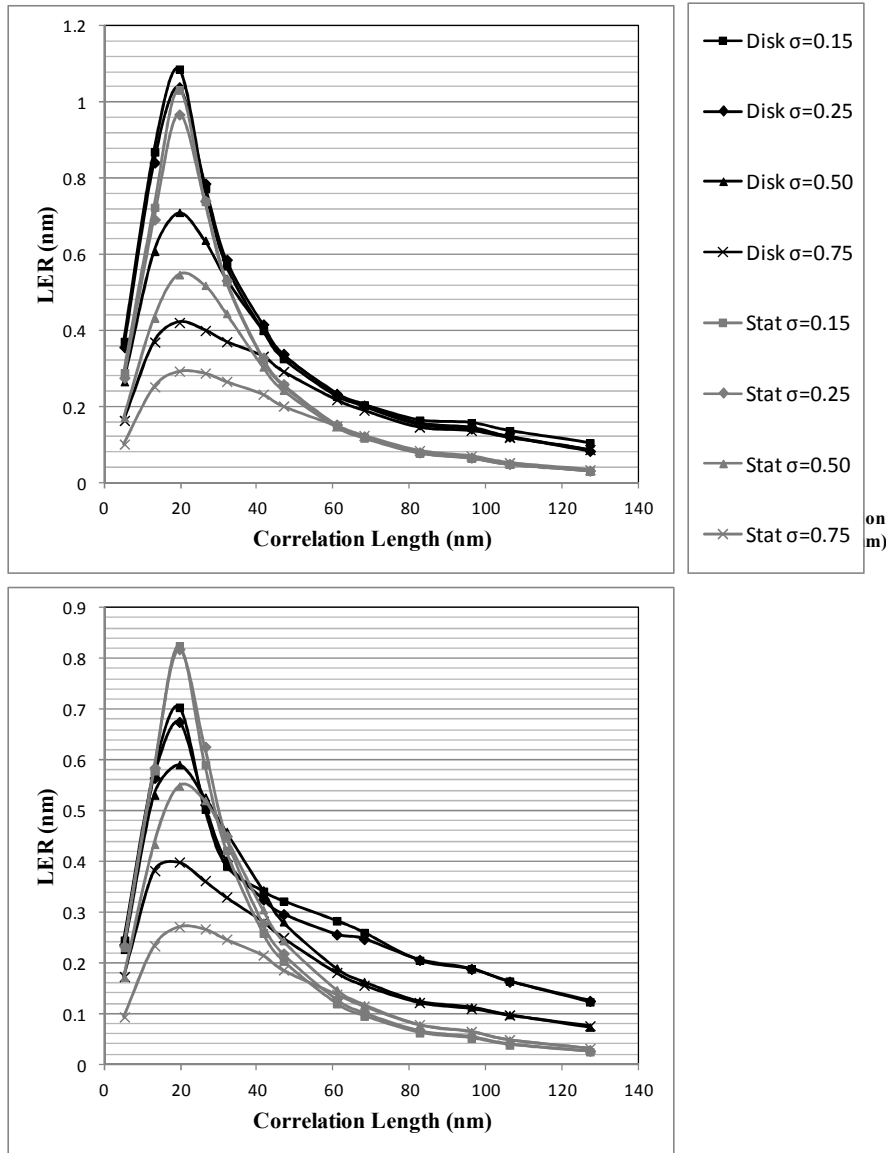


Fig. 40. (Top) 50nm lines and spaces on 50pm RSR for NA = 0.5 at -30nm defocus, and (bottom) 22nm lines and spaces.

4.3 Verification on isolated lines and spaces

The scaling of the speckle by the intensity at the line-edge has interesting implications for the mask roughness induced LER of isolated lines versus isolated spaces. In the case of an isolated space of a sufficiently small feature, the intensity in the middle of the space is unable to reach the maximum it would for a much larger feature. This, in turn, damps the intensity at the line-edge, and consequently the speckle at the line-edge calculated in equation 2, and improves the mask roughness induced LER as seen in equation 3. Isolated lines do not benefit from any similar situation, as there is no damping of the intensity in the clear-field surrounding the isolated line feature.

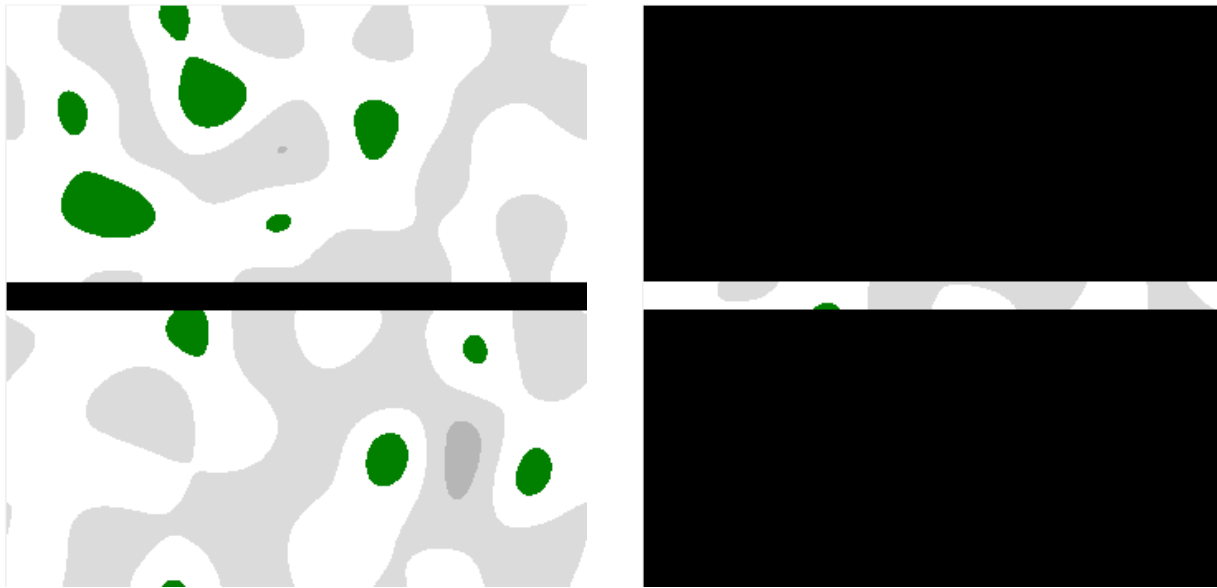


Fig. 41. (Left) Isolated line on rough surface, and (right) isolated space on a rough surface.

Figure 42 illustrates numerically the difference in maximum intensity reached for both an isolated line and an isolated space and for both 22-nm and 50-nm features. This was for an aberration-free imaging system of $NA = 0.32$ at a defocus of -50 nm and disk illumination settings of $\sigma = 0.15, 0.25, 0.50,$ and 0.75 . For the 50-nm features, the difference in maximum intensity between the isolated line and the isolated space is minimal. In contrast, for the 22-nm features the difference is significant, and it is to be expected that the 22-nm isolated line features would have significantly worse LER than that of the isolated space.

	$\sigma = 0.15$	$\sigma = 0.25$	$\sigma = 0.50$	$\sigma = 0.75$
50-nm Isolated Line	1.133	1.13	1.106	1.046
50-nm Isolated Space	1.307	1.285	1.189	1.043
22-nm Isolated Line	1.207	1.188	1.11	1.014
22-nm Isolated Space	0.724	0.715	0.672	0.597

Fig. 42. Maximum Intensity for isolated line versus isolated space for disk illumination setting of $\sigma = 0.15, 0.25, 0.50,$ and 0.75 , at a defocus of -50 nm, for both 50-nm and 22-nm features. For an $NA = 0.32$ aberration-free imaging system.

To verify this prediction, full 2D aerial image modeling with conducted for an optical system with $NA = 0.32$, four different disk illumination conditions ($\sigma = 0.15, 0.25, 0.50, 0.75$), an RSR setting of 50 pm, and for both a 22-nm and a 50-nm isolated line and isolated space through focus, and for a variety of correlation lengths (5, 13, 20, 26, 32, 42, 47, 61, 68, 83, 96, 106, 127 nm). Again, for each illumination setting, the data were well-behaved through focus, exhibiting

no crossover from one correlation length to another. Therefore the data at one defocus setting is consistent with how the LER behaves at other defocus settings as well. This was compared against the simplified model described above in Figure 43 at a defocus setting of -50 nm. The simplified model matches well to the fully simulated LER, to within 0.2 nm LER accuracy.

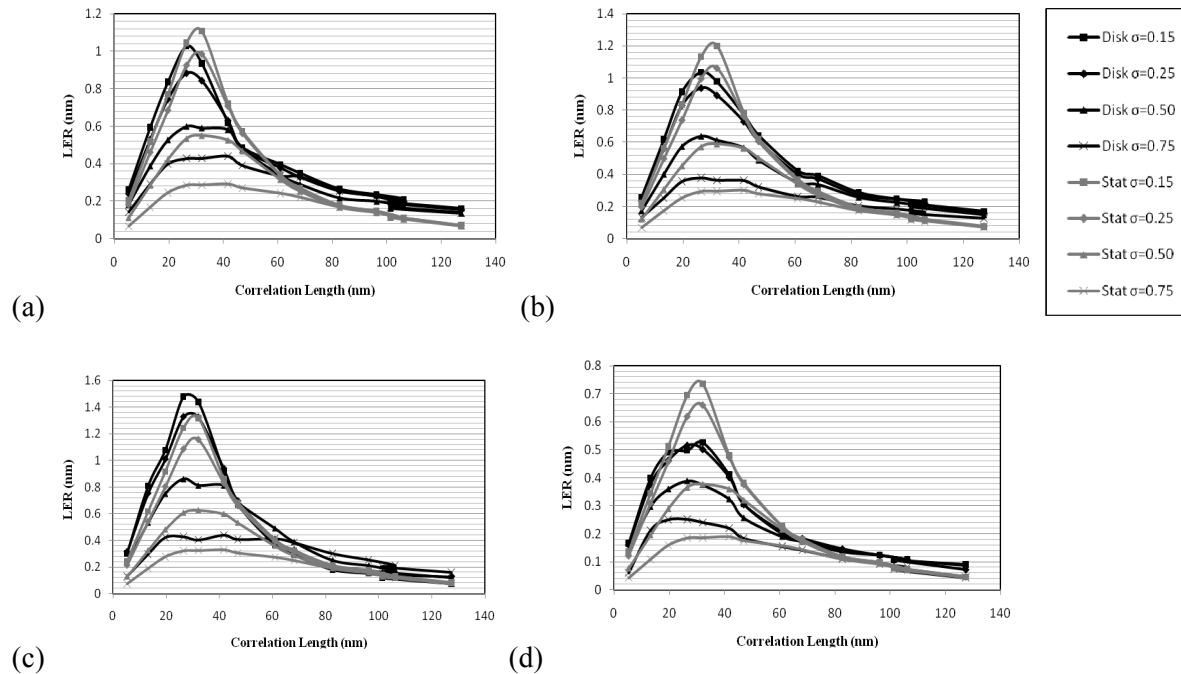


Fig. 43. Numerical results (“Stat” indicated in gray) for the calculation of LER based on Eq. 3 in comparison with the LER calculated from the full 2D aerial image simulation (“Disk” indicated in black). This was for an imaging system with $NA=0.32$, ideal pupil map, disk illumination settings $\sigma = 0.15, 0.25, 0.50, 0.75$, RSR of 50 pm, through correlation length, for (a) 50 nm isolated line, (b) 50 nm isolated space, (c) 22 nm isolated line, and (d) 22 nm isolated space, all at a defocus setting of -50 nm.

In plotting the fully simulated LER for the isolated line directly against the isolated space in Figure 44, it is as expected that the difference in mask roughness induced LER between them for a particular illumination setting is insignificant at the 50-nm feature level. At the 22-nm feature level, however, the difference is considerable, showing the strong effect the intensity-scaling of the speckle has on the LER. It is interesting to note that from the perspective of a feature size close to the diffraction limit (the 22-nm level in this case), the isolated space should have induced a random walk intensity variation in the direction normal to the length of the line, as reported previously in the 2D case of contacts [5]. This should have increased the rms deviation of the speckle to some degree, ultimately benefiting the printing of isolated lines as opposed to spaces, from the perspective of LER. As seen in Figure 43 however, the results clearly indicate that this effect is minimal in comparison to the effect of intensity-scaling the speckle.

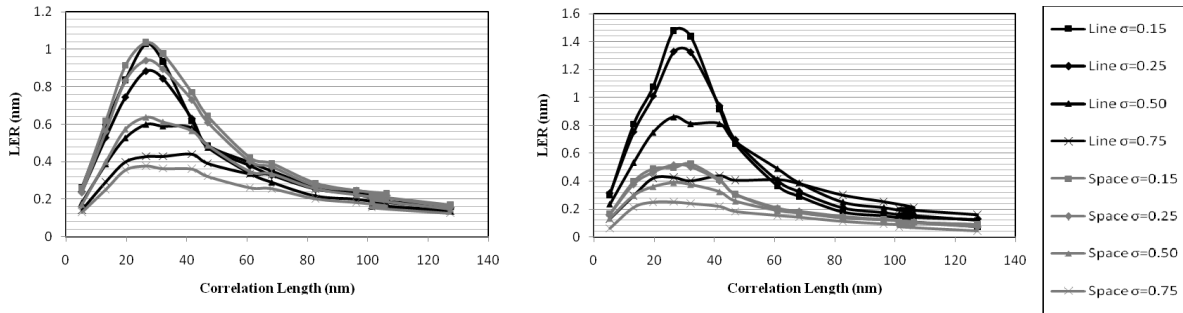


Fig. 44. LER as a function of correlation length data replotted for isolated line versus isolated space for disk illumination setting of $\sigma = 0.15, 0.25, 0.50,$ and 0.75 , at a defocus of -50 nm, for 50 -nm features (*left*) and 22 -nm features (*right*). For an $NA = 0.32$ aberration-free imaging system, and a rough mask with RSR 50 pm, and a variety of correlation lengths.

4.4 Verification at long correlation lengths

We also later explored the behavior at long correlation lengths to see if the mask roughness induced LER prediction collapsed to a single value for all coherence values. We expect that through correlation length the coherence values should preserve order: more incoherence means a larger diffracted order signal is captured by the optic, so greater averaging of the roughness statistics can help mitigate the speckle. However, in the case of long correlation lengths, this should matter less and less as the mask gets globally more smooth (more discussion to follow in Chapter 6, where the geometric model is explored). Replotting previous fully simulated LER values, and now expanding the correlation length range to include a data point at 250 nm, we conduct our investigation on both 50 nm and 22 nm lines and spaces for an RSR of 50 pm, $NA = 0.32$, at a defocus of -50 nm. We find that for the larger CD (50 nm), the mask roughness induced LER has indeed nearly collapsed to approximately the same value, but for the smaller CD (22 nm), the discrepancy between various coherence values remain to within 0.1 nm LER. We note that for the case of the 22 nm CD and disk $\sigma = 0.50$ illumination type, we could not compute the LER due to corrupted data at this defocus value.

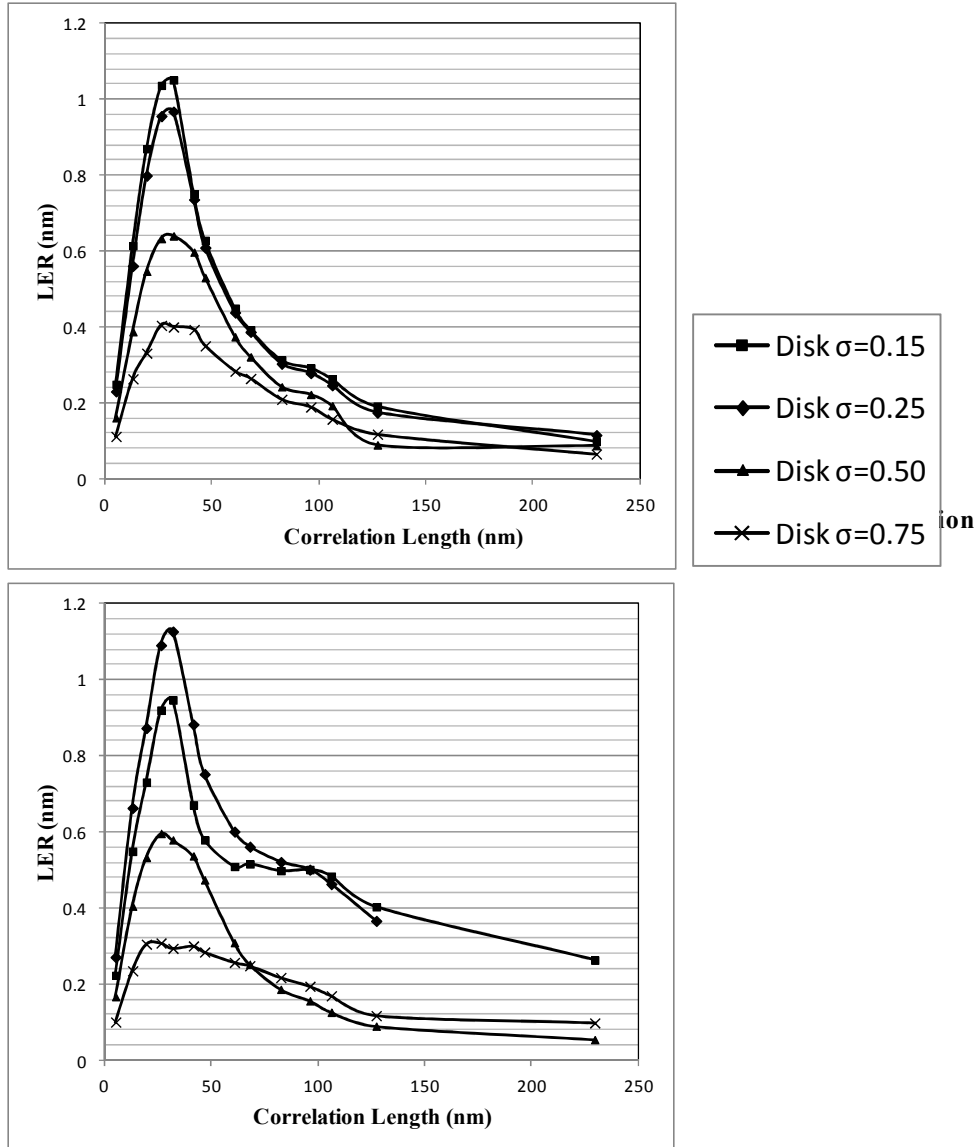


Fig. 45. (Top) 50nm lines and spaces for 50pm RSR at a defocus of -50nm, and (bottom) 22nm lines and spaces.

4.5 Verification self-affine surfaces

The effect of roughness exponent on the comparison was also investigated. All of the previous rough mask surfaces were generated by a random Gaussian number generator subjected to a top-hat filter on the PSD, resulting in band-limited, non-fractal roughness. This is effectively equivalent to a roughness exponent of infinity, where the roughness exponent is given by $(m-1)/2$ [59], where m is the slope after the “knee” in a log-log plot of the PSD, where the “knee” itself is located at the correlation length. Technically, a roughness exponent between 0 and 1 represents the two extremes for self-affine surfaces. Practically, a roughness exponent between 0.2 and 0.8

are good representatives of the two extremes. Therefore, in verifying the simplified method for other roughness exponents, we started with subjecting a random Gaussian number distribution to a filter on the PSD whose knee position was determined for a correlation length of 32 nm and separately for roughness exponents of both 0.2 and 0.8. The PSD was then normalized so that the total integrated energy yielded an RSR of 50 pm. Proceeding in a manner similar to that outlined above, we carried out both the full 2D aerial image LER analysis and the simplified method for 50 nm lines and spaces, for an NA = 0.32, an ideal pupil map, for a variety of partial coherence settings ($\sigma = 0.15, 0.25, 0.50, \text{ and } 0.75$), and through focus from $-0.1\mu\text{m}$ to $+0.1\mu\text{m}$.

The results are seen in Fig. 46, and show that the simplified method remains a valid one to predictions as accurate as 0.1 nm LER, for roughness exponents of 0.2 (Fig. 46(a)) and 0.8 (Fig. 46(b)), the practical extremes for self-affine rough surfaces. It is expected that a change in roughness exponent should have little effect on the validity of the simplified method since most of the integrated roughness is contained within the lower spatial frequencies of the PSD before the occurrence of the knee. The amount of integrated roughness contained in the region whose spatial frequencies are dampened by the roughness exponent remains comparatively insignificant, even for a roughness exponent of 0.2. We also note that the previous results presented in Fig. 45 represent a worst-case scenario for LER specifications, as the top-hat filtered PSD applied to this data means that all of the integrated rms roughness was contained in the lower-spatial frequencies which count towards LER[1].

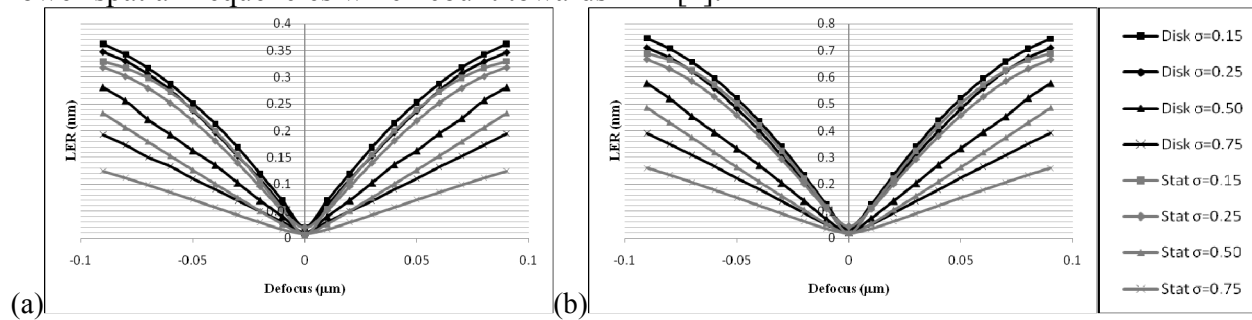


Fig. 46. Simplified LER (“Stat” indicated in gray) for the calculation of LER based on Eq. 2 in comparison with Simulated LER (“Disk” indicated in black) for RSR 50 pm, a variety of illuminations, for a correlation length of 32 nm, 50 nm hld, an RSR of 50 pm, through focus from $-0.1\mu\text{m}$ to $+0.1\mu\text{m}$, for (a) a roughness exponent of 0.2 and (b) a roughness exponent of 0.8.

4.6 Conclusions

A practical means of implementing the newly proposed simplified model of mask induced roughness induced LER has been described in detail. The method has been confirmed to work for the two extrema in pattern imaging: 50% duty cycle line dense structures as well as completely isolated lines and spaces, at both the 50-nm and 22-nm feature level. Specifically, for the 50nm dense lines and space features for an RSR of 50pm and correlation length of 32nm with NA = 0.32, the LER level is at $\sim 1.1\text{nm}$, and by scaling to 230pm RSR, the LER increases to $\sim 4.5\text{nm}$. In addition, the implications of intensity-scaled speckle outlined by the method mean that isolated lines face a particular challenge in mask roughness induced LER maintenance as opposed to isolated spaces at the 22-nm feature level. This is not a concern at the 50-nm feature level.

The simplified model has also been verified at higher NA, longer correlation lengths, and differing roughness exponents, as typical for self-affine surfaces.

Chapter 5

Simplified Model Verification Part II

In Chapters 3 and 4, a new simplified model has been proposed [70] for faster modeling and prediction of mask roughness induced LER based on parameters of objective NA, mask roughness, defocus, and illumination conditions. We extend that work and verify the validity of this simplified model across a much wider range of parameters. We first discuss the implementation, and verify from conventional disk-type illumination to off-axis illumination configurations down to the 16-nm half pitch, and all through focus. We also examine the performance of the simplified model for an alternating phase-shifting mask (Alt-PSM), and compare mask roughness induced LER for the Alt-PSM versus traditional lines and spaces.

5.1 Off-Axis Illuminations

It is important to verify that the simplified model works not only for disk-type illumination, but also for off-axis illumination. Similar to the data above, we model with illumination wavelength of 13.5 nm an aberration-free objective at $NA = 0.32$, for both an RSR setting of 100 pm and correlation length of 32nm, for both 22-nm and 16-nm lines and spaces through focus. The illumination types we considered were: disk ($\sigma = 0.10$ and 0.50), dipole ($\sigma = 0.10$ and 0.50), crosspole ($\sigma = 0.10$ and 0.50), and annular ($\sigma = 0.10$).

5.1.1 Thresholding

In evaluating the simplified model, it was found that the off-axis illumination types were particularly sensitive to the threshold the through focus LER and ILS were calculated at, and care should be taken that these mechanisms are consistent with one another, despite the possible use of different software packages with different thresholding algorithms. For instance, one can choose the threshold to be absolute based at zero defocus (the method Prolith [77] uses), or relative (the method used by SuMMIT [79]).

5.1.2 New results though focus

A comparison of fully simulated mask roughness induced LER versus the simplified model's prediction are shown in Fig.47. The method of thresholding chosen was a relative threshold. While the 100pm RSR value is not the ideal of 50pm, it is a more realistic specification for current mask technologies. The correlation length value of 32nm, as previously mentioned, lies directly on the peak LER value through correlation length, and so represents a worse-case

scenario of mask roughness induced LER for this optic. We note that the random variations in the simplified models predicted LER value is noisy for illumination types disk and crosspole of $\sigma = 0.10$ due to the speckle at such a high coherence setting, which leads to negative exponential statistics, and means fluctuations about the mean are rather pronounced [70]. The shortened focal range analyzed for the fully simulated LER of disk and annular of $\sigma = 0.10$ was caused by corrupted data further out of focus. As expected, higher coherence settings yield consistently higher mask roughness induced LER values through focus due to increased speckle contrast. In all cases, the simplified models prediction, through focus, for the mask roughness induced LER performs remarkably well— to within 0.2nm LER accuracy at the outer extremes of focus. The accuracy improves as the incoherence is increased, again due to the increased noise of limiting negative exponential statistics with very coherent source types. This noise could be improved by increasing the ensemble either spatially in extent of the mask, or the number of independent realizations.

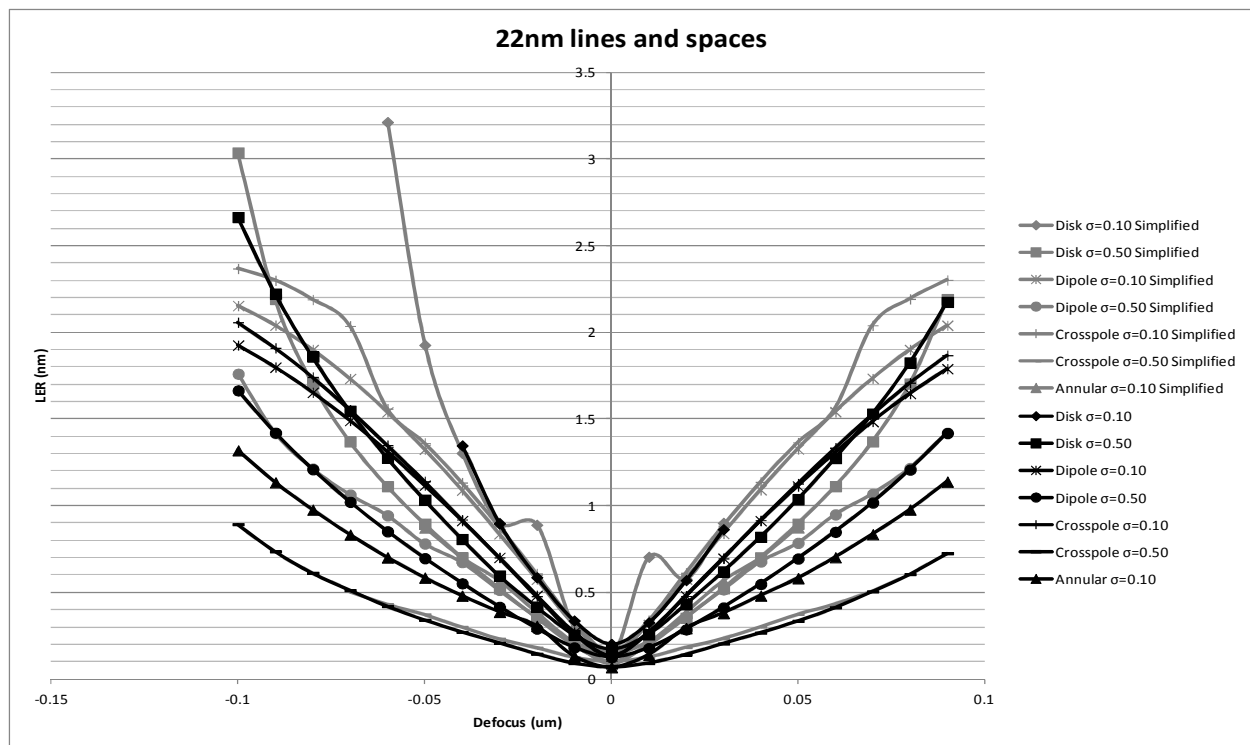


Fig. 47. Numerical results (“Simplified” indicated in gray) for the calculation of LER based on Eq. 3 in comparison with the LER calculated from the full 2D aerial image simulation (indicated in black). This was for an imaging system with NA=0.32, ideal pupil map, various illumination settings $\sigma = 0.10$ and 0.50, RSR of 100 pm, a correlation length of 32nm, for 22nm half-pitch, all through focus.

We repeated our exploration of the validity of the simplified model pushing the limit to the 16nm half-pitch node. Again, on a mask of RSR 100pm and correlation length of 32nm, illumination wavelength of 13.5 nm an aberration-free objective at NA = 0.32, we looked at dipole ($\sigma = 0.10$ and 0.50), crosspole ($\sigma = 0.10$ and 0.50), and annular ($\sigma = 0.10$ and 0.50), where the placing of the poles was optimized given the pitch and NA (crosspole is in the 90° orientation). Again, the shortened range of focus over which the LER was analyzed for in certain line-trends was due to corrupted data. Results in Fig. 48 show that once more, the simplified model holds up under rather large focal ranges, to within an accuracy of ~ 0.2 nm LER. Overall, the predicted mask

roughness induced LER levels remain much higher for the 22nm half-pitch versus the 16nm half-pitch. Although the ILS is most certainly poorer for the 16nm half-pitch, this seeming improvement in LER is accounted for by a combination of both slightly lower intensity threshold value and speckle, both of which have a strong effect on the ultimate mask roughness induced LER, as explained in Section 2.

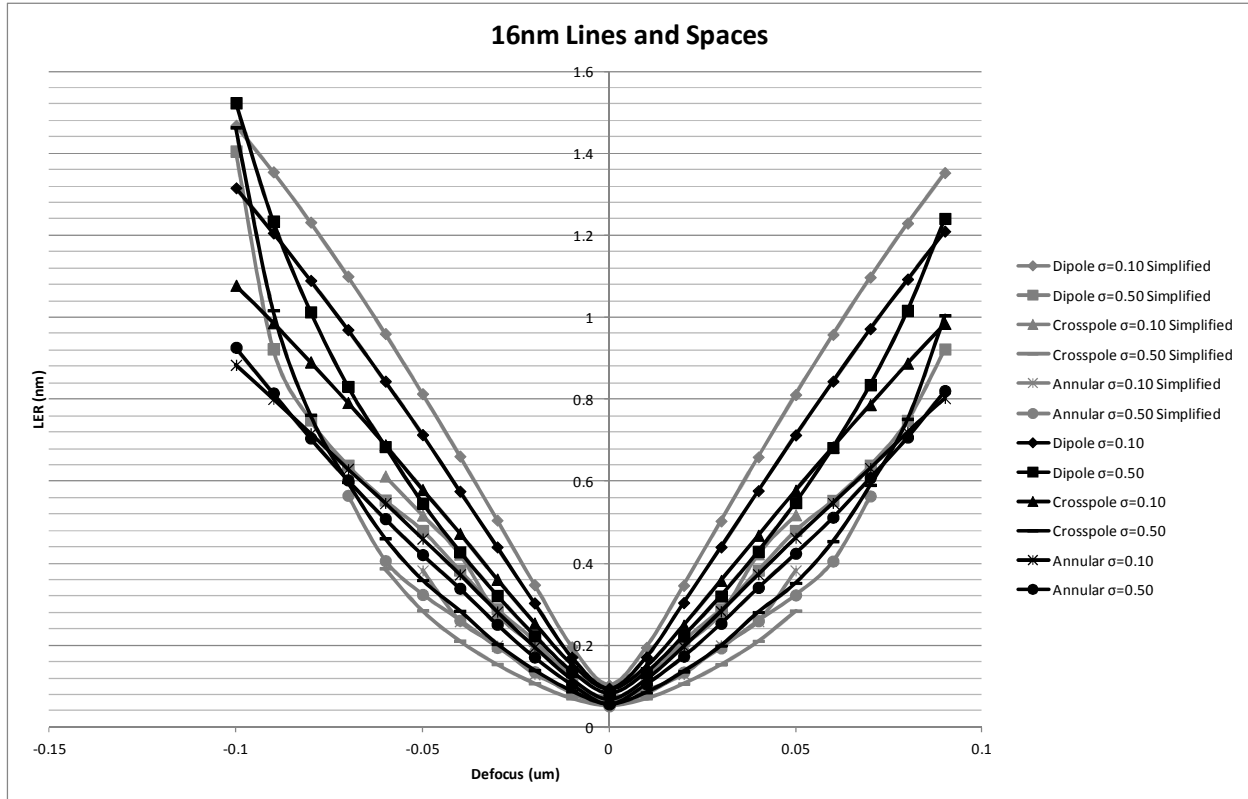


Fig. 48. Numerical results (“Simplified” indicated in gray) for the calculation of LER based on Eq. 3 in comparison with the LER calculated from the full 2D aerial image simulation (indicated in black). This was for an imaging system with $NA=0.32$, ideal pupil map, various illumination settings $\sigma = 0.10$ and 0.50 , RSR of 100 pm, a correlation length of 32nm, for 16nm half-pitch, all through focus.

5.2 Alt-PSM

We were also interested in verifying the performance of the simplified model on an alternating phase-shifting mask (Alt-PSM).

5.2.1 Simulated vs. Simplified at 22-nm

To evaluate the phase shifting mask, we constructed our mask object with the same mask roughness ensemble used in previous chapters for an RSR value of 50pm, through correlation length. The phase shift occurred with periodicity of 88nm (double the frequency we desire to reach), and on an optical system with $NA = 0.32$. The size of the features versus resolution of the optic is important: if the feature size were too large, then the alternating phase shift would not produce a sinusoid in the image, but rather strong narrow lines about the size of the resolution of the optic where each phase edge occurs. The clearfield speckle statistics used were the same as those used previously on the same optical system, RSR, and correlation length distribution.

Again, the data to be compared for the simulated versus simplified model was generated at a defocus setting of -50nm, and the image sized to 22-nm at best focus, with the ILS and intensity thresholding made to match the analysis method of the LER analysis program SuMMIT. Disk illumination was modeled for $\sigma = 0.15, 0.25, 0.50,$ and $0.75,$ with no aberrations.

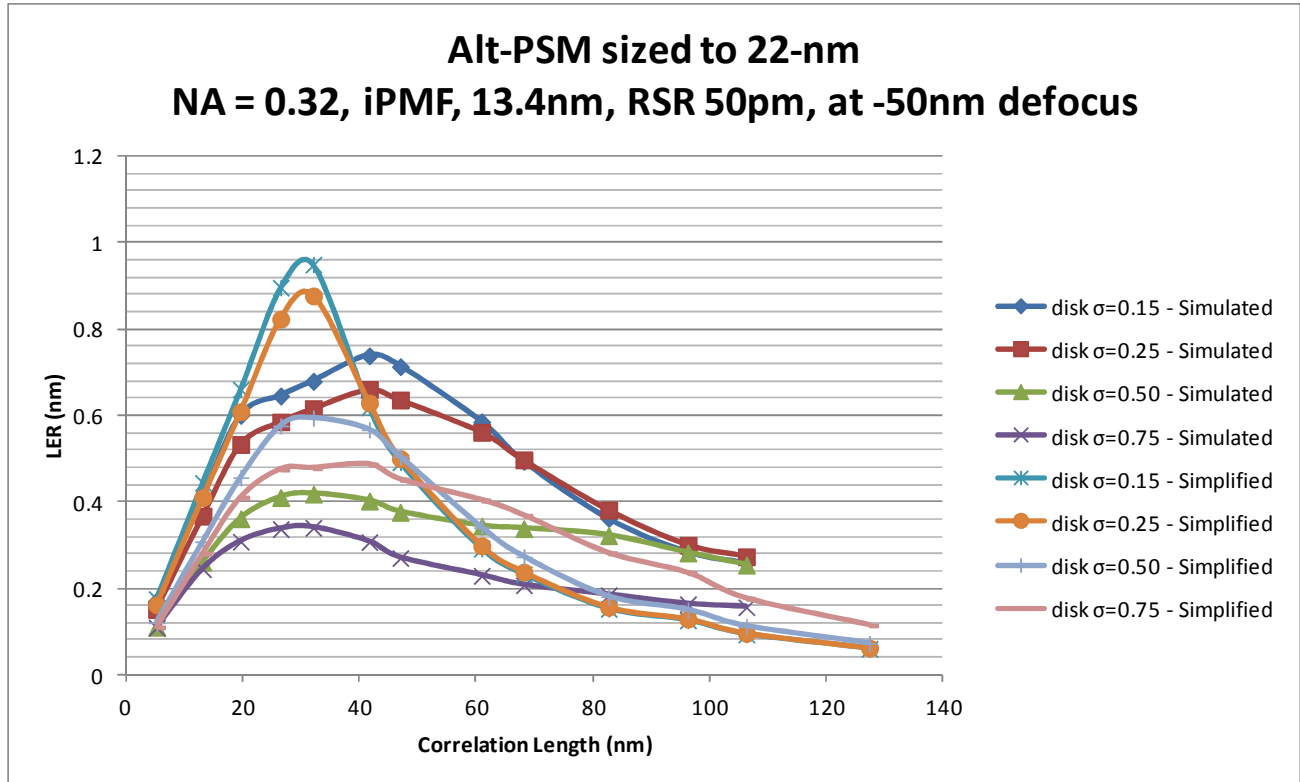


Fig. 49. Numerical results (“Simplified”) for the calculation of LER based on Eq. 3 in comparison with the LER calculated from the full 2D aerial image simulation (“Simulated”). This was for an imaging system with $NA=0.32$, ideal pupil map, disk illumination settings $\sigma = 0.15, 0.25, 0.50,$ and $0.75,$ RSR of 50 pm, a correlation length of 6-127nm, for 22nm half-pitch, at a defocus of -50nm.

Results show that the simplified model again provides a match to within 0.2nm LER accuracy for predicting the mask roughness induced LER values. The fully simulated LER values have a broader peak in terms of correlation length than what the simplified model predicts. This could be due to changes in the speckle statistics due to non-linearity between clearfield versus line-edge speckle, or a difference in intensity thresholding for calculation of the LER: the ILS and intensity were calculated independently so that features were sized to 22-nm at best focus, whereas the fully simulated LER data was sized to 22-nm at best focus and analyzed in SuMMIT, one time, independent of correlation length.

5.2.2 Alt-PSM vs. Lines and Spaces at 22-nm

We wish to revisit previous data on the conventional 22-nm half-pitch lines and spaces, and compare that directly to the alt-psm data presented above. Plotted below, we see that conventional lines and spaces have a significantly higher LER peak at the correlation length of

the resolution of the optic: the alt-psm data shows a much broader, but lower peak in comparison. For more incoherent illumination of disk $\sigma = 0.75$, however, there is no significant difference between the two data sets. Since the ILS is constant through correlation length, as well as the intensity the image was thresholded at, we know that this slight mismatch in contour is due directly to the differences in speckle contrast between the clearfield and that at the line-edge, through correlation length.

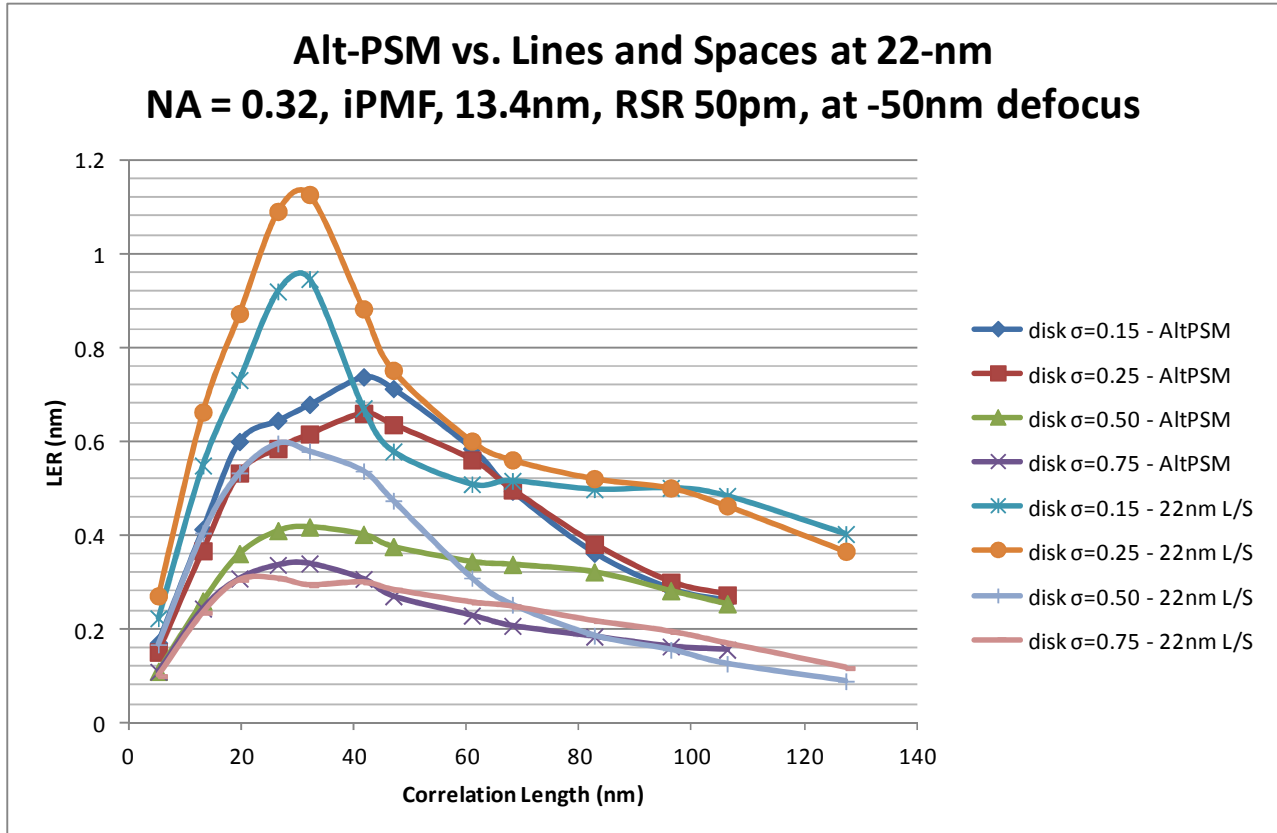


Fig. 50. Fully simulated LER results for the alt-psm versus traditional lines and spaces for 22-nm half-pitch, plotted for direct comparison. This was for an imaging system with $NA=0.32$, ideal pupil map, disk illumination settings $\sigma = 0.15, 0.25, 0.50, \text{ and } 0.75$, RSR of 50 pm, a correlation length of 6-127nm, for 22nm half-pitch, at a defocus of -50nm.

5.3 Conclusions

The simplified model has been verified for off-axis illuminations, through focus, down to the 16nm half-pitch. In particular, the off-axis illumination is very sensitive to the thresholding mechanism used for calculation of the ILS, Intensity, and LER, and should be internally consistent. This is true as well when evaluating the simplified model on alt-psm objects, which were verified for 22-nm.

Chapter 6

Geometric Model

As outlined in chapters 4 and 5, progress has been made in formulating a simplified solution for mask roughness induced LER. Even with already simplified models, however, we seek to find even faster solutions. In this chapter, we develop a geometric model for mask roughness induced LER which is even faster than the already described simplified model. Specifically, we investigate the LER behavior at long correlation lengths of surface roughness on the mask, and find that for correlation lengths greater than $3\lambda/\text{NA}$ in wafer dimensions and CDs greater than approximately $0.75\lambda/\text{NA}$, the simplified model, which remains based on physical optics, converges to a “geometric regime” which is based on ray optics and is independent of partial coherence. In this geometric regime, the LER is proportional to the mask slope error as it propagates through focus, and provides a faster alternative to calculating LER in contrast to either full 2D aerial image simulation modeling or the newly proposed physical optics model. Data is presented for both an $\text{NA} = 0.32$ and an $\text{NA} = 0.5$ imaging system for CDs of 22-nm and 50-nm horizontal-line-dense structures.

6.1 Geometric Regime

As the partial coherence increases to a nominally incoherent regime, we see from previous data in Chapters 3 and 4, that mask roughness induced LER collapses to nearly the same levels across all illumination types. Therefore, this seems to indicate that a geometric regime would be valid for the modeling of mask roughness induced LER, independent of coherence. We explore the possibility of using a geometric principle to further speed the modeling process.

6.1.1 Long correlation lengths trend

Considering all previous data and as noted previously, we see that the LER decreases, but much more gradually, as the correlation length of the roughness gets longer and longer. This can be seen across all data for an optical system with $\text{NA} = 0.32$, four different illumination conditions ($\sigma = 0.15, 0.25, 0.50, 0.75$), two RSR settings of 230 pm and 50 pm, for 22 nm and 50 nm lines and spaces, at a defocus of -50 nm, through a variety of correlation lengths (5, 13, 20, 26, 32, 42, 47, 61, 68, 83, 96, 106, 127 nm), and a roughness exponent of infinity. Here, all the light is captured by the pupil; this adverse effect, however, is mitigated due to a decreasing rate of change of the induced phase roughness, and, for correlation lengths greater than $3\lambda/\text{NA}$ in wafer dimensions, and CDs greater than approximately $0.75\lambda/\text{NA}$, becomes roughly independent of

partial coherence, to within 0.1nm LER with each other. In this limit, a geometric model based on ray optics should be valid since interference effects no longer play an important role.

6.1.2 Mask Slope Error

In this “geometric regime”, we assume the LER to be proportional to the mask slope error as it propagates through focus (see Fig. 51).

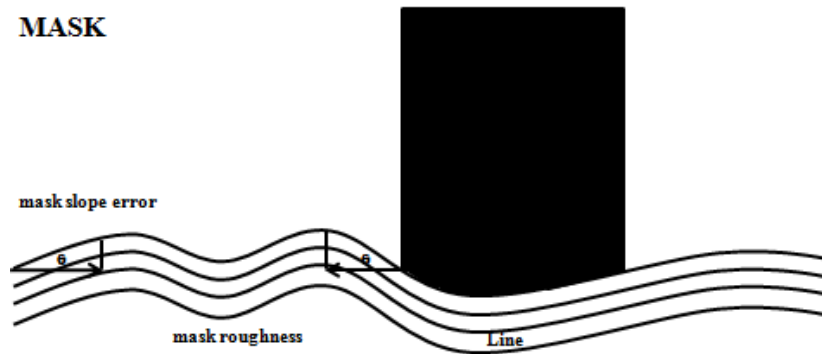


Fig. 51. In the “geometric regime”, the LER is proportional to the mask slope error as it propagates through focus.

Physically, the slope at the base of the feature acts as a local tilt. At zero defocus, the position of the base edge of the feature is perfectly reproduced in the image by the light rays. As soon as defocus is introduced, however, the local tilt which causes a slight change in the angle of the light ray, results in a real image placement error with finite defocus. This problem is further amplified by the reflective architecture of the multilayer mirrors, which amplifies the angle by a factor of 2 (see Fig.49). Thus, for a defocus amount δz , a tilt of angle θ (in radians), the amount of image placement error is thus $IPE=2*\theta*\delta z$, by small angles approximation [81].

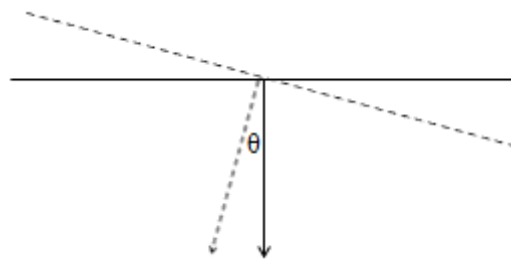


Fig. 52. Image placement error due to slight change in the angle of the light ray, at finite amounts of defocus.

6.2 Geometric Model

In the sections below, we seek to implement the mask slope error concept into our conception of a geometrical model, and verify it provides a good prediction of the LER at these long correlation lengths [82].

6.2.1 Construction

We explore the validity of the geometric model by directly comparing it to LER values extracted from full 2D aerial image simulations. In the comparison, we consider an aberration-free optical system with $NA = 0.32$. For the mask we consider RSR values of 50 and 230 pm and correlation lengths ranging from 5 to 127nm, and roughness exponent of infinity. To build up a significant statistical ensemble, 10 random realizations of the mask for each RSR / correlation length pair were considered. Assuming an illumination wavelength of 13.5 nm, each topographic height map surface was converted to a phase perturbation. The mask was modeled with 1024×1024 pixels at 1 nm / pixel assuming 1:1 imaging to the wafer plane. Following the modeling convention introduced in Chapter 3, we model the geometric prediction for both 22 nm and 50 nm line-space patterns. Simulations were carried out through focus for 4 different disk illuminations: coherence factors $\sigma = 0.15, 0.25, 0.50,$ and 0.75 .

In considering the geometric model, we assume that the LER is proportional to the mask slope error as it propagates through focus. We therefore first constructed the point-spread-function of an aberration-free optical system the same as that already investigated above [71], with an objective $NA = 0.32$ and assuming an illumination wavelength of 13.5 nm. We then convolved this with the topographical height map of the clear-field rough mask to get at how the mask slope error as seen by the wafer at the image plane (see Fig. 53). This height map is dependent only on the mask roughness properties, and was repeated on the same statistical ensemble of rough masks used to produce the data represented earlier; that is, masks for both an RSR of 50 pm and 230 pm, and a variety of correlation lengths (5, 13, 20, 26, 32, 42, 47, 61, 68, 83, 96, 106, 127 nm), a roughness exponent of infinity, with 10 random realizations of the mask for each RSR / correlation length pair. After the convolution performed on each mask, we then took the slope and propagated through focus to yield the geometric prediction which is also plotted in Fig. 54.

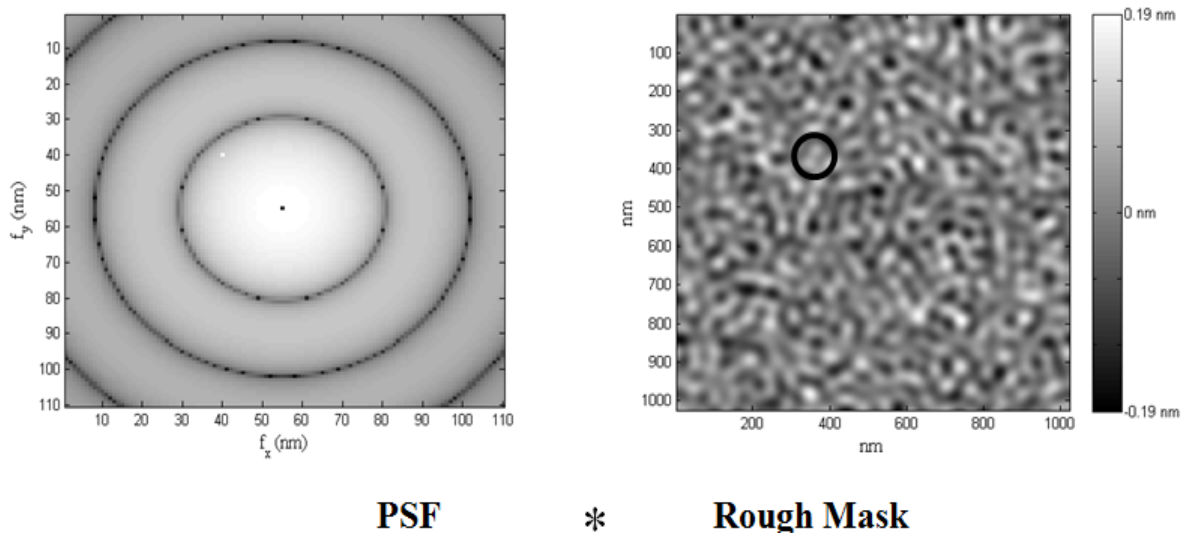


Fig. 53. To generate the “geometric” model, we constructed the point-spread-function of our imaging system (shown in log-scale on the left) and convolved it with the topographical height map of the clear-field rough mask to get how the mask is seen from the wafer plane (shown on the right, along with a

circle representing the first null of the Airy pattern in the PSF, radius of 26nm). We then took the slope across the mask to get the mask slope error, and propagated through focus appropriately.

6.2.2 Verification

It is evident from the results plotted in Figure 54 that the geometric model provides a good prediction of the LER for longer correlation lengths.

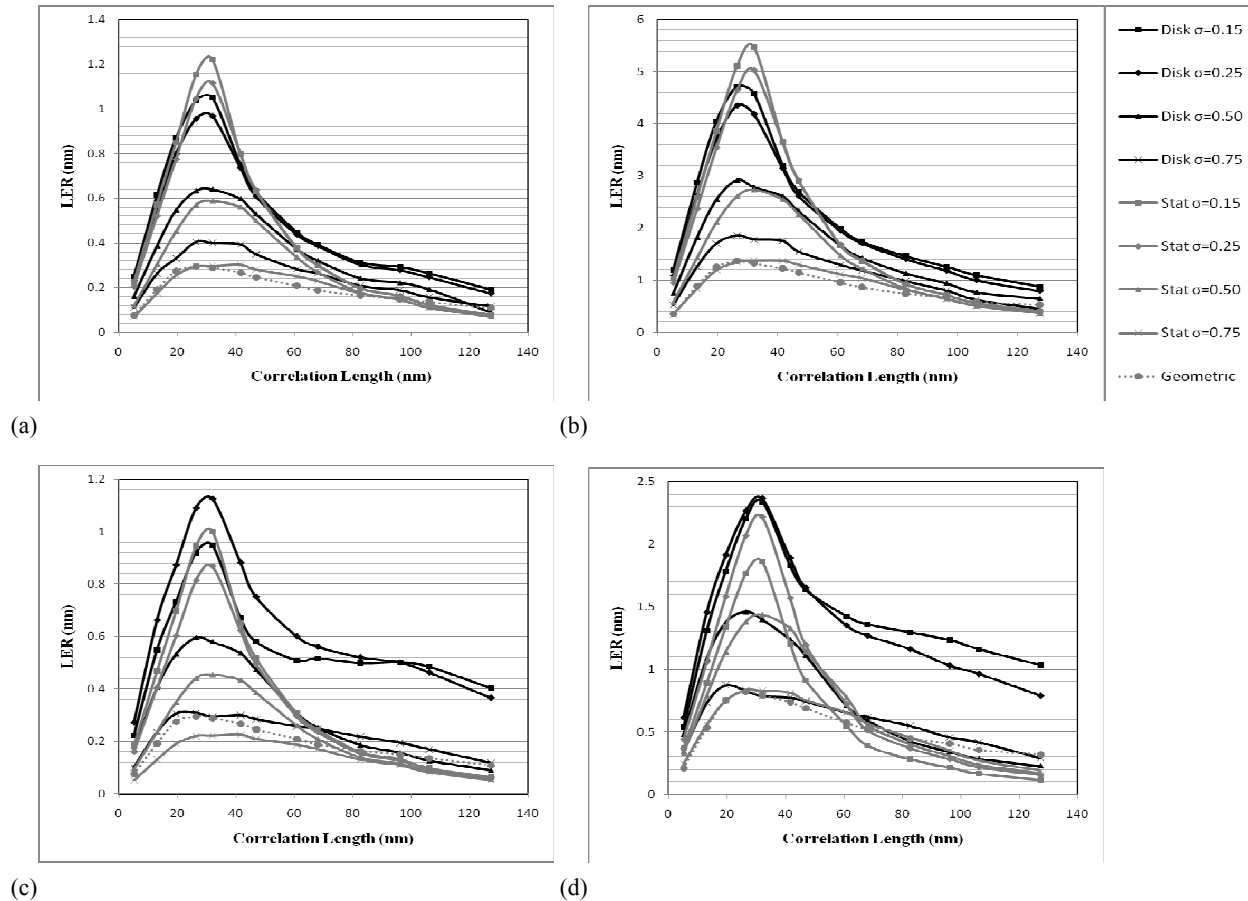


Fig. 54. Simplified LER (“Stat” indicated in gray) for the calculation of LER based on Eq. 2 in comparison with Simulated LER (“Disk” indicated in black) for RSR 50 pm, a variety of illuminations, a variety of correlation lengths, for (a) 50 nm hld (horizontal line dense, or, lines and spaces) for RSR 50 pm, (b) 50 nm hld for RSR 230 pm, (c) 22 nm hld for RSR 50 pm, (d) 22 nm hld for RSR 230 pm. All were at a defocus setting of -50 nm, except for (d) which was at -30 nm defocus.

We note that even in the case where the CD is less than $0.75\lambda/NA$, the geometric model matches to within 0.1nm LER with those illumination conditions which are less coherent ($\sigma = 0.50$, and 0.75 in Fig. 54).

To further test this model, we also consider an NA of 0.5. We repeated all the data for all three methods (fully simulated LER, LER from the simplified model, and LER for the geometric model) for masks of an RSR 50 pm with the same set of correlation lengths, and roughness exponent of infinity for the same illumination conditions ($\sigma = 0.15$, 0.25 , 0.50 , and 0.75), for both 22 nm and 50 nm lines and spaces. This data is seen in Fig. 55 (a) for a defocus of -50 nm

for 50 nm lines and spaces, and (b) for a defocus of -30 nm on 22 nm lines and spaces. Again, the geometric model provides a good prediction to within 0.1 nm of the LER for roughness correlation lengths greater than $3\lambda/NA$ in wafer dimensions. In this case since both CDs considered (22 nm and 50 nm) are now greater than approximately $0.75\lambda/NA$, all illumination conditions converge well to the geometric model for both CDs.

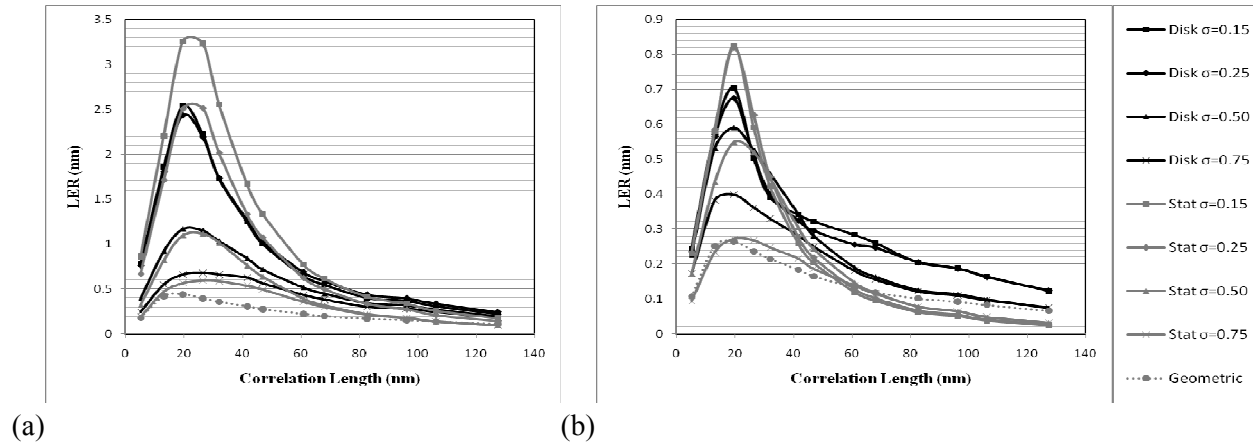


Fig. 55. Simulated LER vs. Simplified LER for an $NA = 0.5$ system, RSR 50 pm, a variety of illuminations, through correlation length, (a) at a defocus of -50 nm for 50 nm lines and spaces, and (b) at a defocus of -30 nm for 22 nm lines and spaces.

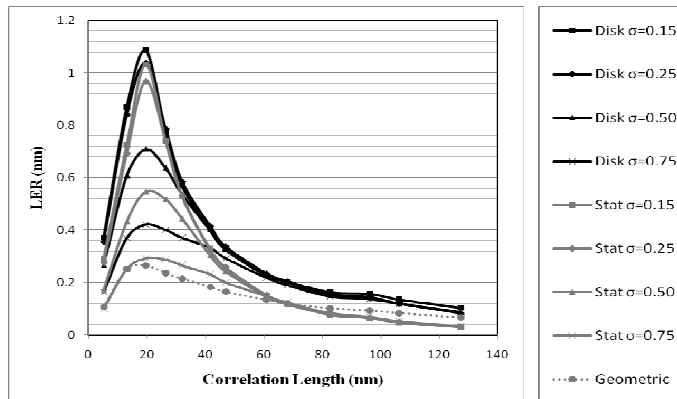


Fig. 56. Simulated LER vs. Simplified LER for an $NA = 0.5$ system, RSR 50 pm, a variety of illuminations, through correlation length, at a defocus of -30 nm for 50 nm lines and spaces.

6.3 Conclusions

We have shown that for roughness on the mask with correlation lengths greater than $3\lambda/NA$ in wafer dimensions and CDs greater than approximately $0.75\lambda/NA$, the physical optics-based simplified model converges to a geometric, ray optics regime which is independent of partial coherence. In comparison to either the fully simulated LER or even the LER calculated from the simplified model, the geometric model provides an advantage in the ease and speed of its calculation. We note, however, that our implementation of the geometric model still involves a

convolution with the physical optics point spread function in order to determine the relevant image plane wavefront slopes.

We also notice that for the $NA = 0.5$ imaging system, the location of the peak in LER has shifted to the slightly lower mid-spatial frequency of correlation length of 20 nm. This is consistent with the earlier prediction [70] that the location of this peak is independent of the feature size, and is tied directly to the resolution of the objective (about $0.62\lambda/NA$). In order to meet the ITRS [1] benchmark of 1.7 nm total combined LER, and assuming an RSR of 50 pm, the correlation length should be greater than approximately 50 nm to limit the mask roughness induced LER contribution to under 0.3 nm. Surprisingly, the stringency of this correlation length requirement is relaxed for the $NA = 0.5$ system in comparison to the $NA = 0.32$ system, where the LER peak was much broader and shifted slightly towards lower spatial frequencies. This allows shorter correlation lengths to be much more tolerable in the $NA = 0.5$ case. In addition, there is the added benefit of greatly reduced contribution of mask roughness induced LER for all correlation lengths for the $NA = 0.5$ system. This is due to the fact that the higher NA does a better job replicating the pure phase function, thus reducing the coupling to speckle. This is in opposition to the effect on mask LER where the higher NA will also do a better job replicating the mask LER (less filtering of the mask LER).

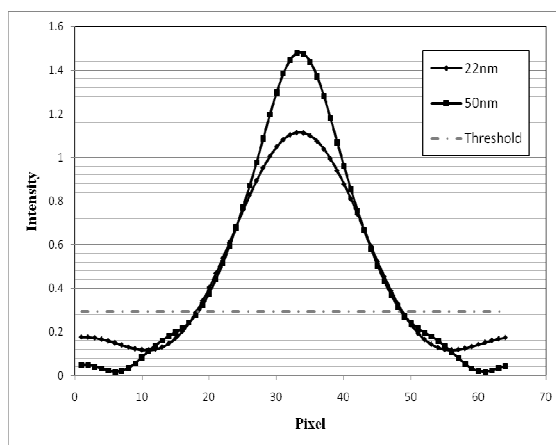


Fig. 57. 1D Aerial images for a partial coherence of $\sigma = 0.15$, $NA = 0.5$, as a function of horizontal position for 50 nm lines and spaces at a defocus of -50 nm where the horizontal scale is 1.56nm / 1 pixel, and for 22 nm lines and spaces at a defocus of -30 nm where the horizontal scale is 0.6875 nm / 1 pixel.

We note that in Fig. 55 for the $NA = 0.5$, the LER for 22 nm lines and spaces (at a defocus of -30 nm) seems much better than that for 50 nm (at a defocus of -50 nm), disproportionate to the slight shift in defocus between them. We therefore recalculated all the data for the case of 50 nm lines and spaces at a defocus setting of -30 nm for direct comparison in Fig. 56. We see that despite the shift in defocus, the LER for 50 nm lines and spaces remains worse than for the 22 nm case. To investigate more closely, we directly plotted the 1D aerial image simulations in Fig. 57. The diamond marker is the aerial image of 22 nm at a defocus of -30 nm and the square marker is that for 50 nm at a defocus of -50 nm just for one disk illumination of $\sigma = 0.15$. From this, it is clear that the 50 nm lines and spaces begin to exhibit a feature that is indicative of higher NA systems for larger CD, where higher diffracted orders (above order ± 1) begin entering the pupil and add characteristic sidelobes to the aerial image. Because these sidelobes are

present in the 50 nm feature in the threshold region, the ILS is adversely affected, and manifests itself in an LER value which is inferior to the smaller 22 nm feature. Although this potential problem could be readily addressed by proper biasing at the mask, it is interesting to note that the ability of the simplified model to accurately predict this anomalous behavior is indicative of the generality of the method.

Chapter 7

Control and Mitigation

With the NXE 3300B shipping beginning 2012, aberrations levels for the optical system lie at about 0.77nm rms [11]. As presented in previous chapters, recent progress has been made in understanding the extent of mask roughness induced LER [71], but only in the case of ideal optics. The work presented in this chapter is an extension of that effort to understand the nature of mask roughness induced LER in the presence of optical aberrations. We also consider an alternative illumination scheme specifically aimed at mitigating mask roughness induced LER.

7.1 Aberrations

As presented earlier, the sensitivity of LER to speckle is determined by the image-log-slope (ILS). A smaller ILS indicates larger line-edge movements for a given increment of intensity variation, e.g., speckle. In the presence of aberrations of the imaging optic, the imaging quality is degraded, as manifest in a smaller ILS. For instance, in considering defocus as an aberration, it is well-known that the ILS worsens as more aberration (defocus) is introduced into the system, and consequently, the susceptibility to speckle increases accordingly. We present here a full aberration sensitivity study on the mask roughness induced LER for the first 37 Fringe Zernikes conducted with fully simulated 2D aerial image modeling. This was done for both 22-nm and 16-nm lines and spaces using potential illumination conditions for each of those nodes respectively, with an NA of 0.32. Mask roughness conditions were set at a replicated surface roughness (RSR) value of 100 pm, a correlation length of 32 nm, and a roughness exponent of infinity [73]. Since the ideal RSR specification for commercialization of EUVL at the 22-nm node is less than 50 pm, and furthermore, since it has been shown that a 32 nm correlation length sits directly on the peak of mask roughness induced LER (determined by the objective NA) [71], these results represent a worst-case scenario. The modeling for the 22-nm features are presented in section 2, and that for 16-nm is presented in section 3. We present results for an aberration distribution of zero mean, as well as an individual aberrations sensitivity matrix where we concentrate the full aberration in one Zernike at a time [83].

7.1.1 Aberrations at the 22-nm half-pitch node

Following the numerical analysis of mask roughness induced LER described elsewhere [2,71], we randomly generated a mask object that was 1024×1024 pixels at 1 nm / pixel with 1:1

imaging to the wafer plane. This statistical representation of a clear rough mask was then appropriately scaled so that the standard deviation of this height map matched the desired RSR value of 100 pm and a correlation length of 32 nm.

This was done for disk illumination with a partial coherence factor $\sigma = 0.50$, first for an aberration-free optical system with $NA = 0.32$ from through focus from -90 nm to +90 nm. The low NA allows for scalar and thin mask modeling. The mask roughness induced LER results for the 22-nm lines and spaces are presented in Figure 58. The results indicate that one single statistical realization of the rough mask well represents the entire ensemble for an ideal pupil map.

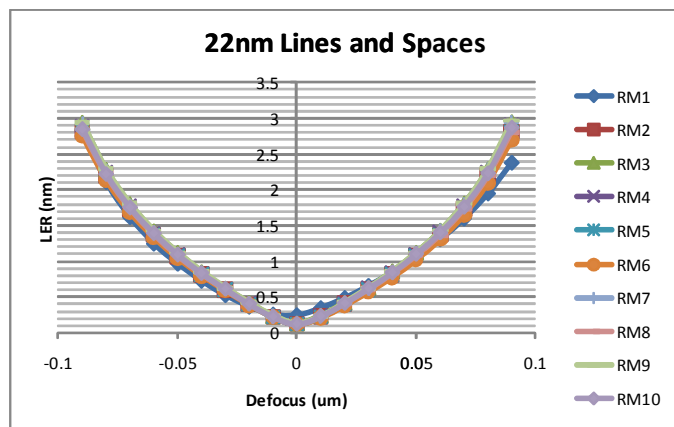


Fig. 58. 10 random rough mask realizations all with RSR 100pm, correlation length 32nm, on an ideal pupil map of $NA = 0.32$ with disk illumination of $\sigma = 0.50$ for 22nm lines and spaces.

Next we repeat the simulations, now introducing aberrations into the system. We randomly generated a distribution in Fringe Zernikes 5 through 16 (ignoring the first four: piston, x-tilt, y-tilt, and power), and scaled to 0.25 nm rms wavefront deviation, or 18.5 milliwaves. This was repeated to generate an ensemble of 10 random realizations all with 0.25 nm rms wavefront deviation for Fringe Zernikes 5 through 16 (Figure 59). This same distribution amongst Fringe Zernikes 5-16 was scaled up for two higher levels of aberrations, one at 0.50 nm rms wavefront deviation (37.0 milliwaves) and also at 0.75 nm rms wavefront deviation (55.6 milliwaves).

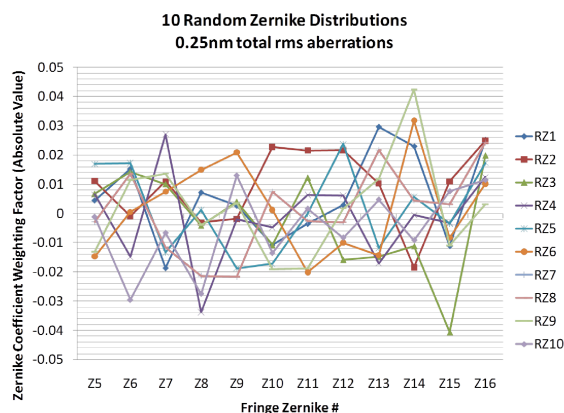
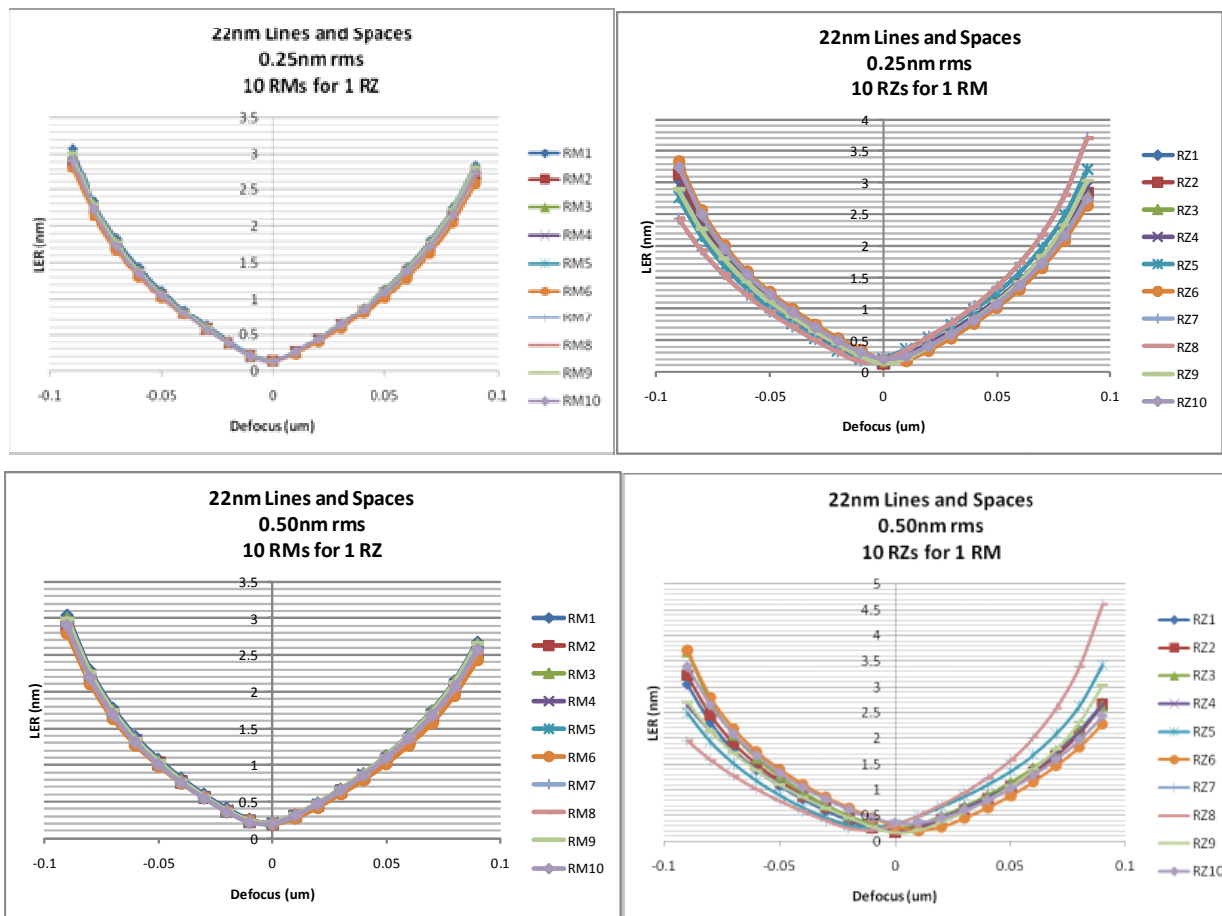


Fig. 59. 10 random Zernike distributions for zero-mean 0.25nm rms levels across Fringe zernikes 5-16.

Initially, we consider the variation of just one random realization of the Zernike distribution against all 10 random realizations of the rough mask. The simulation results for mask roughness induced LER through focus are presented in Figure 60. The results indicate that just one realization of the mask roughness well represents the entire ensemble at all levels of aberrations. Using, therefore, just one realization of the mask roughness, we next consider the variations in mask roughness induced LER by the previously generated 10 random realizations of the Zernike distribution in Fringe Zernikes 5-16. Those results are seen in Figure 61. We see that as the amount of aberrations increase from 0.25 nm to 0.50 nm total wavefront deviations, the consistency of one random realization of the Zernike distribution to another gradually decreases. At the 0.25 nm wavefront deviation level, the ensemble seems internally consistent even at large defocus, to within 1 nm LER of each other. At the 0.75 nm wavefront deviation level, individual realizations of the ensemble may deviate by as much as 3.5 nm LER from each other. This wide variation in resultant LER levels indicates that the system is highly sensitive to particular Fringe Zernike aberrations.



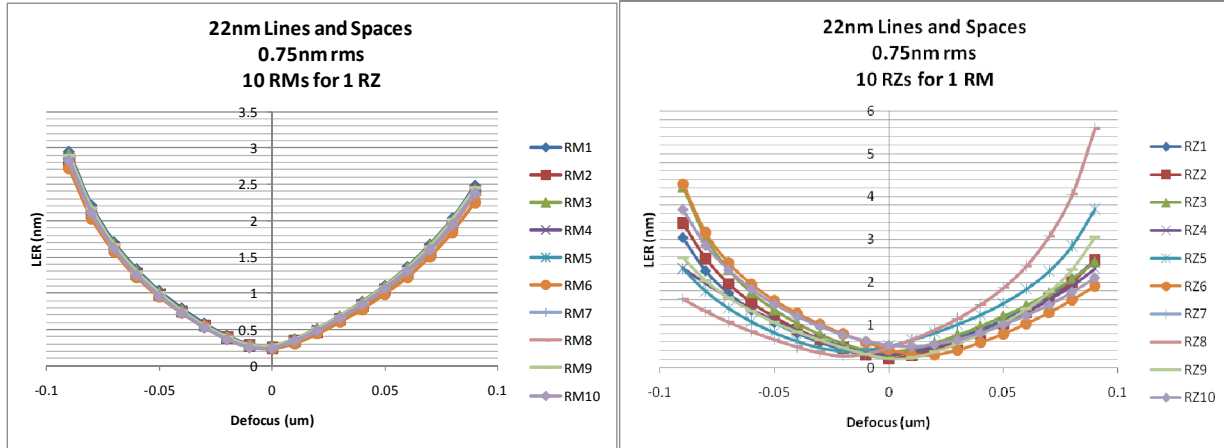


Fig. 60. (left column) 10 random rough mask realizations (RMs) all with RSR 100pm, correlation length 32nm, on 1 random Zernike distribution (RZ) amongst fringe zernikes 5-16 for total aberrations levels of 0.25, 0.50, and 0.75nm rms, with an NA = 0.32 with disk illumination of $\sigma = 0.50$ for 22nm lines and spaces.

Fig. 61. (right column) 1 random rough mask realization (RM) all with RSR 100pm, correlation length 32nm, on 10 random Zernike distributions (RZs) amongst fringe zernikes 5-16 for total aberrations levels of 0.25, 0.50, and 0.75nm rms, with an of NA = 0.32 with disk illumination of $\sigma = 0.50$ for 22nm lines and spaces.

Despite the significant variations between each individual realization of the Zernike distribution, we averaged the 10 realizations for each level of aberrations and plotted them against one another (see Figure 62). These results indicate as a general trend, improving the level of total aberrations in the imaging system has a minimal effect on the mask roughness induced LER, except for a noticeable difference at best focus.

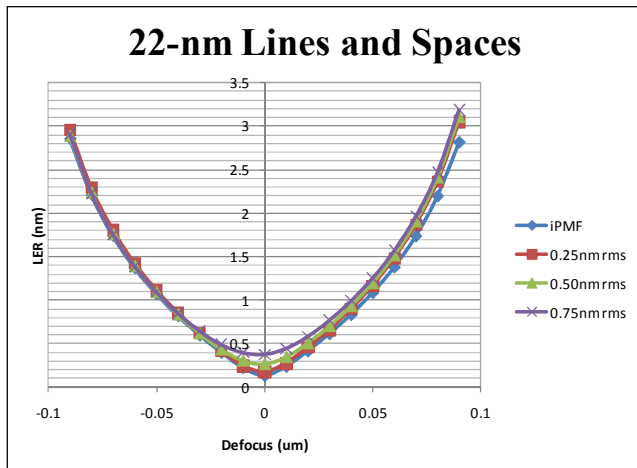


Fig. 62. 1 random rough mask realization (RM) all with RSR 100pm, correlation length 32nm, averaged against 10 random Zernike distributions (RZs) amongst fringe zernikes 5-16 for total aberrations levels of 0.25, 0.50, and 0.75nm rms, with NA = 0.32 with disk illumination of $\sigma = 0.50$. For “iPMF”, this indicates the average of the 10 RMs on an ideal pupil map graphed previously in Figure 55.

To investigate this further, we conducted a sensitivity matrix study of Fringe Zernikes 5 through 37. For instance, in looking at Fringe Zernike 5, we concentrated all aberrations within this one

Zernike, and modeled on just one realization of mask roughness. We did this for three levels of aberrations (0.25 nm, 0.50 nm, and 0.75 nm rms wavefront deviations), again for Zernikes 5 through 37. Those results can be seen in Figure 60. At the 0.25 nm rms wavefront deviation level, we see that the process is in particular sensitive to Fringe Zernikes 5 (3rd order astigmatism) and 8 (3rd order spherical), and to some extent 25 (7th order spherical). The sensitivity to these particular Fringe Zernikes remain consistent at the higher levels of aberrations (0.50 nm and 0.75 nm wavefront deviations). We note that in the case of each other Fringe Zernike, there is not much variation, even amongst the different aberration levels: all converge to approximately the 2.5 nm to 3 nm LER range at extreme defocus values, no matter if the wavefront deviations are at the 0.25 nm rms level or the 0.75 nm rms level. This is consistent with Fig. 59, where, again, improvements in total wavefront deviations across the distribution of Fringe Zernikes 5-16 minimally affected the mask roughness induced LER. Efforts should rather be made in improving the mask surface roughness specifications such as RSR and correlation length, which as shown previously [71], can have a much more significant or at least comparable impact. However, in practice, it might be difficult to significantly improve the RSR beyond 100 pm.

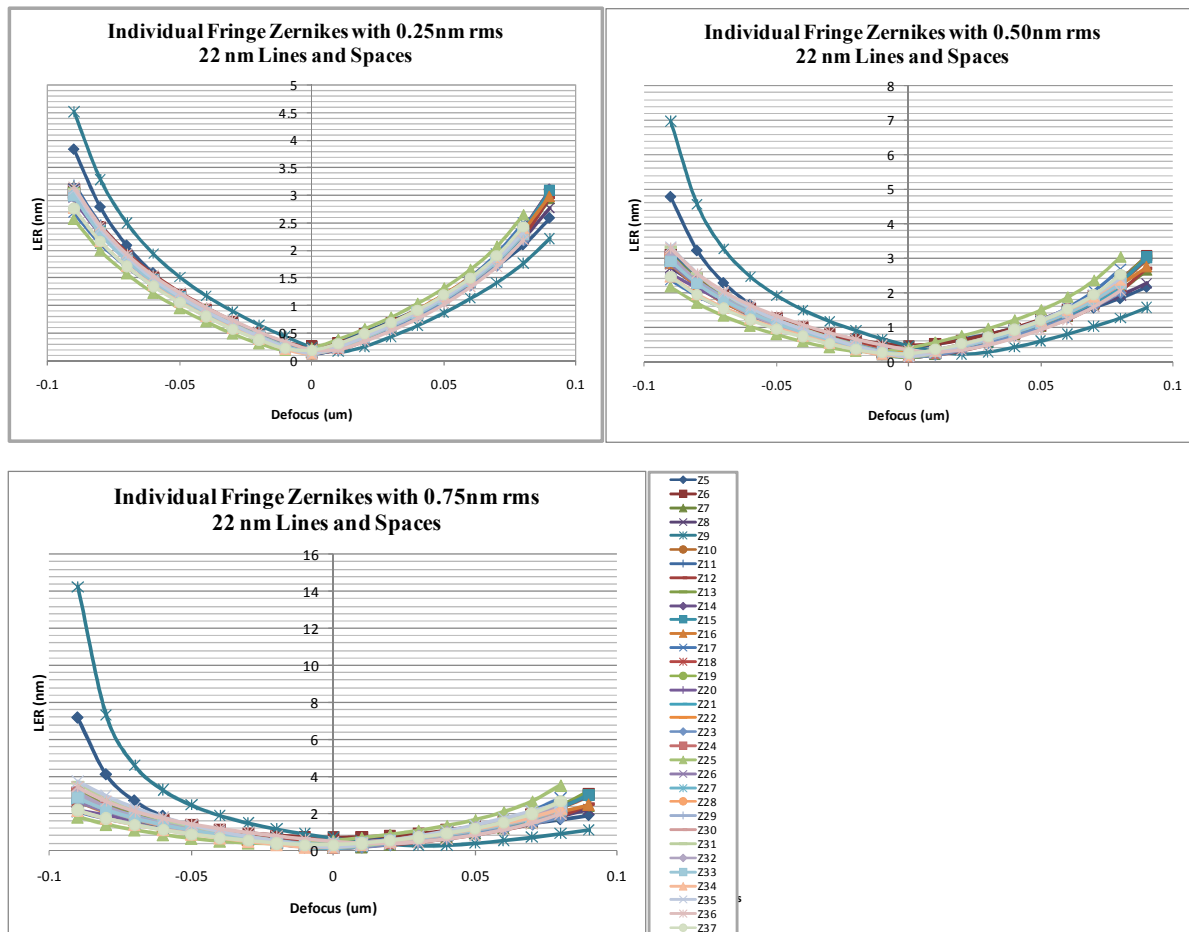


Fig. 63. 1 random rough mask realization (RM) all with RSR 100pm, correlation length 32nm, on each individual fringe zernike 5-37 for a concentrated aberration level in that fringe zernike of 0.25, 0.50, and 0.75nm rms, with an of NA = 0.32 with disk illumination of $\sigma = 0.50$ for 22nm lines and spaces.

7.1.2 Aberrations at the 16-nm half-pitch node

We repeat the entire analysis above now for 16-nm lines and spaces case, again with an NA = 0.32, RSR of 100 pm, and a correlation length of 32 nm. The only difference is a change in illumination conditions, now set to crosspole illumination with $\sigma = 0.10$ and an offset of $d_x = 0$ and $d_y = .67$ in sigma space. Crosspole was chosen to enable simultaneous printing of horizontal and vertical lines, as quadrupole illumination was not accessible at this NA and pitch.

Following the analysis process above, we started with simulating an aberration-free optical system with NA = 0.32 again for a focal range of -90 nm to +90 nm. After appropriately sizing features to target CD at best focus, the results are presented in Figure 64 and show that once again each statistical realization of the rough mask well represents the entire ensemble for an ideal pupil map.

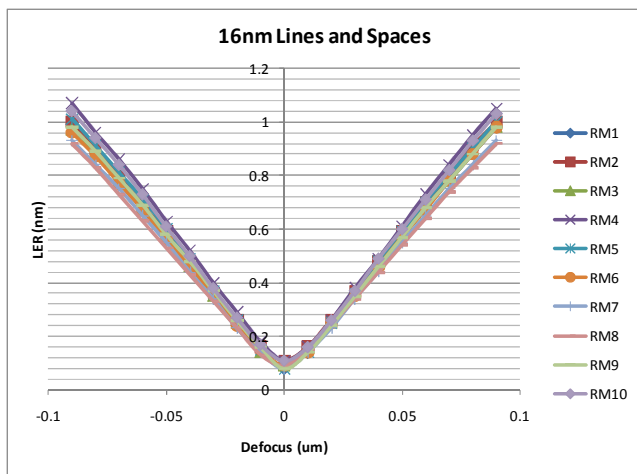


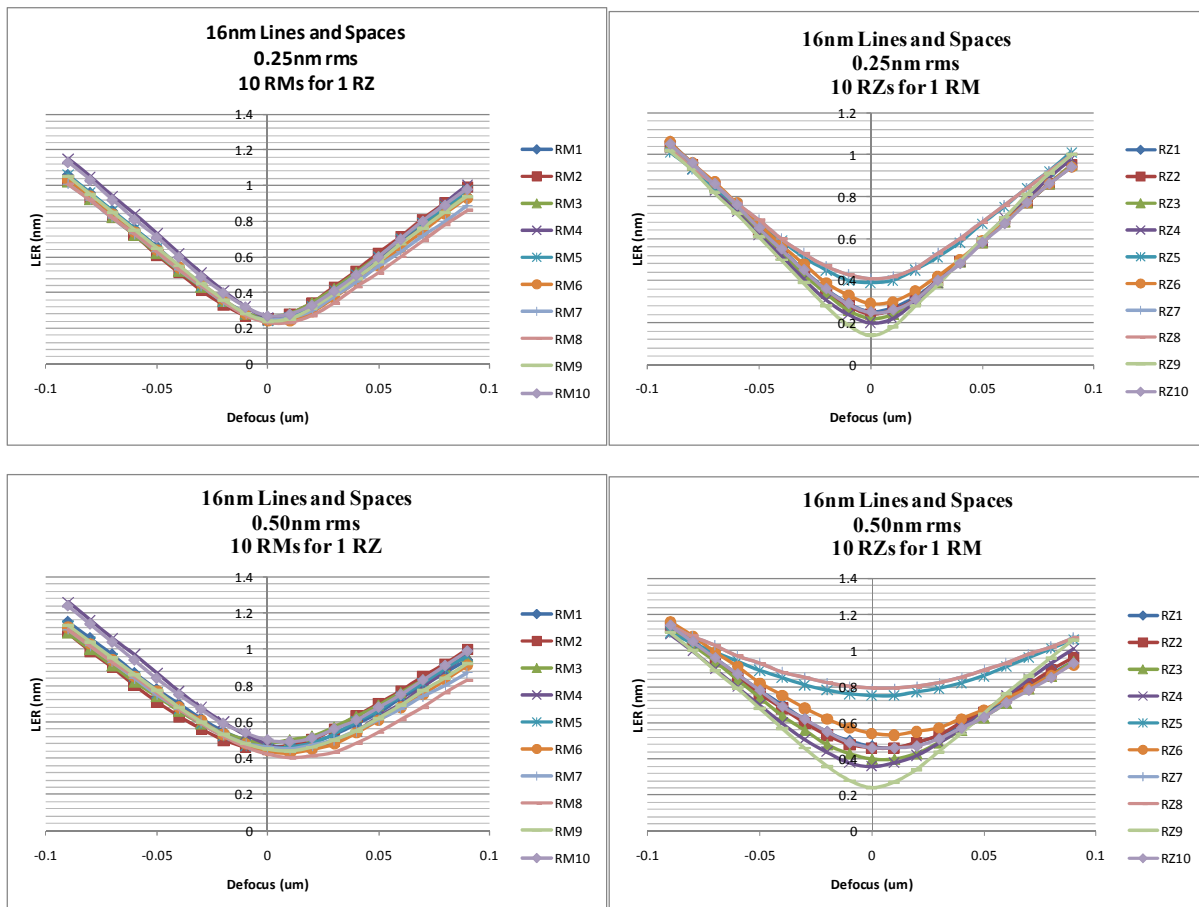
Fig. 64. 10 random rough mask realizations all with RSR 100pm, correlation length 32nm, on an ideal pupil map of NA = 0.32 with crosspole illumination of $\sigma = 0.10$ optimized for 16nm lines and spaces.

Now introducing aberrations into the system, we once more consider the variation of just one random realization of the Zernike distribution over Fringe Zernikes 5 through 16, against all 10 random realizations of the rough mask (for overall aberration levels of 0.25, 0.50, and 0.75 nm rms). The results similarly indicate that just one realization of the mask roughness well represents the entire ensemble at all levels of aberrations (see Figure 65). We therefore continue with our previous simplification, and use just one realization of the mask roughness for the rest of our analysis. As this single mask roughness realization is sampled across the same previously generated 10 random realizations of the Zernike distribution in Fringe Zernikes 5-16, the dependency of LER on which realization of the Zernike distribution remains quite small at the 0.25 nm rms level, with substantial deviations (~ 0.2 nm LER) between realizations only observed at best focus (see Figure 66). As overall aberrations increase to the 0.50 and 0.75 nm level, these deviations become quite large at best focus, as much as 0.8 nm LER increase at zero defocus, while the LER remains pinned to about 1-1.2 nm LER at the extremes of focus (again, see Figure 66). From this, we conclude that the system is still highly sensitive to particular fringe Zernike aberrations.

Once more, we conduct an averaging analysis of the 10 random realizations of the Zernike distribution, despite the significant variations in system LER performance between each realization. In contrast to the 22 nm lines and spaces case, at the 16 nm node, LER is significantly more sensitive to the overall aberrations level throughout focus. Aberration levels of 0.25 nm rms could perhaps be tolerated, which already sacrifice 0.3 nm LER at best focus (see Figure 67).

Finally, the sensitivity matrix study of Fringe Zernikes 5 through 37 revealed a particular sensitivity to Fringe Zernikes 8 and 24 (3rd and 7th order spherical), as well as 27 (5th order quadrafoil) at the 0.25 nm rms level (see Figure 68). These particular aberrations remain dominant at higher aberration levels as well.

We note that the results above are extremely dependent not only on the nominal feature sizes of 16 and 22 nm, but also the type of illumination (crosspole $\sigma = 0.10$ and disk $\sigma = 0.50$ respectively, in this case). The overall levels of LER should improve accordingly with a significant reduction in the RSR value, and/or shift in the correlation length.



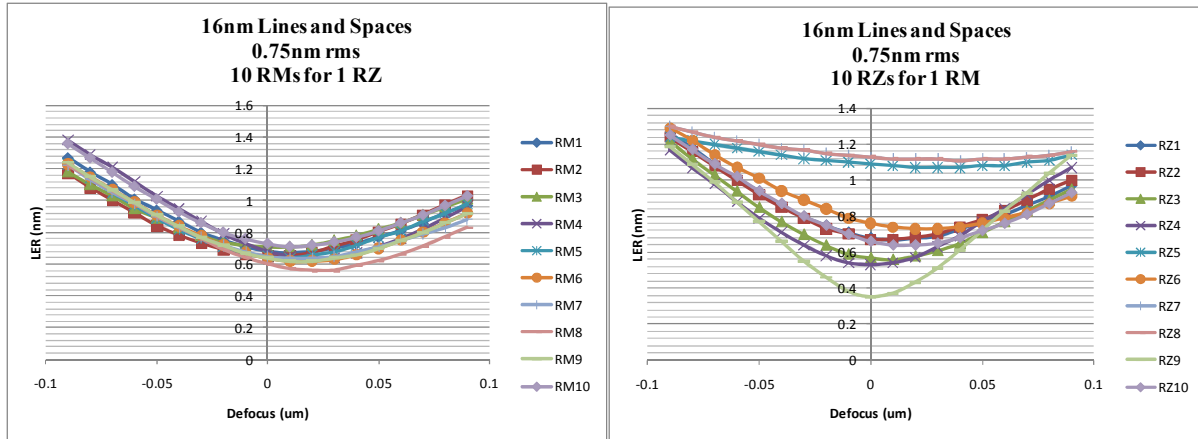


Fig. 65. (left column) 10 random rough mask realizations (RMs) all with RSR 100pm, correlation length 32nm, on 1 random Zernike distribution (RZ) amongst fringe zernikes 5-16 for total aberrations levels of 0.25, 0.50, and 0.75nm rms, with crosspole illumination of $\sigma = 0.10$ optimized for 16nm lines and spaces.

Fig. 66. (right column) 1 random rough mask realization (RM) all with RSR 100pm, correlation length 32nm, on 10 random Zernike distributions (RZs) amongst fringe zernikes 5-16 for total aberrations levels of 0.25, 0.50, and 0.75nm rms, with an of NA = 0.32 with crosspole illumination of $\sigma = 0.10$ optimized for 16nm lines and spaces.

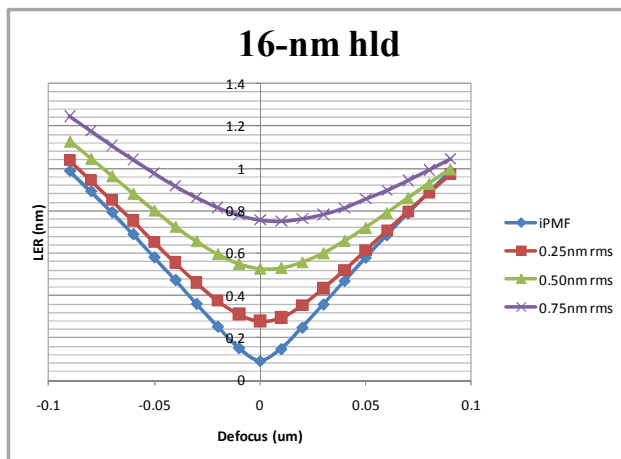


Fig. 67. 1 random rough mask realization (RM) all with RSR 100pm, correlation length 32nm, averaged against 10 random Zernike distributions (RZs) amongst fringe zernikes 5-16 for total aberrations levels of 0.25, 0.50, and 0.75nm rms, with NA = 0.32 with crosspole illumination of $\sigma = 0.10$ optimized for 16nm lines and spaces. For “iPMF”, this indicates the average of the 10 RMs on an ideal pupil map graphed previously in Figure 6.

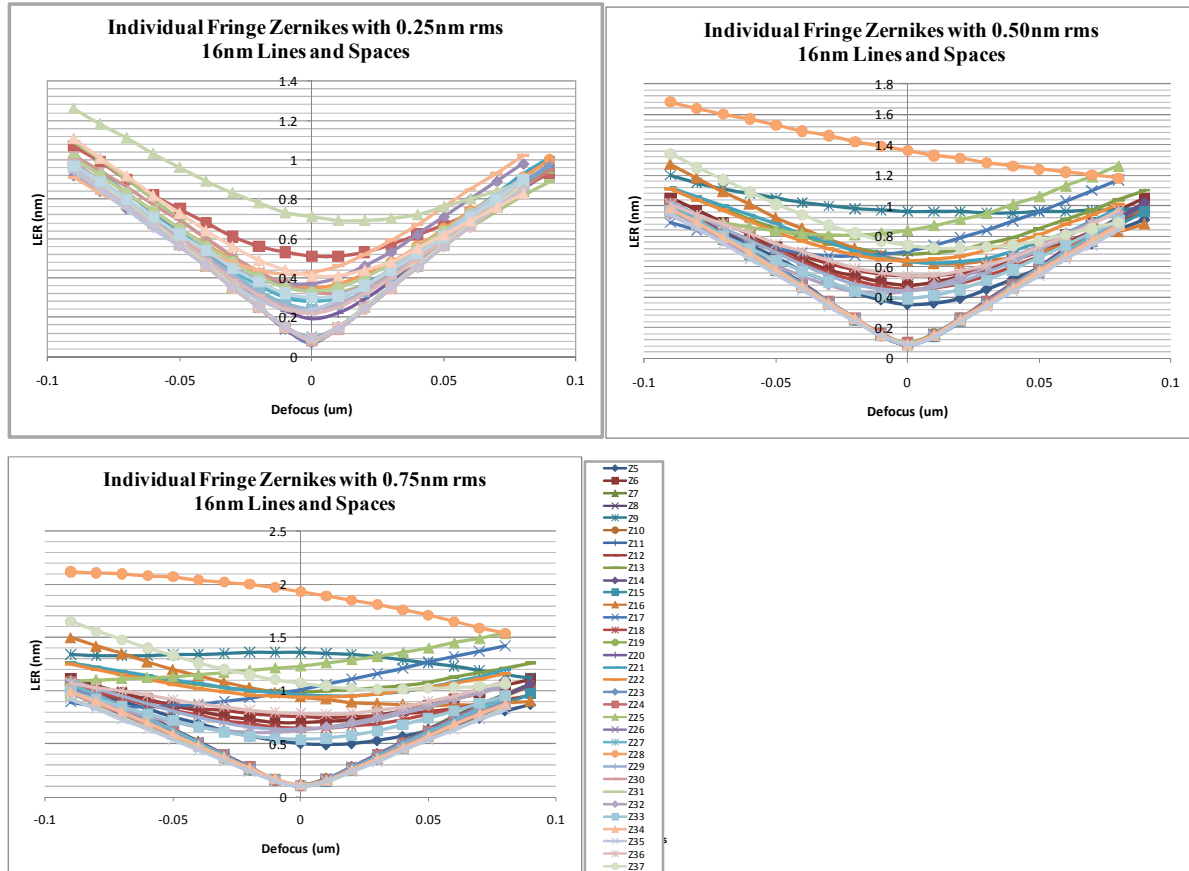


Fig. 68. 1 random rough mask realization (RM) all with RSR 100pm, correlation length 32nm, on each individual fringe zernike 5-37 for a concentrated aberration level in that fringe zernike of 0.25, 0.50, and 0.75nm rms, with an of NA = 0.32 with crosspole illumination of $\sigma = 0.10$ optimized for 16nm lines and spaces.

7.2 Mitigation through Extended Dipole Illumination

We have explored the explicit relationship between speckle (and hence source coherence), aerial image (through image-log-slope, ILS), and LER [71]. From this basic relationship, we can conclude that if speckle is reduced while maintaining good ILS, indicative of good imaging quality, LER should be mitigated. Once such way we can envision doing this is by an alternate illumination scheme whereby a traditional dipole angular spectrum is extended in the direction parallel to the line-and-space mask absorber pattern to represent a "strip". We hypothesized that this reduction in coherence in direction parallel to the predominant pattern orientation should effectively reduce the speckle arising from mask roughness, while the high coherence in the orthogonal direction should maintain good resolution and high ILS.

7.2.1 LER Performance – optimal stage

We conducted our analysis by gradually extending the dipole from an initial $\sigma = 0.20$ radius (properly displaced for 16 nm lines and spaces at $dx = 0$ and $dy = .67$ in sigma space) in four gradual steps, each time increasing the length of the dipole by $\Delta x = 0.20$ in sigma space to either

side of the dipole (see Figure 69). For each illumination condition, we modeled the system on an aberration-free $NA = 0.32$ optic, 13.5-nm illumination wavelength, and the same 10 random realizations ensemble of mask roughness for RSR 100 pm and correlation length of 32 nm used above.

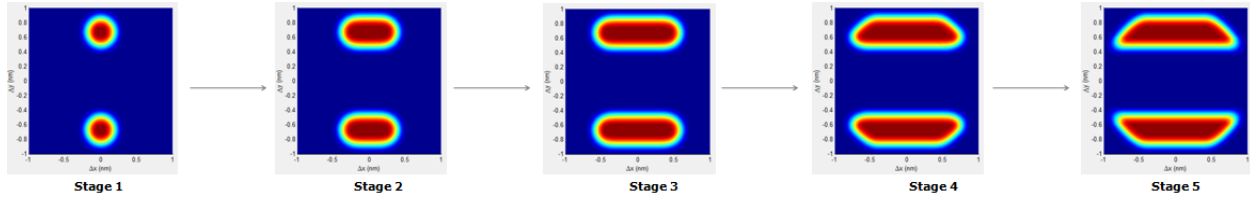


Fig. 69. The five stages of extended dipole illumination tested for LER sensitivity, starting with dipole illumination with intrinsic $\sigma = 0.20$ optimized for 16nm lines and spaces.

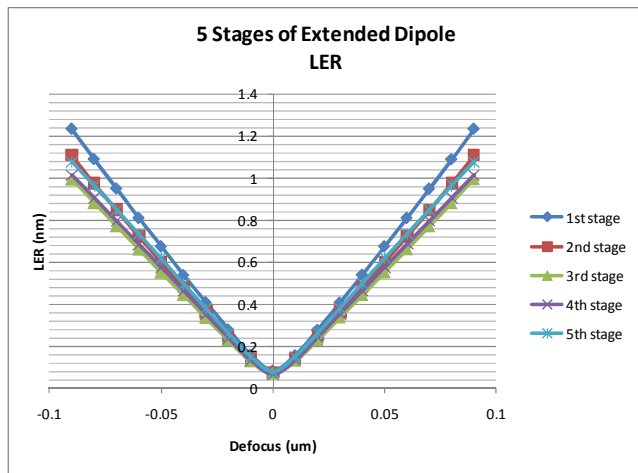


Fig. 70. The LER performance of the five stages of extended dipole.

Shown in Figure 70 are the five stages of the extended dipole LER results plotted through focus. We observe that the extension of the dipole gradually benefits the LER (by about 0.2 nm LER at the extremes of focus) until the point that the dipole begins to be clipped by the pupil (after stage 3 extended dipole).

7.2.2 LER Performance against conventional illuminations

Compared directly to LER results of the crosspole illumination examined previously in section 3, this illumination surprisingly provides nearly the same LER values (see Figure 71). We suspect that this results because the LER seems to be governed by the so-called “geometric” regime, a concept that was explored in Chapter 6 [82]. Although there is little LER improvement with the extended dipole compared to the crosspole illumination scheme, a quick look at the imaging quality in terms of the traditional ILS and contrast (Figure 72) show that the extended dipole stage 3 offers potentially improved performance. Not to mention, the larger absolute source size may increase throughput at the wafer level. The surprisingly minimal improvement in LER with the extended dipole runs counter-intuitively to our initial hypothesis.

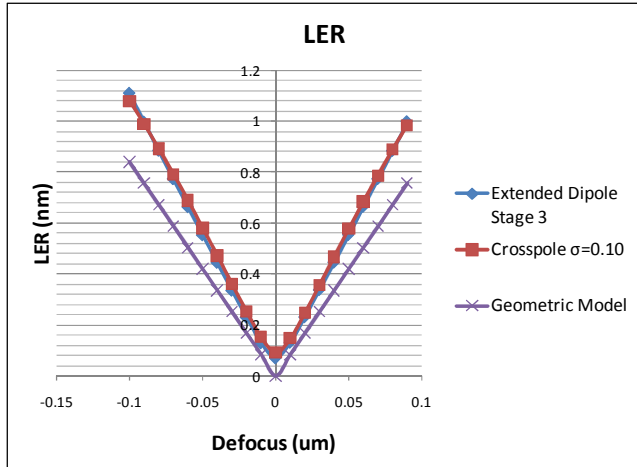


Fig. 71. LER comparison between the optimal 3rd stage of extended dipole, versus crosspole illumination of $\sigma = 0.10$ optimized for 16nm lines and spaces, and the geometric model.

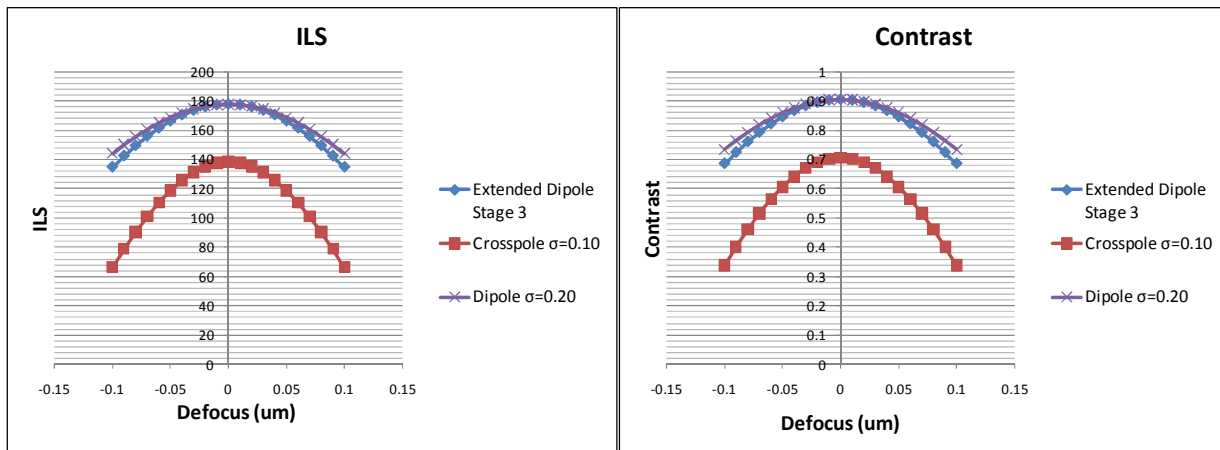


Fig. 72. ILS and Contrast comparison between the optimal 3rd stage of extended dipole, versus crosspole illumination of $\sigma = 0.10$, and the original dipole (1st stage of extended dipole) of $\sigma = 0.20$, all optimized for 16nm lines and spaces.

7.3 Conclusions

Our examinations of 22nm lines and spaces under disk illumination of $\sigma = 0.50$ and $NA = 0.32$ show that aberrations between 0.25-0.75 nm rms levels yield similar LER performance through focus. Efforts would be better spent on improving mask roughness characteristics. The individual Fringe Zernike study show a particular sensitivity to 5 (3rd order astigmatism) and 8 (3rd order spherical), and to some extent 25 (7th order spherical).

For 16-nm lines and spaces under optimized crosspole illumination of $\sigma = 0.10$ and $NA = 0.32$, overall aberrations levels should be limited to 0.25 nm rms. Fringe Zernikes 8 and 24 (3rd and 7th order spherical), as well as 27 (5th order quadrafoil) are particularly sensitive. As with the 22-nm node, aberration improvements should be made hand in hand with mask roughness improvements, as both are equally important from an LER perspective. Of course, all of the

results above are extremely dependent not only on the nominal feature sizes of 16 and 22 nm, but also the type of illumination used.

The extended dipole illumination stage 3 (intrinsically $\sigma = 0.20$) was explored for possible use at the 16-nm node may provide a minimal LER improvement, ILS, and contrast improvement over crosspole illumination ($\sigma = 0.10$), and greater throughput than traditional dipole illumination. Higher throughput, however, is only an option if source shapes are created through limiting apertures- something not of concern to EUVL litho tools that implement other methods.

Chapter 8

Application in Industry

In this chapter we examine the experimental effects on lithographic performance due to repetitive cleans on a mask patterned for use in extreme ultraviolet lithography (EUVL). The performance is measured against the process window for line edge roughness (LER) and contact size variation. Mask properties such as surface roughness, reflectivity, and aerial image monitoring were used as metrics of the cleaning process effects. We also introduce a new method involving the correlation in LER of a single line from exposure to exposure. Results presented in section 8.1 are those presented recently [84].

8.1 Mask cleaning effects of lithography process and lifetime

As extreme ultraviolet lithography (EUVL) nears commercial introduction, the lack of pellicle implies a viable mask cleaning strategy must be in place that effectively removes printable defects while at the same time not degrading reflectivity. Removal efficiency has been shown using acid-based wet cleaning for defects arising from storage, shipping and handling, exposure deposition, and chuck-induced ones on the mask backside. While the acid-based cleaning itself may potentially introduce defects, the effects of the aggressive acid cleaning process may cause greater damage to the mask itself, reducing lithographic performance (process latitude, line edge roughness, contact size variation, etc). It is estimated that the mask should survive at least 20 cleaning cycles to meet HVM lifetime goals. To ensure this within a safe margin, the cleaning process should exhibit minimal impact through 30 cleaning cycles, which has been shown in recent work [84-86].

Following previous methods, we examine the effects on lithographic performance due to cleans on a mask patterned for use in EUVL. Exposures were carried out at the SEMATECH Berkeley micro-exposure tool (MET) on both a cleaned mask and a reference (uncleaned) mask with the same mask architectures. The performance is measured against the process window for lines and spaces, line edge roughness (LER), and contact size variation measured using scanning electron microscopy (SEM). Mask properties such as surface roughness and reflectivity were used as metrics of the cleaning process effects. We also introduce a new method involving the correlation in LER of a single line from exposure to exposure at the same dose and focus. If mask cleaning were to introduce significant damage to either the capping layer or the absorber, we would expect an increase in LER correlation from exposure to exposure of the same feature,

as uncorrelated effects due to the resist would be unaffected by the cleans. We look at these metrics on the same mask used in previous cleans studies, now for a 33× cleans.

Two masks with identical fabrication processes were examined, one of which was processed with the acid-based cleaning chemistry, and the other kept pristine as a reference. The process mask was subjected to 50 and 75 cleaning cycles during which lithographic performance (process window analysis and line edge roughness). Surface roughness was also monitored every 2-4 cleans for comparison to the reference mask. Reflectivity data was gathered on a witness plate by EUV reflectometry.

Two masks were fabricated from commercially available EUV blanks with identical stacks—substrate, Mo/Si multilayer with Ru cap and absorber. The same layout design was used for patterning exposure on the Berkeley MET. One of the masks was subjected to 33 cleaning cycles, and the other was kept pristine as a reference.

A standard acid-based recipe formulated for resist strip was used for each of the cleaning cycles. The process comprises two main components—a sulfuric acid/hydrogen peroxide mixture (SPM) followed by SC1 with megasonics.

Exposure was performed on the SEMATECH Berkeley MET at the Advanced Light Source synchrotron facility at Lawrence Berkeley National Laboratory [87-88]. Imaging was done using an annular illumination with an inner sigma of 0.35 and an outer sigma of 0.55, an illumination angle of incidence 4 degrees parallel to the line printing results presented here.

The same subfield area of the mask was used throughout the imaging studies on standard BBR-08A resist. The patterns in resist were recorded using a top-down SEM (Hitachi FE-SEM S-4800) and analyzed offline with the software package SuMMIT [79]. Each data set consisted of an 11×11 focus exposure matrix (FEM), with focus step size of 50 nm and 5% exponential dose steps.

Process data for two sets of vertical, 1:1 line and space patterns (at critical dimensions of 40nm and 36nm for process window and LER analysis, and 50nm for LER correlation analysis) and two sets of contacts (at critical dimensions of 50nm and 45nm) were collected for both process and reference masks. The reference mask was imaged alongside the process mask each time thus enabling us to monitor any system and process related effects over the long time span of this study.

A Digital Instruments atomic force microscope (AFM) was used to measure surface roughness at regular intervals (typically every 2-3x) to measure integrity of the Ru capping layer. This AFM is capable of measuring sub-angstrom level root-mean-squared (rms) roughness, using a probe with nominal tip radius of 8nm in tapping mode. Each image comprised a field of view of 2×2μm.

A witness mask was used for reflectivity data with identical stack as the process mask. The witness mask was subjected to the same cleaning process and its EUV reflectivity measured at periodic intervals with an EUV Technology reflectometer.

8.1.1 Lines and spaces, LER, and contacts

The process metrics extracted from the collected wafer images are shown in Table 1. We look at exposure latitude percent (EL), depth of focus (DOF), and LER. The DOF is determined based on an elliptical fit to the +/-10% CD-change process window. EL and DOF data for both features have less than 5% variation and so are well within the process uncertainty, expected to be anywhere from 5% to 10% for normal wafer-to-wafer MET operation conditions. The EL trend is plotted in Figure 73.

The averaged, 3σ LER is also found in Table 1. Variations between the process and reference masks are below the measurement uncertainty of ± 0.40 nm. The LER is plotted in Figure 74.

Table 1. Process comparison of all relevant parameters for 1:1 40nm and 36nm lines and spaces patterns.

# of Cleans	40nm CD, 1:1 lines						36nm CD, 1:1 lines					
	Cleaned Mask			Reference Mask			Cleaned Mask			Reference Mask		
	EL	DOF	LER	EL	DOF	LER	EL	DOF	LER	EL	DOF	LER
2	18.8	319.7	4.03	16.6	292.9	4.21	16.5	306.3	4.13	16.7	303.3	4.32
4	16.3	330.6	3.96	15.4	335.6	3.98	16.1	294.4	3.99	11.9	185.1	4.14
6	16.0	245.3	4.24	13.3	200.7	4.02	14.8	239.4	4.15	13.4	212.3	4.25
8	15.5	287.5	4.25	14.7	155.2	4.19	14.0	308.5	4.01	12.7	181.4	4.48
14	25.4	302.0	3.31	22.0	256.0	3.21	22.3	320.0	3.52	19.6	304.0	3.40
16	24.3	247.6	3.42	21.9	226.4	3.36	21.0	261.7	3.82	20.3	253.8	3.60
18	20.6	260.0	3.45	19.6	180.1	3.52	20.2	260.0	3.74	16.4	193.3	3.83
22	22.8	300.0	3.47	21.3	334.0	3.19	19.1	252.0	3.65	18.8	271.0	3.21
33	24.3	296.8	5.87	24.3	305.0	5.84	19.5	321.0	5.57	23.3	240.0	6.16

EL is in %, DOF and LER are given in nm units.

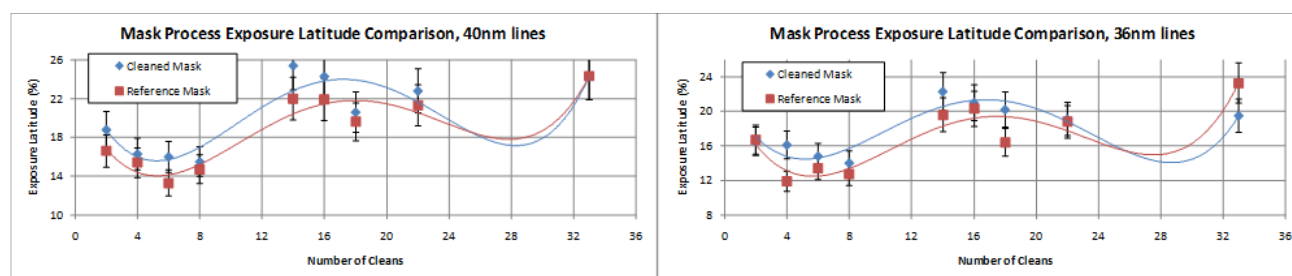


Fig. 73. Exposure latitude comparison throughout the mask clean studies for both the process mask and the reference mask. Any system level changes and resist level changes are accounted for by comparing the two masks. All observed changes are within the statistical limit of normal wafer-to-wafer patterning.

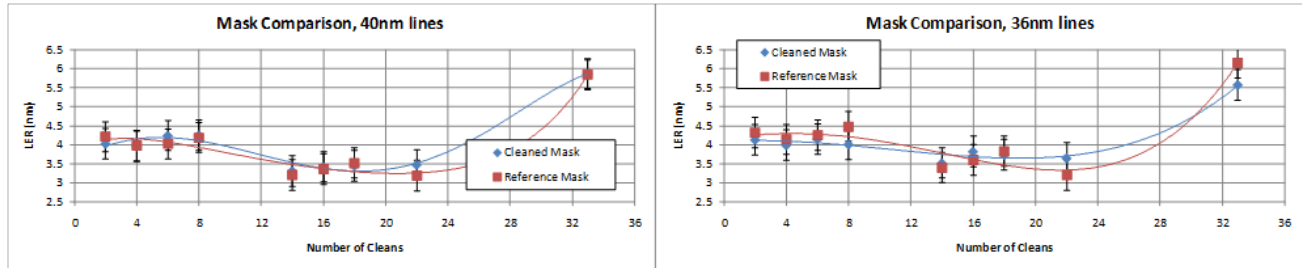


Fig. 74. LER trends for both the cleaned mask and the reference mask. Despite a noticeable increase at 33 cleaning cycles, the process and reference mask are close to one another. This indicates it was not due to mask pattern degradation.

Iso-focal feature widths indicate there is no damage to mask patterns, as both sets of patterns are observed to be nearly identical throughout the study. The data is tabulated in Table 2 for both line sets evaluated. Additionally, there is no indication of CD change. The uncertainty in the data is found to be near 2.0nm.

Table 2. Iso-focal matched and averaged CD comparison for all data at 40nm and 36nm line widths.

40nm lines	Cleaned Mask		Reference Mask		36nm lines	Cleaned Mask		Reference Mask	
	CD_ave (nm)	E_iso (mJ)	CD_ave	E_mJ		Cleans	CD_ave (nm)	E_iso (mJ)	CD_ave
	38.2	15.24	39.0	14.38	2	34.4	15.24	35.2	15.10
	37.5	15.23	39.8	14.16	4	34.5	15.23	34.1	13.81
	39.9	14.88	38.0	13.94	6	35.2	15.63	34.1	14.29
	39.0	15.24	40.2	14.17	8	36.1	15.24	35.4	14.51
	38.2	18.14	39.3	19.81	14	35.9	18.14	34.8	19.81
	37.2	16.80	39.8	16.20	16	34.7	16.80	34.4	16.80
	39.4	16.00	39.8	17.18	18	34.6	16.80	34.6	17.60
	38.9	16.54	39.6	15.38	22	34.6	16.54	35.3	15.75
	41.4	16.89	40.3	17.64	33	37.0	16.89	35.9	17.64

Contact features are very sensitive to changes in surface damage and pattern edge roughness. This results in a change of CD and increase of contact size standard deviation [89]. For the process mask wafer data, statistical changes in size and standard deviation were not seen between the start of cleaning and the end of 33 cleaning cycles for the contact data. (Table 3).

Table 3. Critical dimensions and standard deviation values for 50nm and 45nm contact features at the beginning and end of the study.

# of Cleans	50nm CD, contacts				45nm CD, contacts			
	Cleaned Mask		Reference Mask		Cleaned Mask		Reference Mask	
	CD	STD	CD	STD	CD	STD	CD	STD
2	48.78	1.87	47.97	1.97	41.66	2.33	39.33	2.23
33	49.25	1.29	49.81	1.28	42.94	1.5	44.08	1.56

8.1.2 Mask surface roughness

Mask surface roughness was monitored at regularly with AFM to determine the impact of the cleaning on the integrity of the Ru capping layer. Additionally, the mid-spatial frequency roughness (MSFR) with wavelength of 0.1-1.0 μm was extracted from the raw surface roughness data as a separate metric. MSFR is advantageous for being less sensitive to AFM measurement noise/variation and tip artifacts, which pollute high-spatial frequency roughness (HSFR) measurements from an AFM. Figure 75 plots both raw surface roughness and MSFR with respect to cleaning cycles. After 33 cleaning cycles, raw surfaces roughness increased by 50pm, which represents a small change with respect to the noise floor of the AFM at 40pm. The MSFR shows a small increase too.

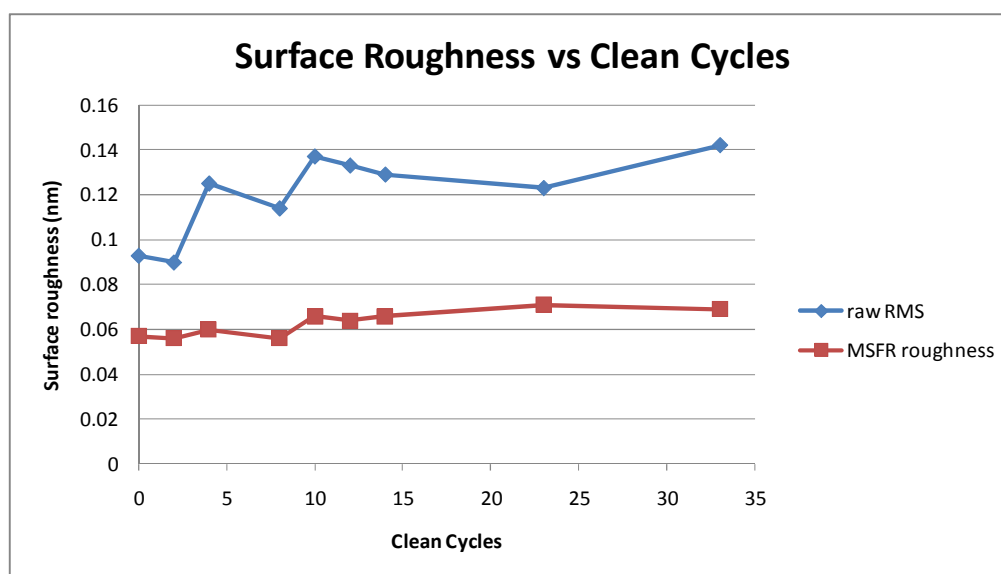


Fig. 75. RuML raw surface roughness and MSFR plotted with respect to cleaning cycles.

AFM images of the surface are shown in Figure 76. These images give a qualitative comparison of the surface between the initial, intermediate and final cleaning cycles. The height map of the surface increases commensurate with the values plotted in Figure 75. Overall, there were no observed gaping fissures, pinholes, or delamination seen.

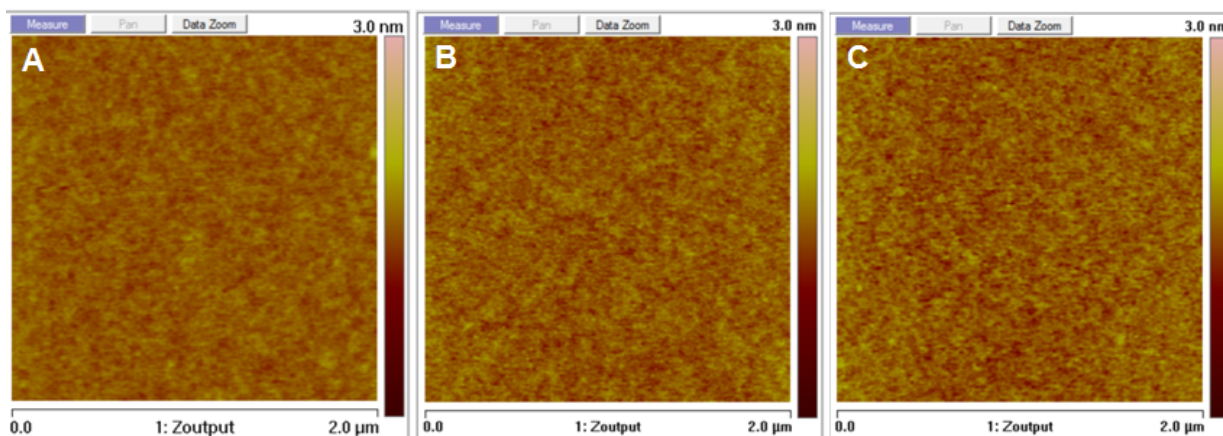


Fig. 76. AFM images of the Ru surface at a) beginning of study, b) after 14 cleaning cycles, c) after 33 cleaning cycles.

To characterize EUV reflectivity, a separate witness mask—from the same vendor and with the same material stack—was used in place of the processed mask. Because of the length of the study which spans a period greater than one year, a witness plate cleaned and measured within the span of one month minimizes the impact of measurement artifacts such as tool drift, calibration, and preventive maintenance interruptions. After 33 cleaning cycles, a 0.5% drop in reflectivity is observed; meaning, the cleaning process is compatible with HVM lifetime requirements whereby each mirror surface must suffer no greater than 1% loss of total reflectivity over its lifetime (expected to encapsulate a total of ~20 cleaning cycles). This can be seen in Figure 77.

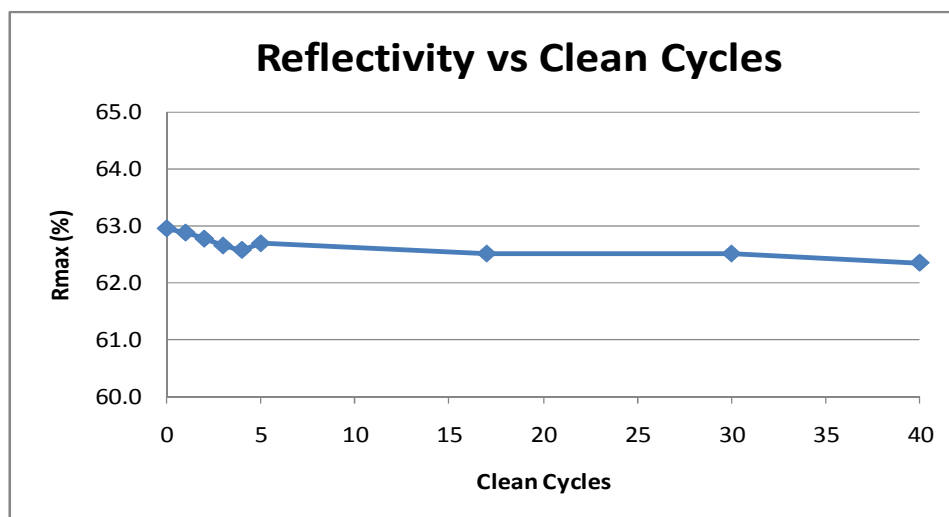


Fig. 77. EUV reflectivity of a witness plate shows a 0.5% drop after 33 cleaning cycles.

8.2 LER correlation method

If mask cleaning were to introduce significant damage to either the capping layer or the absorber, we would expect an increase in LER correlation from exposure to exposure of the same feature. We therefore utilize the recently introduced method [6] involving the correlation in LER of a

single line from exposure to exposure at the same dose and focus as a separate, independent means of measuring the possible impact of mask cleans.

There are two ways the mask can contribute to LER. Firstly, LER from the mask absorber couples to wafer LER by a transfer function [67-68] which is closely related to the modulation transfer function (MTF), where the difference lies in the complex 2D nature of LER. After the cleaning process, there are two possible outcomes. The first case would be that the cleaning could be damaging the multilayer, thereby lowering reflectivity and making features bigger at the same dose. The second case would be that the cleaning could eat away the absorber, thereby making features smaller at the same dose. The second contributor from the mask to wafer level LER is due to mask surface roughness in the bright, clear, reflective areas of the mask. At EUV wavelengths, the geometrical height deviations from the Ru cap surface result in significant optical path length differences in the emerging wavefront based on the index of refraction from the multilayer mirror resulting in phase roughness. This phase roughness couples to speckle in the aerial image [2,71], which in turn causes LER. These two mask LER contributors- both mask absorber LER and mask roughness induced LER- are assumed to be correlated from exposure to exposure of the same object in the same field on the mask, at same dose and focus. This is in contrast to resist sources of LER, such as acid shot noise, photo-acid generator uniformity, quencher uniformity, and blocking group uniformity, which will be random from exposure to exposure. Thus, by correlating line-edge roughness between multiple exposures of an identical region on the mask, invariant mask effects can be separable from random resist effects. The method is outlined in detail in previous work [6].

8.2.1 The method

The correlation method is based on the assumption that mask LER effects are correlated from exposure to exposure, and resist effects remain invariable. Following the analysis found elsewhere [6], let us define L as a random variable representing the deviation of the line edge from a straight line as a function of position along the line. (Traditionally, this random variable would be represented as a standard deviation, and the LER is three times that number). If we let L to represent the summation of two random variables M and R (such as for mask-induced edge deviation, M , and resist-induced edge deviation, R), then for any one realization (exposure) which is represented by the subscript i , the total edge deviation is

$$L_i = M_i + R_i.$$

As previously stated, the mask effects are assumed to be invariant from exposure to exposure, so all M_i are equivalent (completely correlated), and the subscript can be dropped. Then for two different exposures, for example, we have

$$L_1 = M + R_1 \text{ and } L_2 = M + R_2.$$

If we further assume zero mean random variables and also a stationary process so the statistics are invariant between exposures, then the correlation between L_1 and L_2 is now

$$\rho = E[L_1 L_2] / (\sigma_{L_1} \sigma_{L_2}).$$

By expansion and making use of an invariant process so that $\sigma_{L_1} = \sigma_{L_2}$, we have

$$\rho = E[(M + R_1)(M + R_2)] / (\sigma_L^2),$$

$$\rho = E[(M^2 + R_1 R_2 + MR_1 + MR_2)] / (\sigma_L^2),$$

$$\rho = (E[M^2] + E[R_1 R_2] + E[MR_1] + E[MR_2]) / (\sigma_L^2).$$

Finally, using the fact that M and R as well as each realization of R are independent and zero mean,

$$\rho = \sigma_M^2 / \sigma_R^2.$$

From this, the correlated mask LER can be separated from the resist LER contribution to the total image by the factor of

$$\text{LER}_M = \text{LER}_L \sqrt{\rho}.$$

The LER_L is the total measured LER: and the difficulties involved in separating mask from resist LER effects in the final printed image are solved.

8.2.2 Applied to mask cleans

Following those methods, we analyzed the correlation of 5 lines, both left and right edges of 50 nm lines. Using a unique alignment feature that is captured in the same image field on a scanning electron micrograph (SEM) (see Figure 78), each line edge was properly aligned for 11 realizations (exposures) at the same dose and best focus. Since the alignment feature is not expected to change position through focus or due to other effects such as line-end shortening, the label is an able candidate for proper alignment, and is our feature of choice. Correlation for each edge (both left and right separately) for the 5 lines was then calculated after alignment through the 11 exposures. This was performed on wafer data collected from the test and reference masks from the 6× and 33× cleaning cycles, for both best focus and -100nm defocus settings.

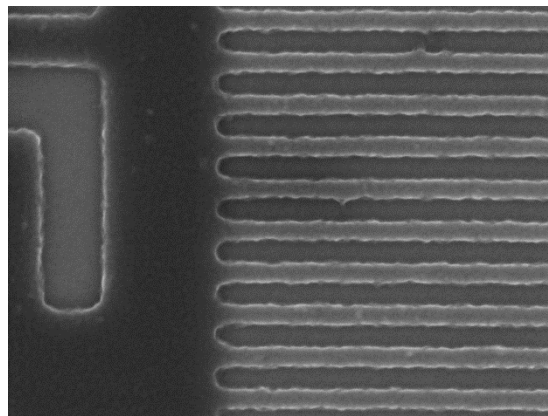


Fig. 78. SEM image of alignment feature next to 50 nm lines. The lines that were analyzed were the 5 to the right of the alignment feature (label) whose left and right edges lie within the extent of the label to allow for alignment.

Analysis is broken into correlation between left- and right-edge LER for each of the 5 lines individually. At the 6 cleaning cycles stage for a best focus image, both the test (process) mask and the reference mask exhibit uncorrelated LER through line realization. This remains relatively unchanged as we go to a -100nm defocus setting. After 33 mask cleaning cycles, there is little observed increase in the correlation between realized exposures of each line, indicating little observable mask cleaning effects up to this point (see all in Figure 79). If correlated effects had been seen, the -100nm defocus setting could have been used as a further means of distinguishing mask LER from mask roughness induced LER, as the mask roughness induced LER component should increase at larger defocus settings.

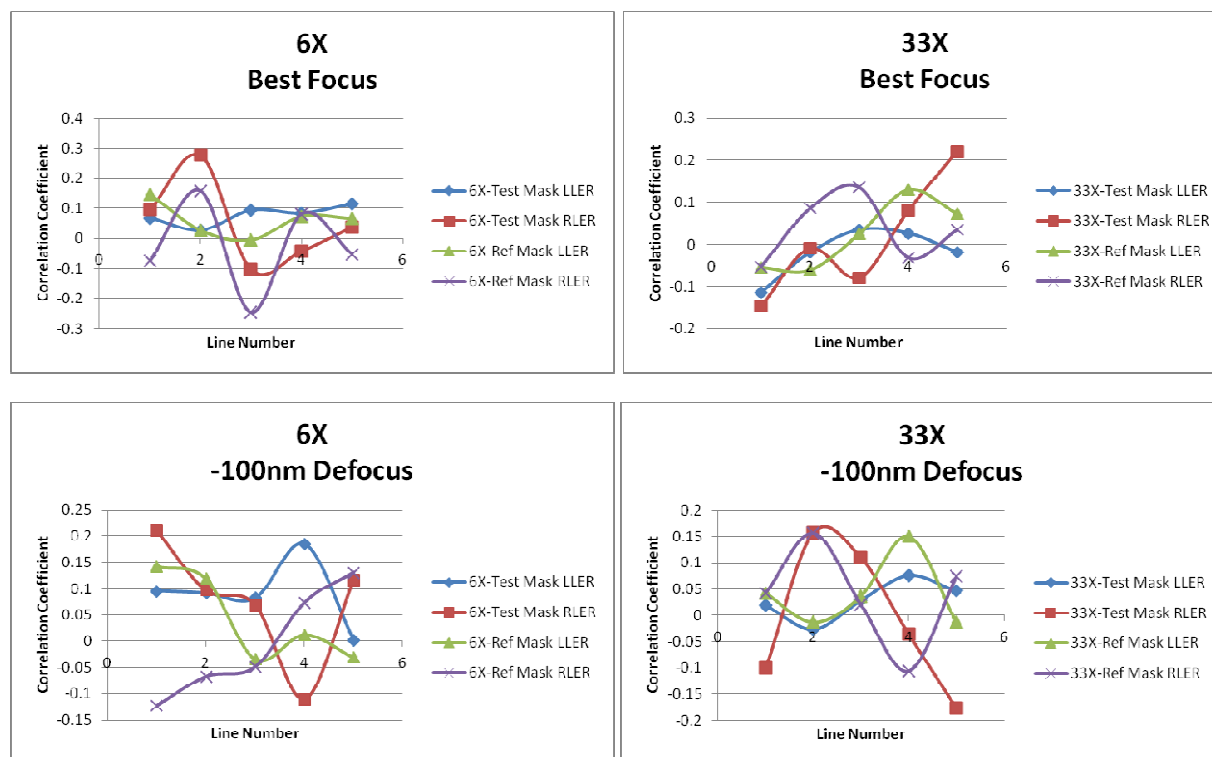


Fig. 79. The correlation between each adjacent exposure of the same line for five lines, separately for left- and right-edge LER, at best focus and -100nm defocus, and for 6 \times and 33 \times stages of the test (process) mask and reference mask. The realizations remain uncorrelated up to this stage, indicating little effect of the mask cleaning process (whereby the correlation should increase).

8.3 Conclusions

In this chapter we examined how repetitive cleans on a mask patterned for use in EUVL affected lithographic performance. Exposures were carried out at the SEMATECH Berkeley micro-exposure tool (MET) for both a cleaned mask and a reference (uncleaned) mask with the same mask architectures. The performance is measured against the process window for line edge roughness (LER) and contact size variation measured using scanning electron microscopy (SEM). Mask properties such as surface roughness and reflectivity were used as metrics of the cleaning process effects. We also introduce a new method involving the correlation in LER of a single line from exposure to exposure at the same dose and focus. If mask cleaning were to

introduce significant damage to either the capping layer or the absorber, we would expect an increase in LER correlation from exposure to exposure of the same feature.

Conclusions from the study show that up to the 33× acid-based cleaning process, there are no detrimental effects to the cleaned mask in comparison to an uncleaned reference mask. This is true in both reflectivity and lithographic performance in terms of lines and spaces, contacts, and LER.

Chapter 9

Conclusions

This dissertation has addressed the critical issue of mask roughness induced LER in extreme ultraviolet lithography, which is a significant new contributor to the total LER budget at the 13.5nm wavelength. As the total LER budget nears 1.7nm value for the 22nm half-pitch node, it is critical to consider every possible contributor to that budget, and its prevention. Potentially, the mask roughness induced LER contribution can be on the order of 1-2nm LER, depending on the level of roughness on the mask as well as imaging conditions such as coherence and defocus. While mask roughness induced LER has until now been largely ignored, this topic has reached a new status that will demand attention.

Currently, many efforts are being made to better understand the origins of the mask roughness induced LER component. Significant work has been made as part of this thesis to demonstrate the coupling of mask-induced speckle intensity variations to line-edge movement through the use of the image-log-slope. Simple tests on a single knife-edge object were constructed to calibrate the model on an ensemble of rough objects. The model was then modified to include an intensity-scaling effect of the clearfield speckle to the speckle at the line-edge through the threshold mechanism. After refining the model, it was applied to a full set of dense lines and spaces, isolated lines and spaces, high and low NA optical systems, on- and off-axis illumination systems, through focus, and on an alternating phase shifting mask to verify its validity uniformly across these set of parameters. Moreover, the model holds well for a variety of mask roughness conditions, from very rough (high RSR, short correlation length, and infinite roughness exponent), to very smooth masks, with accuracy of 0.1-0.2nm LER.

The real advantage of the simplified model relies on the elimination of redundant calculation of mask roughness induced LER across statistical ensembles for a range of features. The simplified model allows a straightforward means to calculate the LER from a single clearfield speckle aerial image simulation to get the intensity statistics particular to a single rough mask, and then subsequently couple that to any feature desired with fast 1D aerial image simulations of the image-log-slope to access the full parameter space.

In the limit of comparatively smooth masks exhibiting long correlation lengths, the simplified model was further enhanced by noting the collapse of all illumination coherence types to a single LER limit. In this case, the coherence conditions are of no importance. Using this concept, we use incoherent image formulation to construct a fast geometric model of mask roughness induced LER by the concept of mask slope error, and propagating its effect through focus by 3 sigma.

The geometric model thus offers a further speed enhancement through its elimination of the additional redundancy of multiple illumination coherence types modeling, which have now all been collapsed into a single PSF.

Apart from a redundancy factor increase in the modeling speed of the LER, the simplified model also provides insight to the physical mechanism by which speckle leads to LER. This suggests potential means by which the mask roughness induced LER can be mitigated and prevented. Specifically, narrow isolated features exhibit distinct LER behavior due purely to a difference in the intensity thresholding for an isolated line versus an isolated space. An aberrations study on the 22nm and 16nm half-pitch nodes showed that total system aberrations should be kept to 0.25nm rms level amongst the primary zernikes, at least from a mask roughness induced LER perspective. Current tools offered by ASML are at the 0.77nm rms level. Individual Zernike sensitivities were identified, primarily in the form of even aberrations such as spherical and astigmatism. A mitigation technique called strip illumination was explored as part of this thesis. The promise of the extended dipole illumination setup was to drive down speckle through increased incoherence while maintaining simultaneously high imaging quality through the image-log-slope by constraining the coherence in the direction orthogonal to the line-space pattern. Results showed not much improvement in mask roughness induced LER compared to other illumination candidates.

This thesis also explored the application of mask roughness induced LER issues in industry-specifically in terms of mask cleaning lithographic performance of CD, LER, and contact size variation. In order for a cleaning method to be a viable method, the mask needs to withstand a cleaning cycle of at least 22× (and 33× for a safe margin) without significant degradation over a period of approximately 3 years. While this study has been conducted over the course of about a year and a half, it has been shown that the cleaning method is viable up to the 33× cleaning cycle.

Until recently, LER has been considered a resist-limited effect. Now, however, it is better understood that system-level effects can greatly influence LER. Overall, two simplified models for mask roughness induced LER have been introduced, developed, validated, and explored, and specific behaviors examined in the presence of aberrations and alternative source shapes, and lastly, experimental results on the mask cleaning process were presented. Future efforts could further expand on the development of an analytic form to the through-focus mask-induced speckle contrast, to eliminate the currently most time consuming aspect of the simulation modeling.

Bibliography

- [1] International Technology Roadmap for Semiconductors, 2010 ed., <http://public.itrs.net/>.
- [2] P. Naulleau, "Relevance of mask-roughness-induced printed line-edge roughness in recent and future extreme-ultraviolet lithography tests," *Appl. Opt.* **43**, 4025-4032 (2004).
- [3] P. Naulleau, D. Niakoula, and Guojing Zhang, "System-level line-edge roughness limits in extreme ultraviolet lithography," *J. Vac. Sci. Technol. B* **26**, 1289-1294 (2008).
- [4] P. Naulleau and S. George, "Implications of image plane line-edge roughness requirements on extreme ultraviolet mask specifications," *Proc. SPIE* **7379**, 73790O (2009).
- [5] P. Naulleau, S. George, and B. McClinton, "Mask roughness and its implications for LER at the 22- and 16-nm nodes," *Proc. SPIE* **7636**, 76362H (2010).
- [6] P. Naulleau, "Correlation method for the measure of mask-induced line-edge roughness in extreme ultraviolet lithography," *Appl. Opt.* **48**, 3302-3307 (2009).
- [7] H. J. Levinson, *Principle of Lithography*, 2nd ed., SPIE Press, Bellingham, WA, 2005.
- [8] C. Mack, *Fundamental Principles of Optical Lithography: The Science of Microfabrication*, Wiley-Interscience, New York, 2007.
- [9] K. Suzuki and B.W. Smith, *Microlithography: Science and Technology*, 2nd ed., CRC Press, Boca Raton, FL, 2007.
- [10] B. Wu and A. Kumar, *Extreme Ultraviolet Lithography*, McGraw Hill, New York, NY, 2009.
- [11] C. Wagner, J. Bacelar, N. Harned, E. Loopstra, S. Hendriks, I. de Jong, L. Levasier, M. van de Kerkhof, H. Meiling, D. Ockwell, R. Peeters, E. van Setten, J. Stoeldraijer, S. Young, J. Zimmerman, R. Kool, P. Kuerz, and M. Lowisch, "EUV Lithography at chipmakers has started: performance validation of ASML's NXE:3100," *Proc. SPIE* **7969**, 79691F (2011).
- [12] M. Born and E. Wolf, *Principles of Optics*, 7th ed., Cambridge University Press, New York, NY, 1999.
- [13] E. Hecht, *Optics*, 4th ed., Addison Wesley, San Francisco, CA, 2002.

- [14] D. Attwood, *Soft X-rays and Extreme Ultraviolet Radiation*, Cambridge University Press, New York, NY, 1999.
- [15] E. Spiller, *Soft X-ray Optics*, SPIE, Bellingham, WA, 1994.
- [16] T.W. Barbee and D.L. Keith, "Synthesis of Metastable Materials by Sputter Deposition Techniques," p. 93 in *Synthesis and Properties of Metastable Phases*, E.S. Machlin and T.J. Rowland, Editors (Metallurgical Society, Amer. Inst. Mech. Eng., Warrendale, PA, 1980).
- [17] J.H. Underwood and T.W. Barbee, "Soft X-ray imaging with a normal incidence mirror," *Nature* **294**, 429 (1981).
- [18] J.H. Underwood and T.W. Barbee, "Layered synthetic microstructures as Bragg diffractors for X-rays and extreme ultraviolet: theory and predicted performance," *Appl. Opt.* **20**, 3027 (1981).
- [19] R.P. Haelbich and C. Kuntz, "Multilayer Interference mirrors for the XUV range around 100 eV photon energy," *Opt. Commun.* **17**, 287 (1976).
- [20] A.E. Rosenbluth, "Computer search for layer materials that maximize the reflectivity of X-ray multilayers," *Revue Phys. Appl. (Paris)* **23**, 1599 (1988).
- [21] T.W. Barbee, S. Mrowka, and M.C. Hettrick, "Molybdenum-Silicon multilayer mirrors for normal incidence in the extreme ultraviolet," *Appl. Opt.* **24**, 883 (1985).
- [22] K.M. Skulina, C.S. Alford, R.M. Bionta, D.M. Makowiecki, E.M. Gullikson, R. Soufli, J.B. Kortright, and J.H. Underwood, "Molybdenum-Silicon multilayer mirrors for normal incidence in the extreme ultraviolet," *Appl. Opt.* **34**, 3727 (1996).
- [23] C. Montcalm, D.G. Stearns, S.P. Bajt, R.D. Behymer, M.A. Wall, and J.A. Folta, "Multilayer reflective coatings for extreme ultraviolet lithography," *Proc. SPIE* **3331**, 42 (1998).
- [24] J.W. Goodman, *Introduction to Fourier Optics*, Roberts and Company, Greenwood Village, CO, 2005.
- [25] S. Braun, H. Mai, M. Moss, R. Scholz, and A. Leson, "Mo/Si multilayers with different barrier layers for applications at extreme ultraviolet mirrors," *Jap. J. Appl. Phys.* **41**, 4074–4081 (2002).
- [26] S. Bajt, J. B. Alameda, T. W. Barbee Jr., et al., "Improved reflectance and stability of Mo-Si multilayers," *Opt. Eng.* **41**, 1797-1804 (2002).
- [27] R. Soufli and E. M. Gullikson, "Absolute photoabsorption measurements of molybdenum in the range 60 to 930 eV for optical constant determination," *Appl. Opt.* **37**, 1713-19 (1998).
- [28] D. Tichenor, G. Kubiak, S. Haney, D. Sweeney, "Extreme ultraviolet lithography machine," U.S. Patent No. 6031598, 2000.

- [29] D. Tichenor, G. Kubiak, W. Replogle, et al., "EUV engineering test stand," Proc. SPIE **3997**, 3997:48-69, 2000. [27] D. Tichenor, A. Ray-Chaudhuri, S. Lee, et al., "Initial results from the EUV engineering test stand," Proc. SPIE **4506**, 4506:9, 2001.
- [30] D. Tichenor, A. Ray-Chaudhuri, W. Replogle, et al., "System integration and performance of the EUV engineering test stand," Proc. SPIE **4343**, 4343:19 (2001).
- [31] D. Tichenor, W. Replogle, S. Lee, et al., "Performance upgrades in the EUV engineering test stand," Proc. SPIE **4688**, 4688:72 (2002).
- [32] D. O'Connell, S. Lee, D. Tichenor, et al., "Lithographic characterization of improved projection optics in the EUVL engineering test stand," Proc. SPIE **5037**, 5037:83 (2003).
- [33] P. Naulleau, et al., "Status of EUV micro-exposure capabilities at the ALS using the 0.3-NA MET optic," Proc. SPIE **5374**, 5374:881 (2004).
- [34] P. Naulleau, K. Goldberg, E. Anderson, et al., "EUV microexposures at the ALS using the 0.3-NA MET projection optics," Proc. SPIE **5751**, 5751:56 (2005).
- [35] P. Naulleau, C. Anderson, K. Dean, et al., "Recent results from the Berkeley 0.3-NA EUV microfield exposure tool," Proc. SPIE **6517**, 6517 (2007).
- [36] A. Brunton, et al., "High-resolution EUV imaging tools for resist exposure and aerial image monitoring," Proc. SPIE **5751**, 5751:78 (2005).
- [37] J. Taylor, D. Sweeney, R. Hudyma, et al., "EUV microexposure tool (MET) for near-term development using a high NA projection system," 2nd International EUVL Workshop, October 19-20, 2000. Proceedings available from SEMATECH, Austin, TX.
- [38] R. Hudyma, J. Taylor, D. Sweeney, et al., "E-D characteristics and aberration sensitivity of the microexposure tool (MET)," 2nd International EUVL Workshop, October 19-20, 2000. Proceedings available from SEMATECH, Austin, TX.
- [39] U. Dinger, G. Seitz, S. Schulte, et al., "Fabrication and metrology of diffraction limited soft x-ray optics for the EUV microlithography," Proc. SPIE **5193**, 5193:18 (2004).
- [40] V. Bakshi (ed.), *EUV Sources for Lithography*, SPIE, Bellingham, WA, 2005.
- [41] M. Corthout, R. Apetz, J. Brudermann, et al., "Sn DPP source-collector modules: Status of alpha resources, beta developments, and the scalability to HVM," Proc. SPIE **6921**, 69210V (2008).
- [42] J. Jonkers, "High power extreme ultraviolet (EUV) light sources for future lithography," *Plasma Sources Sci. Technol.* **15**, S8-S16 (2006).
- [43] J. Pankert, R. Apetz, K. Bergmann, et al., "EUV sources for alpha-tools," Proc. SPIE **6151**, 6151Q (2006).

- [44] H. Meiling, J. Benschop, U. Dinger, P. Kürz, "Progress of the EUVL alpha tool," Proc. SPIE **4343**, 4343:38 (2001).
- [45] H. Meiling, J. Benschop, R. Hartman, et al., "EXTATIC, ASML's α -tool development for EUVL," Proc. SPIE **4688**, 4688:52 (2002).
- [46] H. Meiling, V. Banine, P. Kürz, N. Harned, "Progress in the ASML EUV program," Proc. SPIE **5374**, 5374:31 (2004).
- [47] H. Meiling, H. Meijer, V. Banine, et al., "First performance results of the ASML alpha demo tool," Proc. SPIE **6151**, 615108 (2006).
- [48] N. Harned, M. Goethals, R. Groeneveld, et al., "EUV lithography with the alpha demo tools: Status and challenges," Proc. SPIE **6517**, 651706 (2007).
- [49] H. Meiling, E. Boon, N. Buzing, et al., "Performance of the full field EUV systems," Proc. SPIE **6921**, 69210L (2008).
- [50] B. LaFontaine, Y. Deng, R. Kim, et al., "The use of EUV lithography to produce demonstration devices," Proc. SPIE **6921**, 69210P (2008).
- [51] M. Richardson and G. Schriever, "Laser plasma source for extreme ultraviolet lithography using a water droplet target," U.S. Patent No. 6,377,651 (2002).
- [52] K. Takensoshita, Ph.D. thesis, "Debris characterization and mitigation of droplet plasma sources for EUV lithography," University of Central Florida (2006).
- [53] D. Brandt, "LPP EUV Source Production for HVM," 2011 International Symposium on Extreme Ultraviolet Lithography, October 17-19, 2011. ***Proceedings available from SEMATECH, Austin, TX.***
- [54] H.J. Kwon, "Classification of Multilayer Defects and their printability," 2011 International Symposium on Extreme Ultraviolet Lithography, October 17-19, 2011. ***Proceedings available from SEMATECH, Austin, TX.***
- [55] E. Gallaher, "EUV Masks: Ready or Not?," 2011 International Symposium on Extreme Ultraviolet Lithography, October 17-19, 2011. ***Proceedings available from SEMATECH, Austin, TX.***
- [56] S. Wurm, H. Han, P. Kearney, et al., "EUV mask blank defect inspection strategies for the 32 nm half-pitch and beyond," Proc. SPIE **6607**, 66073A (2007).
- [57] U. Okoroanyanwu and J.H. Lammers, "Resist road to the 22 nm technology node," Future Fab Intl. 17 (2004).
- [58] P. Naulleau, C. Anderson, L.-M. Baclea-an, P. Denham, S. George, K. Goldberg, G. Jones, S. Rekawa, N. Smith, B. McClinton, R. Miyakawa, "Critical Challenges for EUV resist materials," Proc. SPIE **7972**, 797202 (2011).

- [59] V. Constantoudis, E. Gogolides, J. Roberts, and J. Stowers, "Characterization and Modeling of Line Width Roughness (LWR)," Proc. SPIE **5752**, Bellingham, WA (2005).
- [60] P. Naulleau and G. Gallatin, "Spatial scaling metrics of mask-induced line-edge roughness," J. Vac. Sci. Technol. B **26**, 1903-1910 (2008).
- [61] V. Constantoudis, G. P. Patsis, A. Tserepi, E. Gogolides, "Quantification of line-edge roughness of photoresists. II. Scaling and fractal analysis and the best roughness descriptors," J. Vac. Sci. & Technol. B **21**, 1019-1026 (2003).
- [62] Y. Ma, H.J. Levinson, and T. Wallow, "Line Edge Roughness Impact on Critical Dimension Variation," Proc. SPIE, **6518**, 651824 (2007).
- [63] J.-Y. Lee, J. Shin, H.-W. Kim, S.-G. Woo, H.-K. Cho, W.-S. Han, and J.-T. Moon, "Effect of line edge roughness (LER) and line width roughness (LWR) on sub-100nm device performance," SPIE **5376**, Bellingham, WA (2004).
- [64] E. Gogolides, V. Constantoudis, G. Patsis, A. Tserepi, "A review of line edge roughness and surface nanotexture resulting from patterning processes," Micro. Eng. **83**, 1067-1072 (2006).
- [65] P. Naulleau, C. Anderson, L.-M. Baclea-an, P. Denham, S. George, K. Goldberg, G. Jones, B. McClinton, R. Miyakawa, I. Mochi, W. Montgomery, S. Rekawa, and T. Wallow, "Using synchrotron light to accelerate EUV resist and mask materials learning," SPIE **7985**, 798509 (2011).
- [66] G. Gallatin, "Resist Blur and Line edge roughness," Proc. SPIE **5754**, 38-52 (2005).
- [67] P. Naulleau and G. Gallatin, "Line-edge roughness transfer function and its application to determining mask effects in EUV resist characterization," Appl. Opt. **42**, 3390-3397 (2003).
- [68] G. Gallatin and P. Naulleau, "Modeling the transfer of line edge roughness from an EUV mask to the wafer," Proc. SPIE **7969**, 796903-796903-10 (2011).
- [69] P. Naulleau, S. George, and B. McClinton, "How good will EUV masks need to be to meet LER requirements?," *LBNL presentation*.
- [70] J.W. Goodman, *Statistical Optics*, Wiley Classics, New York, NY (2000).
- [71] B. McClinton and P. Naulleau, "Mask roughness induced LER: a rule-of-thumb," J. Micro/Nanolith. MEMS and MOEMS **9**, 041208 (2010).
- [72] P. Naulleau and S. George, "Validity of the thin mask approximation in extreme ultraviolet mask roughness simulations," Appl. Opt. **50**, 3346-3350 (2011).
- [73] S. George, P. Naulleau, E. Gullikson, I. Mochi, F. Salmassi, K. Goldberg, and E. Anderson, "Replicated mask surface roughness effects on EUV lithographic patterning and line edge roughness," Proc. SPIE **7969**, 79690E (2011).

- [74] T. Milster and N. Beaudry, "Scattering and Coherence in EUVL," in *Emerging Lithographic Technologies II*, Y. Vladimirsky, ed., Proc. SPIE **3331**, 537 (1998).
- [75] N. Beaudry and T. Milster, "Effects of mask roughness and condenser scattering in EUVL systems," in *Emerging Lithographic Technologies III*, Y. Vladimirsky, ed., Proc. SPIE **3676**, 653 (1999).
- [76] N. Beaudry and T. Milster, "Effects of object roughness on partially coherent image formation," *Opt. Lett.* **25**, 454-456 (2000).
- [77] PROLITH is a registered trademark of KLA-Tencor Corporation, 160 Rio Robles, San Jose, Calif. 95134.
- [78] Panoramic Technology, Inc., "EM-suite: core lithography simulation package," (2009), see <http://www.panoramictech.com>.
- [79] EUV Technology Corp., <http://www.euvl.com/summit>.
- [80] B. McClinton and P. Naulleau, "Mask roughness induced LER: a rule-of-thumb," Proc. SPIE **7636**, 76362G (2010).
- [81] E. Gullikson, "EUV Scattering from mask substrate roughness," 2002 International Symposium on Extreme Ultraviolet Lithography, October 15-17, 2002. ***Proceedings available from SEMATECH, Austin, TX.***
- [82] B. McClinton and P. Naulleau, "Physical and geometric optics models for mask roughness induced LER," Proc. SPIE **7969**, 79691Y (2011).
- [83] B. McClinton and P. Naulleau, "Mask roughness induced LER control and mitigation: aberrations sensitivity study and alternate illumination scheme," Proc. SPIE, **7969**, 79691Z (2011).
- [84] R. Chen, B. McClinton, S. George, Y. Kim, L.-M. Baclea-an, and P. Naulleau, "Effect of repetitive acid-based cleaning on EUV mask lifetime and lithographic performance," Proc. SPIE **8166**, 81661O (2011).
- [85] S. George, R. Chen, L.-M. Baclea-an, and P. Naulleau, "22× mask cleaning effects on EUV lithography process and lifetime," Proc. SPIE **7969**, 79691W (2011).
- [86] S. George, L.-M. Baclea-an, P. Naulleau, R. Chen, T. Liang, "Extreme ultraviolet mask surface cleaning effects on lithography process performance," *J. Vac. Sci. Technol. B* **28**, C6E31 (2010).
- [87] P. Naulleau, C. Anderson, J. Chiu, K. Dean, P. Denham, K. Goldberg, B. Hoef, S. Huh, G. Jones, B. La Fontaine, A. Ma, D. Niakoula, J. Park, and T. Wallow, "Advanced extreme ultraviolet resist testing using the SEMATECH Berkeley 0.3-NA microfield exposure tool," Proc. SPIE **6921**, 69213N (2008).

[88] P. Naulleau, K. Goldberg, E. Anderson, J. Cain, P. Denham, K. Jackson, A.-S. Morlens, S. Rekawa, F. Salmassi, "At-wavelength alignment and testing of the 0.3 NA MET Optic," *J. Vac. Sci. Technol. B* **22**, 2962 (2004).

[89] P. Naulleau, "Effect of mask-roughness on printed contact-size variation in extreme-ultraviolet lithography," *Appl. Opt.* **44**, 183-189 (2005).